Non-invasive therapy of brain disorders with focused ultrasound: From animal experiments to clinical transfer

Youliana Younan, Jean-François Aubry, Tanter Mickael

To cite this version:

Youliana Younan, Jean-François Aubry, Tanter Mickael. Non-invasive therapy of brain disorders with focused ultrasound: From animal experiments to clinical transfer. Medical Physics [physics.med-ph]. Université Pierre et Marie Curie - Paris VI, 2014. English. NNT : . pastel-00974865

HAL Id: pastel-00974865
https://pastel.hal.science/pastel-00974865
Submitted on 7 Apr 2014

UNIVERSITE PARIS. Pierre et Marie Curie (Paris 6)

ECOLE DOCTORALE : La Physique de la Particule à la Matière Condensée - ED389
SPECIALITE : Acoustique Physique

Institut-Langevin, ESPCI-ParisTech, CNRS UMR7587, INSERM U979

Présenté par

Youliana YOUNAN

Pour obtenir le garde de DOCTEUR de l'UNIVERSITE PARIS 6

Non-invasive therapy of brain disorders with focused ultrasound: From animal experiments to clinical transfer

Soutenue le 7 Mars 2014

Devant le jury composé de :

M. Jean-François Aubry	Directeur de thèse
M. Alexandre Carpentier	Président
Mme. Gail ter Haar	Rapporteur
M. David Melodelima	Rapporteur
M. Mickael Tanter	Co-directeur de thèse

إهداء

إلى الشجرة المباركة التي تظللني بطيبِ أوراقها...وتسترني بجميل فيّها وتطعمني من ثمارها، إلى الذي فضائله كالنجوم في الأفق لا يحصيها العد، إلى صاحب القلب الكبير ...

" أبي "

إلى منحة السماء للأرض ... إلى الملاك في صورة بشر... إلى الشفتان التي لم تكفان عن الصلاة والدعاء لي... إلى التي فاضت بالنعيم يداها... إلى التي لا استبدل شيئا في الوجود برضاها...

" أمي "

إلى من زينوا حياتي بأزاهير ضحكاتهم ، ويتعاطفوا معي عندما تعبس الأيام بوجهي... إلى الفراشات التي كانت وما تزال وستبقى إلى جانبي...

" أخواتي : **جنان، سوزان، حنان، ليبان** "

إلى بواشق أسرتي و أصدقاء طفولتي...

" أخويّ : **يونان و جان** "

إلى أجمل العصافير ، إلى أحلى الضحكات ، إلى من أضافوا البهجة لحياتي...

" إيمانويل، لويس، ليبان، لاميتا، ميري مي، جويس "

إلى أخوةٍ لم تلدهن أمي...

" القس بولس، كبرئيل، باسل "

إلى أعظم الناس في عيني ، وكان رأس ما عظّمَهُ في عيني صغر الدنيا في عينيه...

" الربّان نوح شابا "

إلى من لم يبخلوا عليّ بشيء، إلى دكاترتي في الجامعة وأساتذتي في جميع مراحلي الدراسية ، وإلى جميع زملائي و أصدقائي والى الدكتور **قصي حجو**، والاستاذ **خالد عبيد**، والاستاذ **منان سليمان**، و**تالين باليان**...

أهديكم كتابي هذا...

يوليانا قسطنطين يونان

Dédicace

Pour l'arbre béni qui m'abrite par la générosité de ses feuillages... qui me protège par sa belle ombre, qui me nourrit de ses fruits, pour celui qui ses vertus comme des étoiles à l'horizon que nul compte n'énumère, à la personne au grand cœur cher à mon cœur...

"**Papa**"

Pour le don du ciel à la terre ... à l'ange qui a pris la forme humaine ... aux lèvres qui n'ont cessé de prier pour moi ... pour celle que la douceur inonde ses mains ... pour laquelle je ne remplacerai pour rien au monde son consentement ...

" **Maman** "

Pour ceux qui ont décoré ma vie par leurs rires, et sympathiser avec moi quand les jours sombres me fronce les sourcils... pour les papillons, qui étaient, sont, et toujours resteront à mes cotés

"Mes Sœurs **: Jinan, Suzan, Hanan et Liban**"

Pour les Aigles de ma famille et les compagnons de mon enfance

"Mes Frères : **Younan et Jean**"

Pour le plus beaux des oiseaux, les plus doux des rires, ceux qui ont ajouté de la joie à ma vie….

" **Emanuel, Louis, Liban, Lamita, Mary May et Joyce** "

Pour les Frères que je n'ai pas eu de ma mère

"**Père Paul, Gabriel et Basel**"

Pour les meilleurs gens à mes yeux, qui sont autant grands à mes yeux que le monde est tout petit aux leurs…

"**Père Noé Shaba**"

Pour ceux qui ont toujours été généreux avec moi, à mes Docteurs et mes professeurs de l'université, de toutes les étapes de mes études, et à tous mes collègues et mes amis et à Docteur **Qusai Hajo**, Professeur **Khaled Obied**, Professeur **Mannan Seuleiman** et **Talin Balian**.

Je leur dédie ce travail ...

Youliana Koustantine Younan

Remerciements

Ce travail a été réalisé à l'institut Langevin sous la direction de Jean-François Aubry et Mickael Tanter à qui je tiens à leur exprimer ma plus vive reconnaissance car je leur dois ma présence dans ce laboratoire. Je les remercie pour leur présence et patience avec moi au laboratoire et dans la vie de tous les jours.

Je remercie Mathias Fink de m'avoir accueillie dans l'institut pour travailler sur un sujet aussi novateur que passionnant.

Je tiens tout particulièrement à remercier Thomas. Il m'a d'abord aidée avec une grande compétence et une patience inégalable lorsque je peinais sur des problèmes.

Je remercie Pierre Pouget, Nicolas Wattiez, Benoit Larrat et Abdelhak Souilah qui ont largement contribué au travail expérimental présenté dans ce mémoire.

Je remercie également tous les membres de l'institut qui ont d'une façon ou d'une autre contribué à mon travail, avec qui je me sens comme en famille et pour tous les bons moments que nous avons passé ensemble.

Je suis honorée que Gail ter Haar et David Melodelima aient accepté d'examiner mon travail et je les en remercie.

Enfin, je remercie Alexandre Carpentier d'avoir bien voulu présider le jury de thèse.

Résumé

Ces travaux de thèse portent sur l’étude de nouvelles modalités de guidage de la thérapie transcrânienne par ultrasons focalisés, technique non invasive particulièrement prometteuse pour le traitement de troubles neurologiques tels que le tremblement essentiel ou le tremblement parkinsonien. Une nouvelle technique d’imagerie par résonance magnétique a tout d’abord été utilisée pour imager l'emplacement du faisceau ultrasonore produit par un prototype préclinique : les déplacements induits par les ultrasons dans une cervelle de veau ex vivo ont été imagés sans distorsion à l’aide d’une séquence d’écho de spin accélérée, avec un dépôt d'énergie jusqu’à quatre fois inférieur aux techniques existantes. Nous avons ensuite étudié les effets directs des ultrasons sur l'activité cérébrale par neuromodulation ultrasonore in vivo, de façon similaire à la stimulation magnétique transcrânienne, mais avec les capacités de ciblage millimétriques des ultrasons focalisés. Des expériences ont été tout d’abord menées sur un modèle de rat anesthésié afin d’étudier la pression seuil pouvant induire un effet moteur. Le champ acoustique simulé dans la tête de rat est fortement affectée par des réverbérations, ce qui doit être pris en compte pour l’évaluation in situ des paramètres acoustiques de neurostimulation, en particulier à basse fréquence et pour les petits animaux. Enfin, pour la première fois, nous avons montré que les ultrasons focalisés de faible intensité pouvaient moduler de façon causale le comportement d’un primate non humain éveillé: le temps de latence d'une tâche d'anti-saccade est retardé de façon significative par des ultrasons focalisés dans le champ visuel frontal.

Mots-clés

ultrasons focalisés ; neuromodulation ; tremblement essentiel ; antisaccades ; force de radiation ; thérapie par ultrasons

Summary

The work presented in this thesis investigates novel modalities to guide Transcranial Magnetic Resonance guided Focused Ultrasound (TcMRgFUS). TcMRgFUS is an emerging and promising non-invasive technique for the treatment of neurological disorders, such as essential tremor or Parkinsonian tremor. A novel Magnetic Resonance Acoustic Radiation Force Imaging (MRARFI) has been used to image the location of the ultrasonic beam produced by a preclinical prototype: an accelerated 2D spin-echo MR ARFI pulse sequence has been introduced to generate undistorted ultrasound-induced displacement maps in ex vivo veal brains with minimum energy deposition. We then investigated direct effects of the ultrasonic beam on brain activity by conducting in vivo ultrasonic neuromodulation, similarly to what is currently achieved with transcranial magnetic stimulation (TMS) but with the millimetric targeting capabilities of the ultrasound. Experiments have been first conducted in an anesthetized rat model to investigate the motor threshold. Numerical simulations have shown that the acoustic pattern in the rat head is affected by reverberations and that special care must be taken when relating acoustic parameters to neurostimulation effects, especially at a low frequency and for small animals. Finally, for the first time, we used low intensity FUS stimulation to causally modulate behavior in an awake nonhuman primate brain. We showed that the latency of an anti-saccade task was delayed significantly in the presence of ultrasonic beam focused in the Frontal Eye Field. Sham experiments did not show any significant change in the latencies.

Key-words

focused ultrasound ; neuromodulation ; essential tremor ; antisaccades ; radiation force ; therapeutic ultrasound

Table des matières

Chapitre 1 Résumé en français

1.1 Introduction

Les utrasons sont des ondes mécaniques dont la fréquence ne peut pas être entendue par l'homme (**Figure 1.1**), car l'homme entend normalement uniquement les fréquences sonores comprises entre 20Hz et 20000Hz. Les ultrasons se sont avérés être un outil médical important pour le diagnostic et le traitement de plusieurs troubles physiques.

L'application médicale des ultrasons la plus couramment utilisée et la plus connue est l'échographie, principalement en raison de son coût raisonnable, de ses bonnes résolutions temporelles et spatiales mais aussi l'absence d'effet irradiant. Cependant les ultrasons ne se limitent pas à l'échographie.

Figure 1.1: Echelle de fréquences des ondes sonores

Production des ondes ultrasonores

Pour générer des ondes ultrasonores, un transducteur piézoélectrique qui convertit l'énergie électrique en son peut être utilisé. Comme l'illustre la **Figure 1.2**, L'élément piézo-électrique oscille en expansion et en contraction à plusieurs reprises sous l'effet de la tension sinusoïdale qui lui est appliquée, générant une onde sonore.

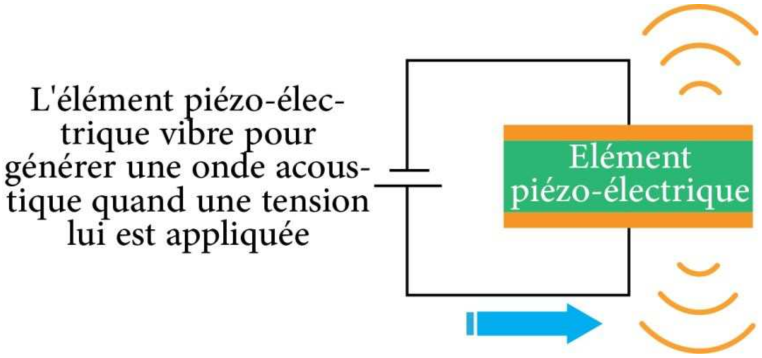

Figure 1.2: Génération d'une onde sonore par un élément piézo-électrique

Un matériau de "backing" est généralement ajouté à l'arrière et joue le rôle de réflecteur, ce qui permet à la fois de réfléchir l'onde arrière et de renforcer l'onde émise par la face avant. (Figure 1.3).

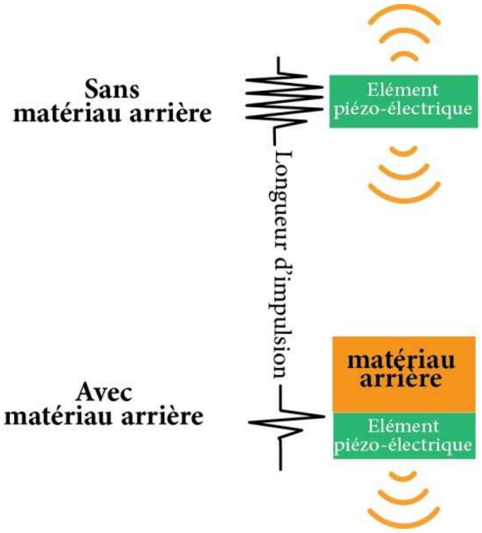

Figure 1.3: Utilisation d'un matériau arrière de "backing" placé derrière l'élément piézoélectrique

Les ondes ultrasonores générées sont ainsi transmises à partir de l'élément piézo-électrique par sa face avant. En présence d'une forte différence d'impédance acoustique sur le trajet, l'onde sera réfléchie et ne pourra pénétrer d'avantage dans les tissus. La présence d'air est donc prohibée et un matériau intermédiaire de couplage (gel échographique) est placé entre l'élément piézoélectrique et les tissus (**Figure 1.4**).

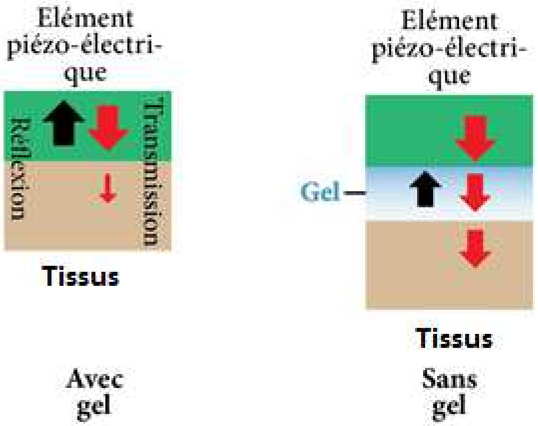

Figure 1.4: Ondes ultrasonores transmises avec et sans gel

Les ondes ultrasonores ainsi générées dans les tissus sont des ondes longitudinales (L-Waves, **Figure 1.5**), pour lesquelles le mouvement particulaire est dans la même direction que la propagation des ondes.

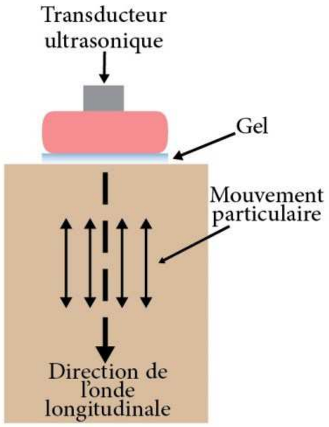

Figure 1.5: onde longitudinale

:

Les ondes de surpression (compression positive et raréfaction négative) se propagent ainsi de proche en proche dans le corps humain. Elles sont liées au déplacement particulaire via l'impédance acoustique du milieu :

$$\boldsymbol{P = Z \times v}$$

Où Z est Impédance acoustique du milieu et v la vitesse de déplacement particulaire

L'amplitude de pression P_0 est la surpression maximale générée, généralement exprimée en MPa.

D'autres paramètres sont utilisés pour caractériser complètement l'impulsion ultrasonore (**Figure 1.6**) ; ils seront beaucoup utilisés dans ce manuscrit afin de décrire les émissions ultrasonores.

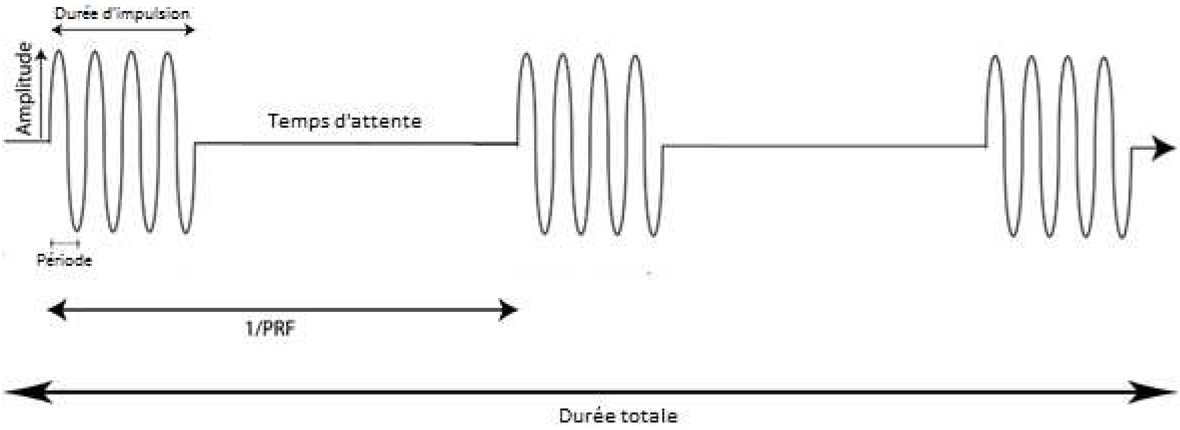

Figure 1.6: Paramètres ultrasonores.

- Durée d'impulsion: durée de la génération élémentaire d'une impulsion.
- Fréquence de répétition des impulsions (PRF : pulse repetition frequency): le nombre de répétitions de l'impulsion par seconde.

- Temps de cycle: Pourcentage du temps pendant lequel les ultrasons sont générés (durée d'impulsion) sur la période de répétition des impulsions.

La longueur d'onde est la distance entre deux compressions ou raréfactions maximales et dépend de la fréquence émise et de la vitesse du son dans le milieu de propagation selon la formule suivante:

$$\lambda = \frac{c}{f}$$

Où c’est la vitesse de l'onde; mesurée en $m.s^{-1}$ et f a fréquence (le nombre de fois qu'une particule oscille par seconde).

Plus la fréquence ultrasonore est élevée, plus la longueur d'onde est faible et plus la distance de pénétration dans les tissus est également faible à cause de l'atténuation, plus forte à haute fréquence.

Les transducteurs ultrasonores pour la thérapie médicale ont des formes et des dimensions adaptées à l'organe pour lequel ils sont conçus. Ils sont en général focalisés pour concentrer l’énergie au point cible (Figure 1.7). C'est le cas des transducteurs que nous avons utilisés pour les expériences sur rongeurs et sur primates.

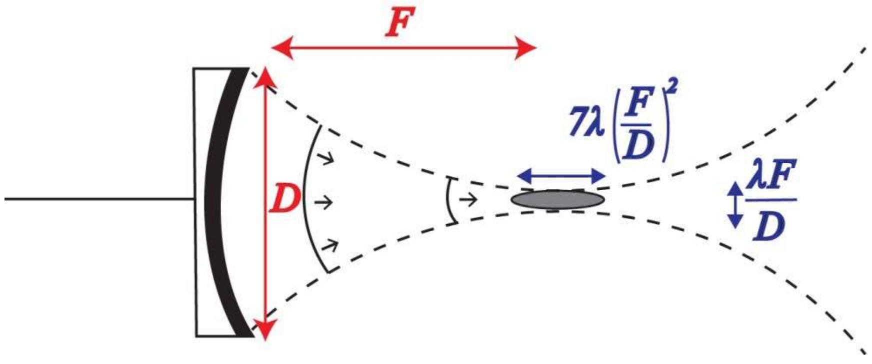

Figure 1.7: Focalisation par un élément piézo-électrique

La taille du foyer est alors déterminée par la géométrie du transducteur (son ouverture D) et la profondeur F à laquelle il focalise. elle a typiquement la forme d'un cigare de largeur λF/D et de profondeur 7λ(F/D)².

Le transducteur peut éventuellement comporter plusieurs éléments. Les dimensions globales de la tâche focale restent identiquement liées à la géométrie du transducteur (Figure 1.8). Un tel réseau multiélément a été utilisé dans le chapitre sur l'accélération Keyhole de l'imagerie IRM de la force de radiation et permet de déplacer la tâche focale ou corriger les aberrations du crâne.

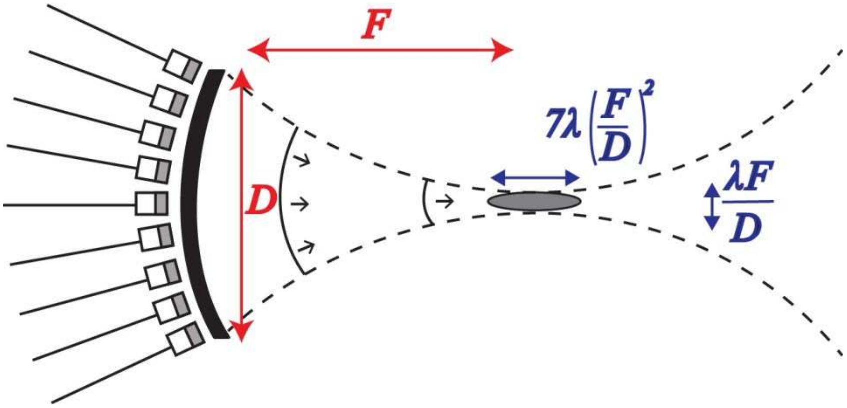

Figure 1.8: Focalisation avec un réseau multiéléments

L'intensité acoustique désigne la puissance d'une onde sonore par unité de surface Figure 1.9. L'intensité acoustique moyenne sur une période est donnée par la formule :

$$\mathrm{I} = \frac{{P_0}^2}{2Z}$$

Où P_0 est l'amplitude de surpression et Z l'impédance du milieu. Elle s'exprime en Watt par mètre carré (W/m² ou $\mathrm{W{\cdot}m^{-2}}$)

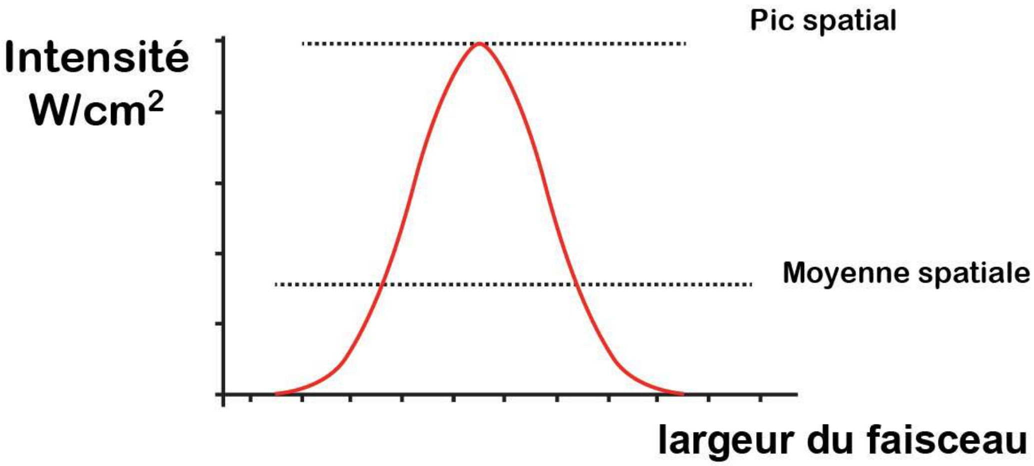

Figure 1.9: Le profil de l'intensité en fonction de la distance

Pour des ultrasons pulsés, l'intensité varie de plus avec le temps (**Figure 1.10**), et on définit donc usuellement les valeurs suivantes :

- Le pic temporel (TP : time peak) : la plus grande intensité trouvée dans une impulsion.

- La moyenne temporelle (TA : time average) qui comprend le temps «mort» entre les impulsions.

- Impulsion moyenne (PA : pulse average) calculée uniquement sur la durée de l'impulsion donnée sans le temps "mort".

L'intensité est importante lors de la discussion des effets biologiques et l'innocuité des séquences ultrasonores.

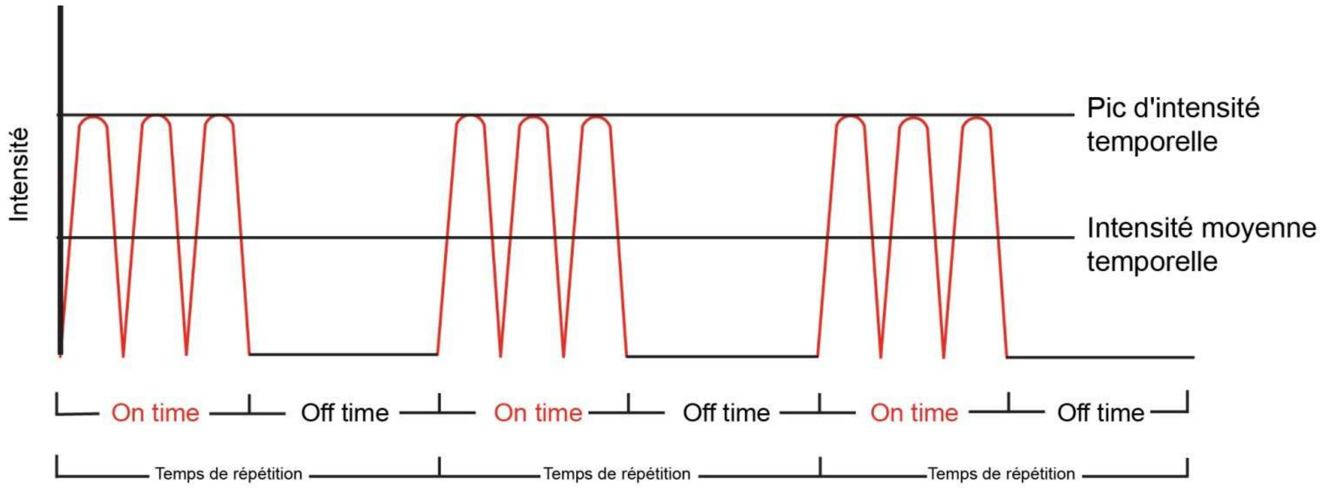

Figure 1.10: Le profil de l'intensité en fonction du temps

Puissances ultrasonores

Les ultrasons interagissent avec les tissus biologiques selon deux types principaux d’interaction : par effets thermiques ou mécaniques.

Les effets thermiques créent un échauffement du tissu lié à l’absorption des ultrasons par le tissu. La quantité d’énergie thermique transférée aux tissus par unité de temps est proportionnelle à l’intensité acoustique.

Les effets mécaniques sont eux-mêmes de plusieurs types. Il y a bien sûr la vibration acoustique elle-même qui entraîne un déplacement du tissu de quelques dizaines de nanomètres à la haute fréquence des ultrasons ; l’augmentation de la pression conduit ainsi à l’augmentation de la l’amplitude de vibration. D’autres effets plus complexes sont aussi induits, comme la constitution d’une force basse fréquence appelée force de radiation proportionnelle à l’intensité acoustique moyenne, créant des déplacements de quelques dizaines de microns à basse fréquence, liés au transfert de quantité de mouvement. Enfin, la cavitation acoustique de microbulles gazeuses, qui correspond à l’oscillation stable ou inertielle de microbulles injectées ou générées spontanément.

L'index mécanique (MI : mechanical index) a été introduit par la Food and Drug administration (FDA) américaine afin d'évaluer les risques d'apparition d'effets mécaniques. Il est défini par :

$$\mathrm{MI} = \frac{PNP}{\sqrt{F_c}}$$

où PNP est la pression du pic négatif de l'onde ultrasonore (qui doit ici être exprimé en MPa) divisé par la racine carrée de la fréquence centrale (Fc) de l'onde ultrasonore (qui doit être exprimée en MHz). L'index mécanique maximal autorisé pour l'imagerie échographique du cœur ou des fœtus est de 1.9. Il est de 0.2 pour l'imagerie de l'œil.

Qu'elles soient d'origine mécanique ou thermique, comme toutes interactions, au-delà d'un certain seuil, elles peuvent provoquer de sérieux dommages aux tissus, jusqu'à leur destruction totale ou partielle.

L'absorption thermique peut ainsi entrainer la nécrose du tissu. La cavitation inertielle peut quant à elle déchirer le tissu cellulaire environnant, provoquant des hémorragies ou des ruptures tissulaires. Ces deux effets sont mis à profit respectivement dans le cadre des techniques de HIFU (High Intensity Focused Ultrasound) et d'histotripsie (destruction des calculs rénaux). Dans le cadre de l'utilisation des ultrasons en imagerie, des normes strictes sont imposées aux constructeurs afin de garantir l'innocuité des séquences ultrasonores utilisées.

Mais nous savons aussi que, à des puissances intermédiaires, ces effets thermiques ou mécaniques peuvent avoir des effets physiologiques qui ne mettent pas forcément en péril la survie du tissu et permettent des applications médicales importantes. Un exemple est l'ouverture de la barrière hémato-encéphalique par ultrasons focalisés et co-injection d'agents de contraste (microbulles de gaz, air, azote ou perfluorocarbone), qui permet de façon non invasive et localisée d'ouvrir transitoirement la barrière pour laisser pénétrer dans le cerveau des molécules qui seraient normalement bloquées en raison de leur taille (> 400 Da). Des études effectuées à l'University of Columbia (New York, USA) en 2009, ont montré que la cavitation stable était le phénomène responsable de l'ouverture de la barrière (Tung et al. 2010)(McDannold, Vykhodtseva, and Hynynen 2008)(Tung et al. 2011) et que celle-ci n'entrainait pas de dommages visibles sur les coupes histologiques.

Un autre effet similaire est la sonoporation qui permet la modification transitoire de la perméabilité des membranes cellulaires par cavitation acoustique. Cette technique est employée notamment pour faire pénétrer localement des molécules de taille trop importante pour traverser d'elle-même la membrane(Deng et al. 2004), comme des fragments d'ADN utilisés pour la thérapie génique in vivo. L'adjonction de microbulles permet là encore de favoriser la cavitation acoustique par rapport aux effets thermiques.

Depuis plusieurs décennies, on a assisté à l'étude des ultrasons comme moyen de stimulation et d'inhibition réversible de l'activité électrique. Dans les années 30, Harvey fut le premier à démontrer le potentiel des ultrasons pour stimuler les nerfs et les fibres musculaires(Harvey 1930). D'autres expériences de stimulation ou inhibition ultrasonore sur les nerfs ou les muscles ont suivi: sur le nerf saphène interne du chat *in vitro* (Young and Henneman 1961), sur d'autres préparations *in vitro* de nerfs périphériques de grenouilles (Lele 1962; Mihran, Barnes, and Wachtel 1990; Tsui, Wang, and Huang 2005), *in vivo* sur les nerfs de la main chez l'homme(Davies and Gavrilov 1996), *in vivo* sur la colonne vertébrale du chat (Shealy and HENNEMAN 1962).

Concernant le tissu cérébral, Fry a montré dès les années 50 que la réponse induite par un stimulus visuel pouvait être inhibée de façon réversible dans le cortex visuel primaire du chat, par la transmission d'ultrasons dans le corps géniculé latéral(W. Fry et al. 1958). L'existence de sensations auditives chez des patients soumis à un doppler transcranien de l'artère basilaire ont également été rapportées(Magee and Davies 1993). Des expériences réalisées sur des tranches d'hippocampes de rongeur et consistant à mesurer directement l'influence des ultrasons sur l'amplitude de potentiels d'action ont permis de montrer une augmentation ou une diminution de cette amplitude en fonction de la puissance des ultrasons (Rinaldi et al. 1991). Il ne s’agit pas là à proprement parler de stimulation directe par les ultrasons mais d’une modulation de l’excitabilité des neurones. On ne parlera pas dans ce dernier cas de stimulation ultrasonore, expression consacrée à la faculté de stimulation et d’inhibition directe de l’activité neuronale par les ultrasons.

Récemment, l’équipe américaine de William Tyler a démontré la possibilité d’induire une neurostimulation directe à faible pression acoustique (Tyler et al. 2008). Ces travaux présentent ainsi deux nouveautés : la possibilité de stimuler directement les neurones et non pas seulement de moduler l’excitabilité neuronale et de le faire à faible pression acoustique, c’est-à-dire avec des risques de dommages sur le tissu cérébral potentiellement nuls. Ces études ont montré la faisabilité de générer, par ultrasons à basse fréquence et faible intensité, des potentiels d’action qui ont été enregistrés par électrophysiologie, d’abord dans des tranches d’hippocampes de souris(Tyler et al. 2008) (*whole-cell current patch-clamp*) puis dans des souris *in vivo* (potentiels locaux de champ ou LFP)(T. Tufail et al. 2010; Y. Tufail et al. 2011). Sur les tranches, l’ouverture des canaux calciques a été observée par microscopie confocale tandis que sur des souris *in vivo*, sans craniotomie, des contractions musculaires suite à l’insonification du cortex moteur ont pu être observées et enregistrées par électromyographie (EMG).

Des travaux similaires ont été publiés un peu plus tard par l’équipe de Yoo sur le lapin (avec craniotomie) avec des résultats similaires(Yoo et al. 2011). Yoo utilise un transducteur compatible IRM ce qui lui permet d’ajouter l’IRM fonctionnel à ses expériences de neurostimulation. Il visualise ainsi directement l’activation de la zone ciblée, ie cortex moteur. Yoo utilise aussi des potentiels évoqués visuels (stimulation lumineuse) pour mettre en avant l’inhibition de l’activité neuronale dans le cortex visuel, d’abord par analyse de la composante p30 du signal EEG (pic positif à 30ms) puis directement par la diminution du signal Bold sur les images fMRI. Pour l’inhibition, Yoo utilise des impulsions ultrasonores plus courtes tout en augmentant la durée totale d’insonification (9s), en conservant la pression et la fréquence ultrasonore inchangées. Dans ces conditions, l’histologie ne montre aucun dommage sur la zone ciblée et l’utilisation de l’IRM permet de vérifier l’intégrité de la barrière hémato-encéphalique (par injection de Gadolinium) et l’absence d’élévation de la température (<0.8°C).

1.2 HIFU transcrâniens

Les thérapies transcraniennes par HIFU ont comme avantage premier d'être non invasifs, ce qui permet d'envisager un traitement chez les patients présentant des risques opératoires. Elles ont l’autre avantage d’utiliser des rayonnements non ionisants. Les radiations ionisées produisent en effet d’une part des effets secondaires néfastes sur les patients et imposent des précautions pour le personnel soignant, et peuvent d’autre part générer des cancers radio-induits en cas de traitements répétitifs. Les ultrasons présentent d’ailleurs un intérêt potentiel pour le traitement du cerveau en développement des enfants, plus sensibles aux radiations ionisantes. L’impact en termes de santé publique et de confort pour le patient pourrait être très avantageux, notamment parce qu’un tel équipement s’affranchirait à la fois des problèmes posés par la chirurgie (infections, hémorragies, etc.), de ceux posés par les radiations ionisantes (radioprotection, etc.) et par son coût qui pourrait être inférieur à la radiochirurgie stéréotaxique.

Récemment les premiers essais cliniques utilisant une fréquence de 660 kHz ont débuté avec des systèmes développés par Insightec pour adresser différentes pathologies du cerveau. Le système utilise une sonde HIFU hémisphérique, ce qui distribue l’énergie acoustique sur une surface de crâne maximale, mais limite par ailleurs le positionnement de la sonde par rapport à la tête et peut entrainer de grands angles entre l'axe des éléments et les normales géométriques du crâne. Le couplage est effectué par de l'eau sans autre interface entre la sonde et la tête. Celle-ci est fixée à un cadre stéréotaxique et peut être translatée. Une correction d'aberration simple est effectuée en utilisant un modèle du crâne basé sur son épaisseur et des tracés de rayons entre les éléments et la cible.

En 2009, le premier essai clinique contre les glioblastomes fût réalisé sur 3 patients à l'aide de ce système. Néanmoins les températures maximales atteintes après des émissions de 20 s étaient trop faibles (42 °C, 48 °C et 51 °C pour chacun des patients) pour engendrer un effet thérapeutique significatif (McDannold et al. 2010). La même année, onze patients furent traités pour des douleurs neurogéniques chroniques résistantes aux thérapies existantes (Martin et al. 2009)(Jeanmonod et al. 2012). Ils étaient conscients, sous sédatif, régulièrement interrogés pendant l'intervention, ainsi que sous monitoring conventionnel. Les cibles de 3 mm à 5 mm de diamètre étaient dans la partie postérieure du noyau central thalamique latéral. Le traitement fut réalisé par des émissions HIFU de puissances acoustiques entre 800 W pendant 20 s et 1200 W pendant 10 s. Des températures de 51 °C à 64 °C furent atteintes. Les patients ont ressenti une diminution plus ou moins importante de la douleur immédiatement après l'intervention et qui semble persister après un an, ceci étant confirmé par une amélioration de mesures électro-encéphalographiques (EEG). Néanmoins pour un patient, un cas d'hémorragie cérébrale couplé à une ischémie fut détecté par IRM provoquant des effets secondaires toujours présents un an après le traitement (Jeanmonod et al. 2012). Selon les auteurs, un phénomène de cavitation ou de température trop élevée (64 °C mesurés) pourrait en être la cause.

Entre 2011 et 2012, 15 patients pharmaco-résistants ont participé à une étude de phase I contre les tremblements essentiels utilisant également ce type de système (Elias et al. 2013). Le traitement consistait en l'ablation d'une cible située dans le noyau thalamique (VIM). Les températures maximales atteintes variaient entre 55 et 63 °C et des échauffements successifs étaient répétés jusqu'à la diminution des tremblements. Les résultats montrent une diminution moyenne des tremblements de la main contra-latérale de 67 % un an après le traitement, se traduisant par une diminution du handicap de 83 %. Cependant une légère paralysie faciale et/ou des engourdissements des doigts ont pu être observés (de façon transiente pour 9 patients, et persistante après un an pour 4 patients).

Fin 2012, 4 patients souffrant de tremblements essentiels de la main ont également été traités à Toronto (Lipsman et al. 2013). Les cibles étaient dans le VIM du côté opposé à la main la plus affectée. La focalisation a été vérifiée par des échauffements modérés puis adaptée afin de ne pas affecter les zones sensorielles adjacentes. Les lésions ont été progressivement élargies en augmentant la puissance ou la durée des émissions (entre 12 et 29 fois, par incréments entre 0 et 2 °C et entre 10 s et 25 s) jusqu'à disparition des tremblements ou apparition d'effets négatifs. Des températures entre 56 °C et 63 °C ont été atteintes. Les tremblements ont fortement diminué lors du traitement ainsi qu'après trois mois. Néanmoins un patient a présenté lors du traitement une paresthésie (trouble des sensations liées au toucher) de la pointe du pouce, toujours présente après trois mois. Selon les auteurs cet effet secondaire serait associé à la lésion non souhaitée d'une zone sensorielle adjacente. De plus un autre patient a présenté une thrombose veineuse profonde qui serait, selon les auteurs, potentiellement liée à la durée du traitement.

Toutes les études menées entre 2009 et 2013 à 660 kHz ont été conduites avec le système Insightec visible sur la **Figure 1.11** (à gauche). Le système utilise une sonde HIFU hémisphérique, ce qui limite son positionnement par rapport à la tête et peut entrainer de grands angles entre l'axe des éléments et les normales géométriques du crâne. Une correction d'aberration simple est effectuée en utilisant un modèle du crâne basé sur son épaisseur et des tracés de rayons entre les éléments et la cible. Un système fonctionnant à plus haute fréquence (1 MHz) est actuellement développé à l’Institut Langevin en collaboration avec la société SuperSonic Imagine (Aix en Provence, France) (**Figure 1.11**, à droite). L’augmentation de la fréquence devrait limiter les risques de cavitation et diminuer la taille de la zone à traiter, ce qui devrait diminuer les effets secondaires liés au traitement ultrasonore du tremblement.

Figure 1.11:Systèmes pour les traitements transcrâniens de Insightec (Gauche, 660 kHz, installé à l'University of Virginia, Charlottesville, USA) et SuperSonic Imagine (droite, 1 MHz, installé à l'hôpital de la Pitié Salpêtrière, Paris, France).

1.3 Objectif de la thèse

L'objectif de cette thèse est de développer de nouveaux outils pour permettre le guidage de la première application clinique envisagée avec le système SuperSonic Imagine: le tremblement essentiel. Les deux techniques principales proposées ici sont :

- L'imagerie de force de radiation par IRM afin de localiser la focale du faisceau ultrasonore avec un échauffement minimal les tissus. Cette technique a été testée sur le système de thérapie installé à l'Hôpital de la Pitié Salpêtrière (**Figure 1.11**, à droite)
- La neuromodulation ultrasonore pour moduler réversiblement l'activité des tissus cérébraux et vérifier que la zone ciblée est bien responsable du tremblement. Cette approche a été testée dans cette thèse sur des modèles rongeur et primate avec un monoélément focalisé spécialement développé.

  Les principaux résultats sont résumés dans les sous parties suivantes.

1.4 Localisation des ultrasons par MR ARFI

L'Imagerie par résonance magnétique (MR ARFI) a été récemment présentée comme une méthode prometteuse pour contrôler et planifier les applications thérapeutiques des ultrasons focalisés de haute intensité guidés par IRM (MRgHIFU). Le MR ARFI mesure le déplacement induit par la force de radiation ultrasonore, et révèle l'emplacement de la tâche focale sans effets thermiques importants. Des cartes quantitatives de déplacements obtenues par MR ARFI fournissent une estimation indirecte de l'intensité du faisceau acoustique à la cible, ce qui est essentiel dans le cadre des procédures de HIFU transcrâniens. La Figure 1.12 détaille la séquence IRM utilisée pour encoder le déplacement. Un tir ultrasonore est nécessaire pour reconstituer une ligne de l'image, soit N tirs pour une image de N lignes.

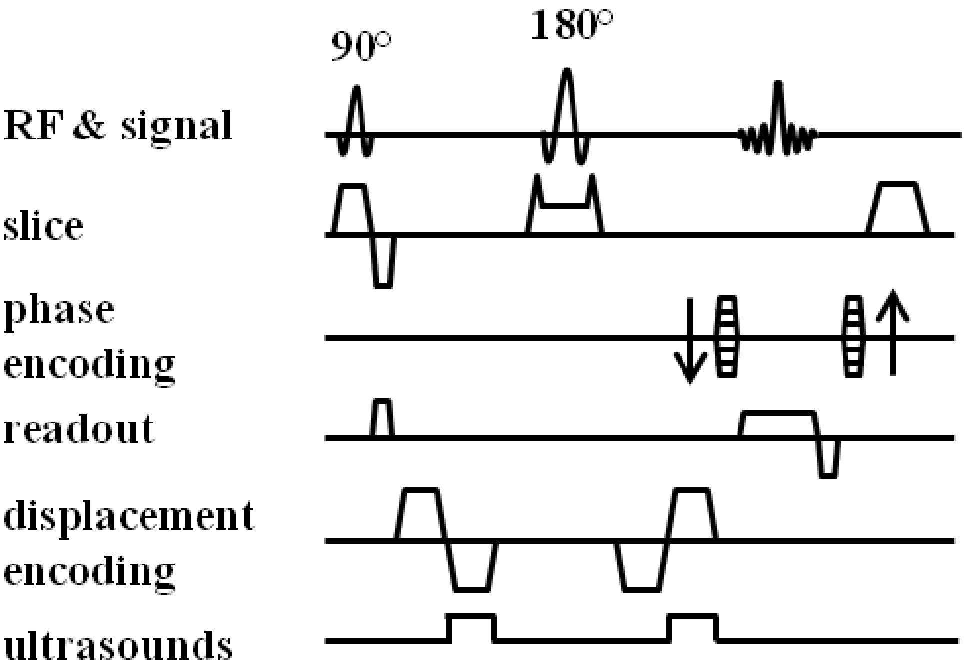

Figure 1.12: Diagramme de la séquence MR ARFI d'écho de spin 2D. Les tirs ultrasonores sont synchronisés avec la seconde moitié du gradient d'encodage des déplacements.

Les gradients de codage du déplacement peuvent être appliqués le long de l'axe de sélection de tranche (TRA, pour transverse), le long de l'axe de lecture (SAG (per) pour sagittal et encodage de phase perpendiculaire au faisceau), ou de l'axe d'encodage de phase (SAG (par) pour sagittal et encodage de phase parallèle au faisceau).

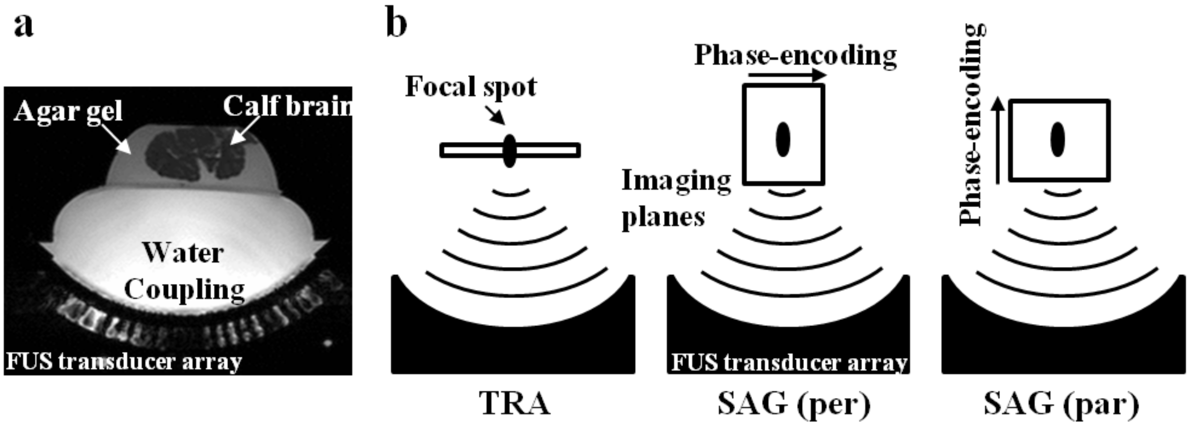

Figure 1.13(a, b): a- Sagittal view of the MRgFUS experimental setup. b- Imaging configurations tested in this work for MR ARFI keyhole acquisitions.

Une méthode de mise à jour partielle de l'espace des K, de type Keyhole, apparaît comme étant une méthode de choix pour minimiser le nombre de tirs ultrasonores et conserver l'innocuité de la technique dans le cadre d'une application clinique. Nous avons donc cherché à démontrer l'efficacité de la technique Keyhole dans l'acquisition des images MR ARFI, avec une distorsion d'image limitée.

La particularité de notre approche repose sur l'hypothèse que le profil de déplacement peut être décrit par une fonction gaussienne (Figure 1.14), qui est bien connue pour avoir des propriétés de transformation de Fourier simple. Typiquement, une large gaussienne dans l'espace image correspond à une gaussienne plus fine dans l'espace des K et vice-versa.

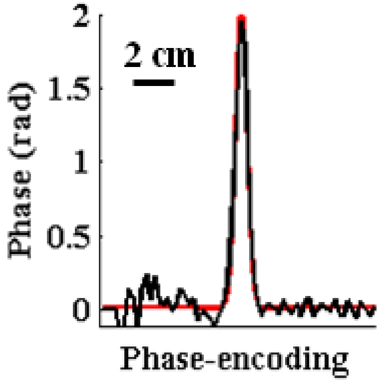

Figure 1.14: (ligne noire) profil expérimental du déplacement obtenu par MR ARFI (ici le long de la dimension de codage de phase avec R = 1). (Ligne rouge) fit gaussien.

Une séquence 2D d'écho de spin MR ARFI a été développée pour échantillonner une fenêtre Keyhole δk_y, avec $\delta k_y / \Delta k_y = 1 / R$, où Δk_y est la gamme complète de codage de phase et R l'accélération, encore appelé facteur Keyhole. Pour un facteur R= 2, la moitié seulement des lignes de l'espace des K a été acquise. Les autres lignes nécessaires à la reconstruction de l'image ont été prises sur une image de référence du même plan, acquise en l'absence de tir ultrasonore. L'acquisition des images a été réalisée sur un scanner (MR) 3T Siemens Verio (Siemens Healthcare, Erlangen, Allemagne). Les mesures ont été effectuées dans une cervelle de veau fraîche du commerce placée dans un gel d'agar (3 % en poids) préparé à l'aide d'eau dégazée. Une attention particulière a été portée pour éliminer des bulles d'air lors du placement de la cervelle dans le gel.

Les paramètres expérimentaux étaient les suivants : TE = 43 ms, TR = 900 ms. Les champs carrés de vision (FOV) de 160 × 160mm2 ont été acquis avec une taille de matrice 64 × 64 et une résolution isotrope de 2,5mm. Les données de référence sans impulsions US ont été enregistrées et les données de Keyhole ont été acquises avec des impulsions US de 5 ms. L'impulsion US a été émise au cours de la seconde moitié des gradients de mouvement de la séquence MR-ARFI (Figure 1.12) et a été générée avec le prototype à 1 MHz comportant 512 tranducteurs (SuperSonic Imagine, Aix en Provence, France).

La Figure 1.15 montre les images MR ARFI générées en changeant le facteur Keyhole R. Lorsque la direction d'encodage de phase est parallèle au faisceau ultrasonore (ce qui est le cas pour la configuration SAG (par) uniquement), l'image est le moins dégradé par l'augmentation du facteur R. Dans ce cas, les fréquences spatiales sont effectivement faibles car le gradient de champ ultrasonore est le plus faible dans la direction de propagation du champ.

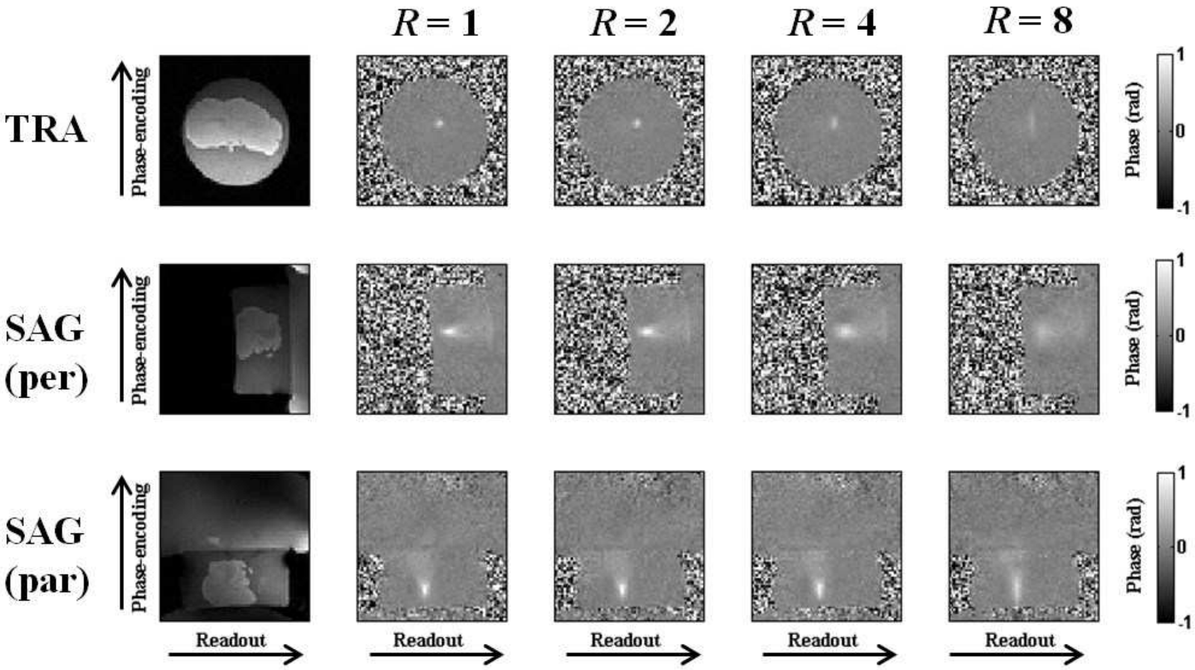

Figure 1.15: Images expérimentales MR ARFI Keyhole (phase) obtenues dans de la cervelle de veau en faisant varier les facteurs Keyhole R dans les plans d'imagerie transversales (TRA) et sagittal (SAG (per) et SAG(par)).

La Figure 1.16 confirme et quantifie les résultats de la Figure 1.15. Elle montre la phase φ_0 mesurée au foyer pour R variant de 1 à 8. Pour la vue TRA et SAG (per), φ_0 diminue de façon constante en fonction de R. Pour R = 2, φ_0 maintient plus de 90% de la valeur initiale, puis elle chute à 60-70% à R = 4 ou à 35-40% à R = 8. Pour le SAG (par), φ_0 reste presque inchangée de R = 1 à 4 (~ 95%), puis elle diminue à environ 70% à R = 8. La configuration de SAG (par) donne environ deux fois plus de signal par rapport à la TRA pour R = 8.

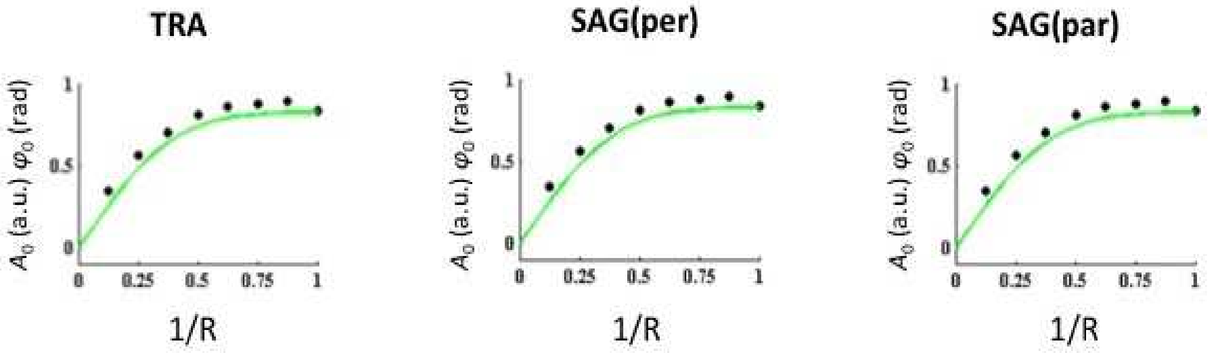

Figure 1.16: (Points noirs) maximum de phase φ_0 mesurées à la cible en fonction de l'inverse du facteur de Keyhole. (Vert) Simulation de l'évolution de l'amplitude A_0 d'un objet gaussien basé uniquement sur la propagation extraite de la régression. Les valeurs de φ_0 ont été utilisées uniquement comme des facteurs d'échelle

La simulation (en vert) montre que la perte de phase est bien prédite par la perte de signal lié à la dégradation de la gaussienne par la fenêtre utilisée pour le calcul de la transformée de Fourrier. La simulation pourrait donc être utilisée comme un outil de prédiction.

Nous le voyons, l'utilisation de la technique Keyhole pourrait permettre de diminuer le dépôt d'énergie ultrasonore d'un facteur 4 à 8 par pour visualiser le faisceau ultrasonore avant traitement.

1.5 Neuromodulation sur les rats

Une autre façon, plus intéressante encore, de planifier le traitement d'un tremblement essentiel pourrait être de moduler de façon réversible l'activité cérébrale avec le faisceau ultrasonore, jusqu'à être capable d'arrêter transitoirement le tremblement. On ne s'assurerait alors pas seulement que le traitement aura bien lieu sur la cible visée, mais également que la cible visée correspond bien à la zone responsable du tremblement. Or il a été montré que les ultrasons focalisés de basse intensité peuvent stimuler le cerveau d'une manière non invasive et sans dommage notable du tissu. Une telle neuromodulation, non invasive et localisée, pourrait avoir un impact majeur dans les années à venir. L'émergence de ce nouveau champ de recherche nécessiterait de nombreuses expériences sur des animaux afin de bien comprendre les mécanismes de stimulation ultrasonore. Le premier but de mes recherches était d'étudier la neuromodulation transcranienne par ultrasons de basse fréquence (320khz) sur des rats anesthésiés avec différentes pressions acoustiques. Ceci afin d'estimer la distribution *in situ* de la pression du champ et le seuil moteur correspondant. Etant donné que la distribution de la pression acoustique correspondant à l'intérieur du cerveau ne peut pas être mesurée *in vivo*, cette étude s'est basée en partie sur des simulations numériques de la propagation des ultrasons à l'intérieur de la cavité cranienne, afin de reproduire au mieux les conditions expérimentales réalisées dans la première partie, aussi bien en terme de géométrie de transducteur, de géométrie de la tête qu'en terme de paramètres acoustiques.

Dans cette étude, 29 sessions de neuromodulation ultrasononore ont été effectuées sur des rats (N=8) en utilisant un transducteur à 320khz.

Dans plus de 60% des expériences réalisées, les impulsions ultrasonores ont provoqué une réponse motrice. Dans toutes les expériences ayant induit une stimulation, celle-ci était reproductible jusqu'à un seuil de pression sous lequel aucune réponse motrice ne se produisait. Ce seuil de pression acoustique moyen avait une valeur de 0.68 ± 0.1 MPa (correspondant à un indice mécanique (MI) de 1.2 et une intensité moyenne spatiale et temporelle (Isppa) de 7.5 W.cm^{-2}), correspondant aux calibrations obtenues en champ libre dans de l'eau dégazée avec les mêmes tensions d'alimentation. Une légère variation a été observée entre une phase d'anesthésie profonde (0.77 ± 0.04 MPa) et une phased'anesthésie légère (0.61 ± 0.03 MPa), phases évaluées à partir du réflexe de la patte du rat à un stimulus mécanique externe. Plusieurs types de réponses motrices ont été observées telles que: mouvement de la queue, de la patte arrière, des pattes antérieures, de l'œil et même d'une seule moustache. Chacune de ces réponses a été induite séparément (**Figure 1.17**).

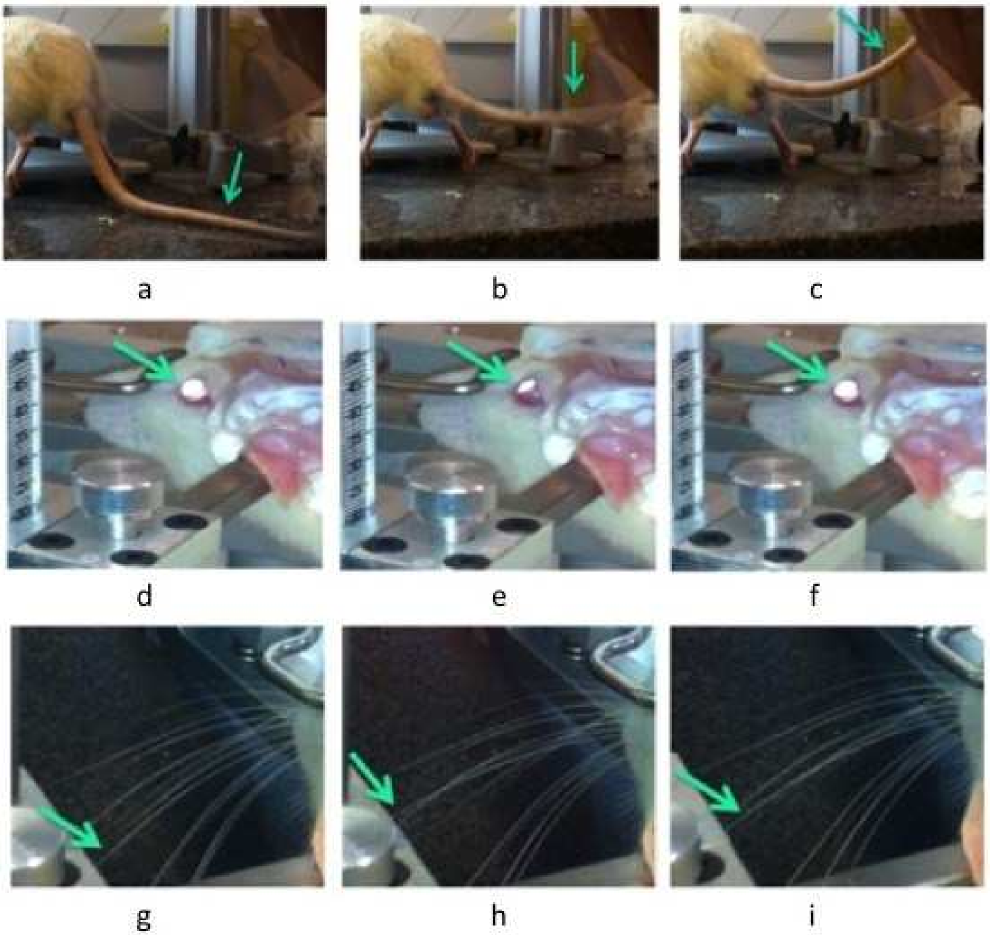

Figure 1.17(a, b, c): images successives de stimulations motrices de la queue. a-Avant ultrasons. b- pendant l'impulsion ultrasonore. c- Après la stimulation. (d, e, f): réponse motrice du système occulomoteur du rat. d- avant ultrasons. e- pendant l'impulsion ultrasonore. f- après l'impulsion d'ultrasons. (g, h, i): réponse motrice d'une seule moustache du rat. g- avant ultrasons. h- Pendant l'impulsion d'ultrasons. i- juste après l'impulsion d'ultrasons.

Le champ ultrasonore dans la tête de l'animal a été simulé afin de pouvoir évaluer la pression maximum in situ, ainsi que la distribution spatiale de pression. Les simulations numériques sont basées sur les données micro CT d'une tête de rat à partir desquelles sont déduites les propriétés acoustiques des os et des tissus mous. Les champs acoustiques simulés présentent plusieurs pics de pressions secondaires en raison de réverbérations de l'onde dans la cavité que constitue la tête du rat (Figure 1.18). Les champs acoustiques sont complexes à l'intérieur de la tête du rat : en conséquence, pour relier les effets de neuromodulation à des paramètres acoustiques dans le cerveau, il ne suffit pas de prendre en compte la simple atténuation du faisceau par le passage du crâne, en particulier pour l'étude sur les petits animaux et à basse fréquence. On mesure ainsi dans notre modèle une pression maximale temporelle et spatiale (Psptp) 1.8 fois plus grande dans la tête de l'animal que celle simulée dans l'eau en l'absence de crâne. L'intensité maximale temporelle et spatiale (Isptp) est mutipliée par 3.6 (± 1.8) comparativement aux simulations dans l'eau seule. La prise en compte de la seule présence de la première interface, comme cela est souvent fait, conduirait au contraire à estimer une pression plus faible dans le cerveau que dans l'eau en l'absence de crâne. La tête se comporte comme une cavité réverbérante qui amplifie la valeur du maximum de pression et complexifie la répartition spatiale du champ.

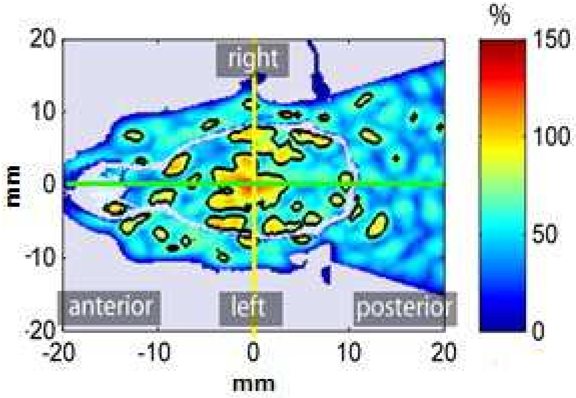

Figure 1.18: ***Simulations numériques dans le modèle de tête de rat à 320 kHz, normalisé par rapport à la focalisation dans l'eau***

La prise en compte de telles corrections dans les résultats précédemment obtenus expérimentalement nous conduit à une estimation de la moyenne du seuil de la pression acoustique dans le cerveau de 1.2± 0.3 MPa (MI=2.2 et Isppa =17.5 W.cm^{-2}) pour une neuromodulation motrice, à 320khz. Nous avons également mis en évidence que la stimulation ultrasonore transcranienne dépend non seulement du niveau de pression dans le cerveau mais également du niveau d'anesthésie du rat.

1.6 Neuromodulation sur singe éveillé

Le petit animal, de surcroît anesthésié, est donc un modèle plus complexe qu'il n'y paraît pour l'étude de la neurostimulation ultrasonore de basse fréquence. Dans ce travail de thèse, nous avons ainsi utilisé les ultrasons focalisés (FUS) afin de moduler la latence d'un paradigme d'anti saccade chez deux singes éveillés (Macaca Mulatta).

Les animaux ont été spécifiquement dressés pour un paradigme d'anti saccade (AS), dans lequel on leur demandait de fixer sur un stimulus central de couleur marron apparu sur un écran. Après la fixation, ce stimulus disparait et une cible latérale rouge apparaît à gauche ou à droite de l'écran. Les singes ont été entrainés à ne pas regarder cette cible latérale, mais initier le plus tôt possible une saccade dans la direction opposée **Figure 1.19**.

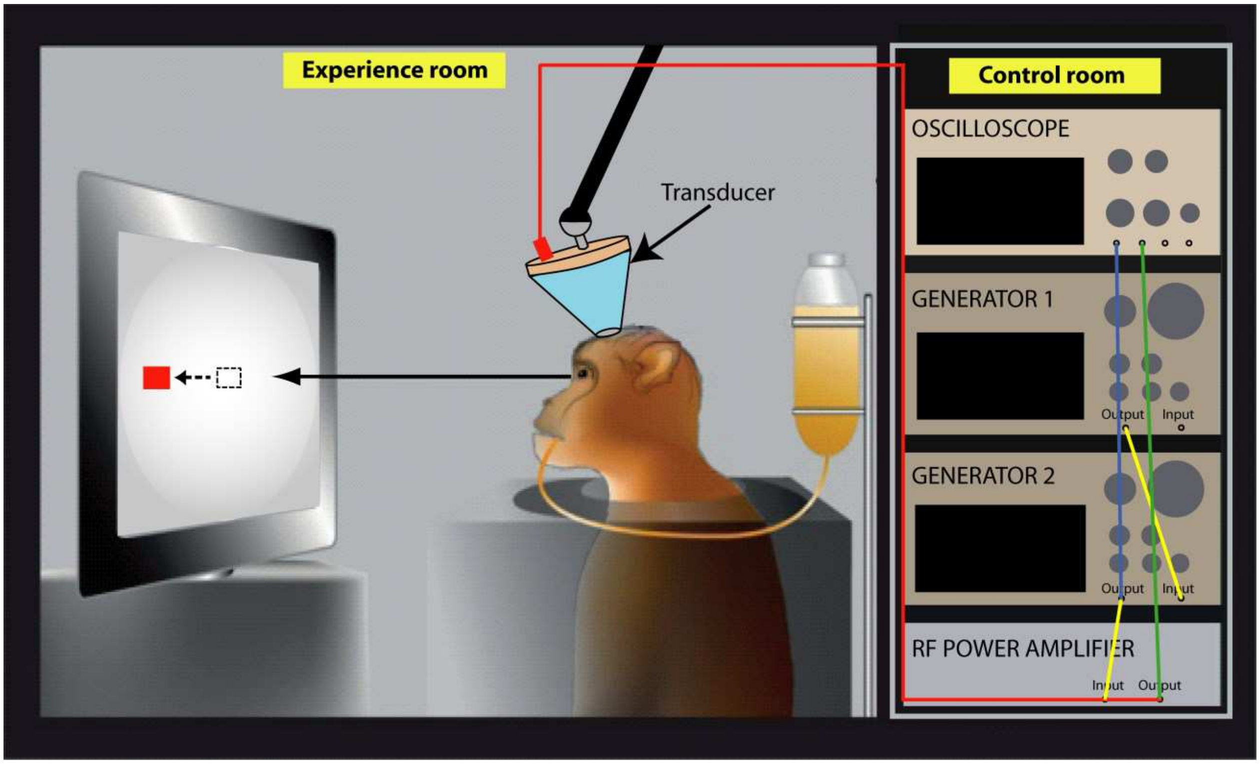

Figure 1.19: Dispositif de neuromodulation ultrasonore sur singe éveillé.

Les mouvements des yeux ont été enregistrés par un suivi oculaire infrarouge (Eyelink 1k, SR-Research, Ontario, Canada) et la position de l'œil a été enregistrée pour des analyses ultérieures. Dans une série de 23 expériences indépendantes, les animaux ont exécutés 3 blocs d'entrainement AS par session (**Figure 1.20**). Une ligne de base d'un bloc de 100 essais (50 gauche/50 droite) d'AS; des blocs de 400 essais (360 essais sans FUS (180 pour chaque côté) et 40 essai avec FUS (20 pour chaque côté) et un dernier bloc de 100 essais en tant que test post traitement. Le FUS consistait en une insonification de 100ms avec un transducteur à 320khz (H115, Sonic Concept, Bothell, WA, USA) focalisée sur le champ oculaire frontal (frontal eye field ou FEF) et identifié par ses coordonnées stéréotaxiques. La **Figure 1.20** schématise l'organisation des sessions. La pression dans le cerveau a été estimée à 0.35 ± 0.05 MPa (Ispta 13.46 ± 3.78 mW/cm^2), sur la base de mesure en cuve avec et sans crane de singe.

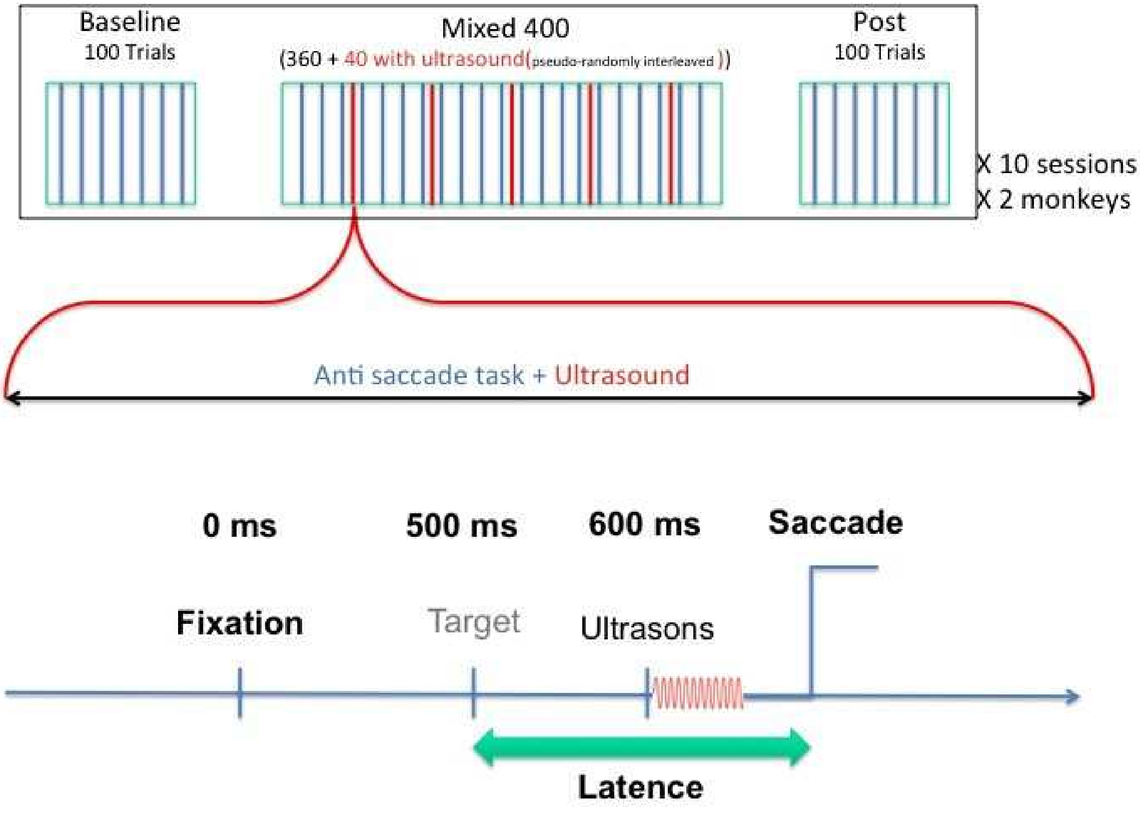

Figure 1.20: Les 3 blocs d'entrainement AS par session

Comme le montre la Figure 1.21, la stimulation ultrasonore ciblée dans le FEF gauche affecte les latences des anti saccades. Plus spécifiquement, durant les sessions expérimentales, la latence moyenne de l'anti-saccade ipsilatérale a été significativement ralentie par simulation ultrasonore (singe Y: p= 0.0018; singe L: p< 0.001), comparé aux cas non stimulés (singe Y: noUS= 221 ms US= 235 ms; singe L: noUS= 239 ms US= 269 ms).

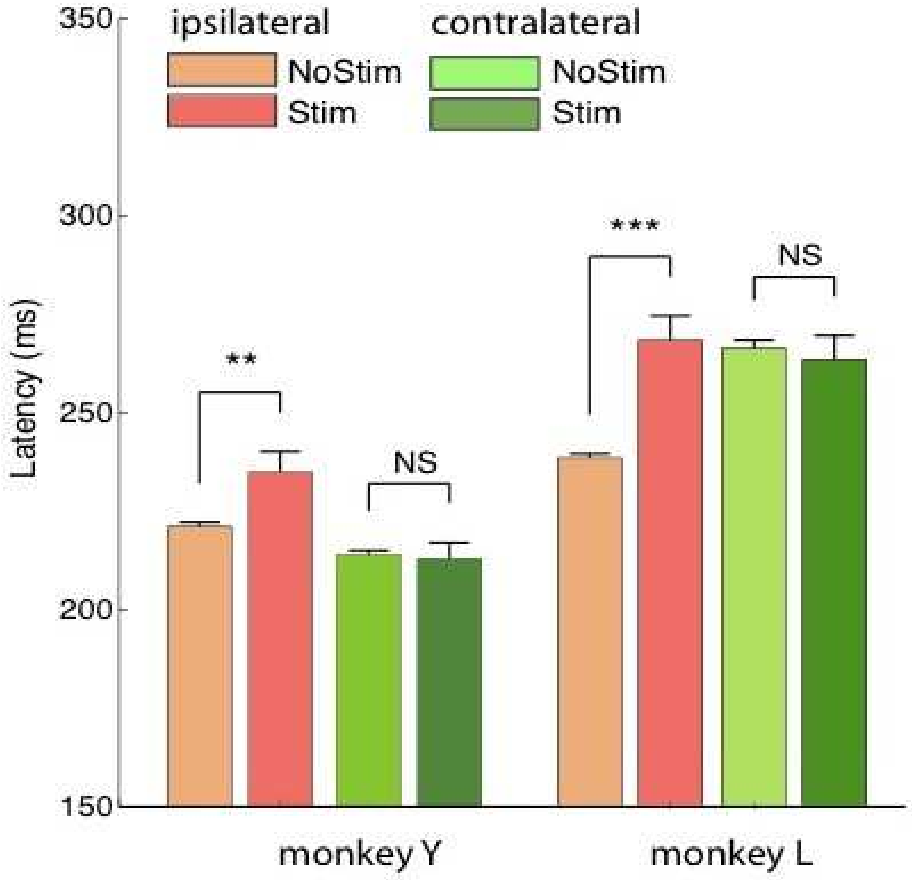

Figure 1.21: Latences moyennes des antisaccades Ipsilatérales et contralatérales avec et sans ultrasons sur les singes

Pour les 2 animaux, les latences moyennes des anti-saccades contralatérales n'ont pas été significativement ralenties (t-test: singe Y: p> 0.8; singe L: p> 0.6), comparativement aux cas sans ultrasons.

La stimulation utrasonore appliquée sur une zone contrôle (cortex pre-moteur) n’a affecté significativement ni les latences ipsilatérales (t-test: singe Y: $p > 0.69$; singe L: $p > 0.1$), ni les latences contralatérales (singe Y: $p > 0.11$; singe L: $p > 0.74$).

L’effet de la stimulation a été transitoire (pas d’effets significatifs observés sur les essais consécutifs ($p > 0,5$) pour les 2 animaux).

Dans le cas des pro-saccades, la stimulation ultrasonore n'affecte que marginalement les latences controlatérales, et ce pour un seul animal (respectivement $p < 0.001$ and $p > 0.52$).

Pour les deux singes, un sham d’ultrasons focalisés, calqué sur les sham d’expériences de Transcranial Magnetic Stimulation (TMS) a été mis en place : le transducteur était reculé de 3 cm et une couche d’air empêchait ainsi les ultrasons de pénétrer dans le cerveau. Aucun changements significatifs des latences ipsilatéralesou controlatérales ($p>0,5$) n'ont été observés.

L’étude démontre la faisabilité de la neuromodulation du cerveau par ultrasons focalisés de moduler d’une façon transitoire un processus cognitif avancé et conscient.

Chapitre 2 Introduction

2.1 Introduction

Ultrasound is a mechanical wave with a frequency higher than the upper limit of the human hearing range (**Figure 2.1**). An average man can hear sound frequencies between 20 Hz and 20,000 Hz, a range which narrows with age and is unique to each person.

Ultrasound is best known to the general public for its application in medical imaging. Ultrasound imaging has been used clinically for several decades. Its main advantages are cost, temporal and spatial resolution, and the absence of radiating effects. But ultrasound is not restricted to imaging and can also have therapeutic benefit as shown in this work.

Figure 2.1: Approximate frequency ranges corresponding to ultrasound

How ultrasonic waves can be generated?

Piezoelectric transducers convert electric energy into sound. A piezoelectric element with electrodes affixed on both sides oscillates by repeatedly expanding and contracting when a sinusoidal tension is applied, generating a sound wave (**Figure 2.2**).

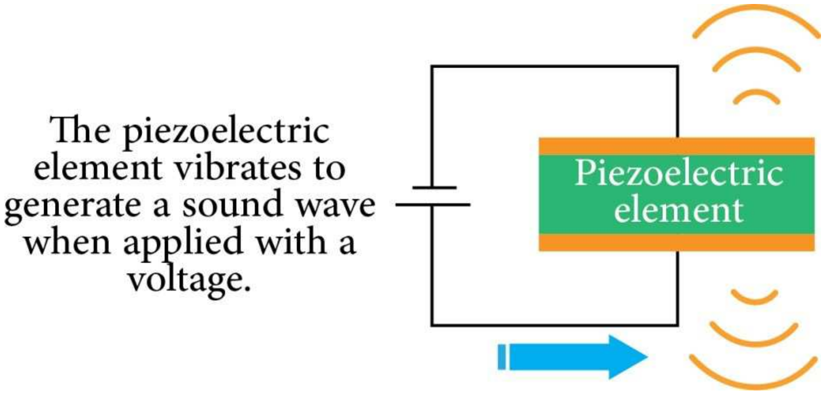

Figure 2.2: Sound wave generated by a piezoelectric element

A backing material is generally placed behind the piezoelectric element in order to reflect the wave on the back and reinforce the wave emitted by the front face (Figure 2.3).

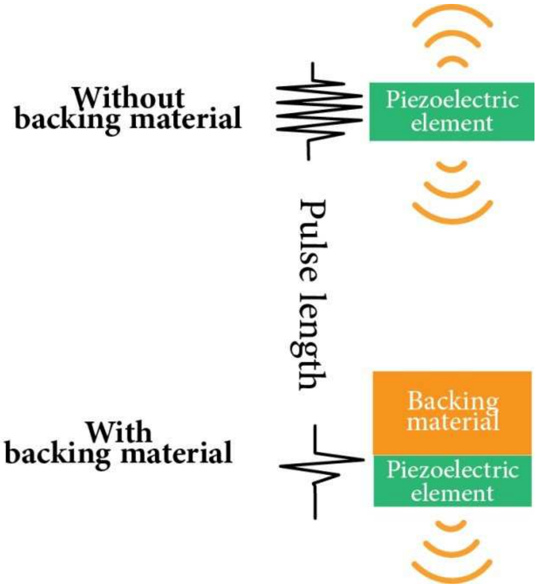

Figure 2.3: Function of the backing material behind the piezoelectric element

Generated ultrasonic waves are transmitted from the piezoelectric element into the patient. Any difference in acoustic impedance on the path will reflect ultrasound and potentially prevent ultrasonic waves from reaching their target. In particular, the wave is completely reflected in the presence of air. To avoid this phenomenon, an intermediate echographic gel is placed between the piezoelectric element and the tissues (**Figure 2.4**), so that transmission is optimum.

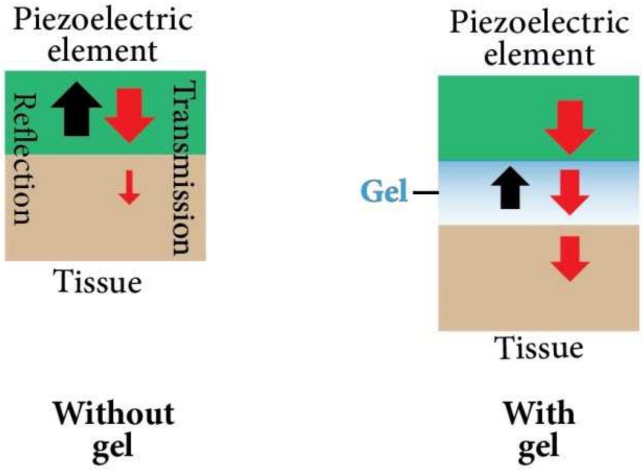

Figure 2.4: Ultrasonic waves transmitted with and without gel

Waves generated within tissue are longitudinal (L-Waves, **Figure 2.5**), where the particle movement is in the same direction as the wave propagation.

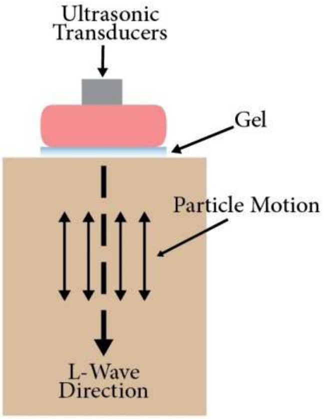

Figure 2.5: longitudinal wave

The pressure waves (positive compression and rarefaction negative) are thus propagated in the human body. Pressure is related to particle velocity through the medium acoustic impedance:

$$\boldsymbol{P} = \boldsymbol{Z} \times \boldsymbol{\upsilon}$$

Where Z is the medium acoustic impedance and υ is speed particle displacement.

The amplitude of pressure P_0 is the maximum pressure generated, usually expressed in MPa.

Other parameters are used to fully characterize the ultrasonic pulse (**Figure 2.6**), and are widely used in this manuscript.

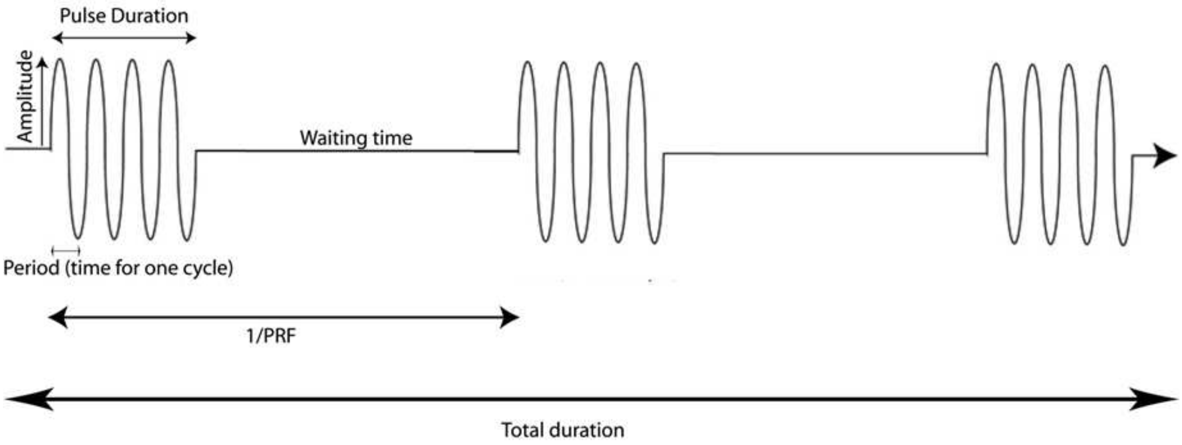

Figure 2.6: ultrasonic parameters

- Pulse duration: the time required for one single pulse to occur.
- Pulse repetition frequency (PRF): the number of pulses occurring in 1 s.
- Duty cycle: Percentage of time that ultrasound is being generated (pulse duration) over the pulse repetition period

The wavelength is the distance between maximum of two compressions or rarefaction and depends on the frequency transmitted and the speed of sound in the propagation medium according to the following formula:

$$\lambda = \frac{c}{f}$$

Where c is the speed of the wave; measured in m.s^{-1} and f is the frequency (the number of times a particle oscillates per second).

The higher the frequency, the lower the wavelength and the shorter the penetration depth due to higher attenuation.

Focused Ultrasound

Ultrasonic transducers for medical therapy have shapes and dimensions adapted to the organ for which they are designed. In general, they have a spherical shape in order to focus ultrasound at the target (Figure 2.7), as do the transducers which were used in this work for neuromodulation on rodents and primates.

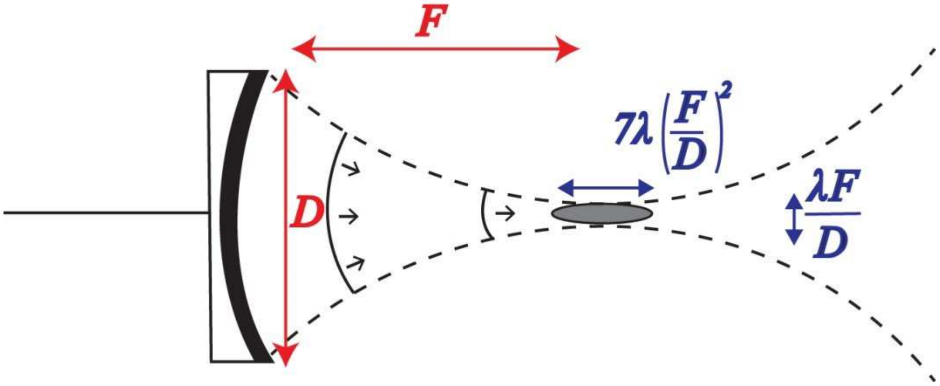

Figure 2.7: Focused ultrasound transducer by one spherical piezoelectric element

The focal spot size is determined by the geometry of the transducer (aperture D) and the depth (F) of the target. It typically has the shape of an ellipsoid (length: λF/D and depth: 7λ(F/D)²).

Transducers can also be comprised of many elements (Figure 2.8) in order to achieve electronic beam steering out of the geometrical focus or perform aberration correction (for human transcranial treatments for example). We used such a multielement transducer for accelerating Magnetic Resonance Imaging Acoustic Radiation Force (MR ARFI) with a Keyhole technique.

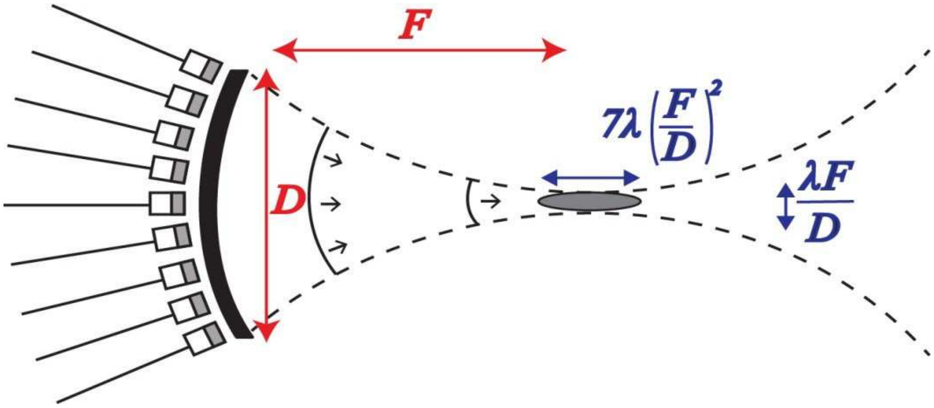

Figure 2.8: Multielement focused ultrasound transducer

Sound intensity refers to the power of a sound wave per unit area (Figure 2.9). The average acoustic intensity at focus over a period is given by the formula:

$$\mathrm{I} = \frac{{P_0}^2}{2Z}$$

Where P_0 is the pressure amplitude of the impedance Z in the medium. It is expressed in watts per square meter (W / m² or W · m-2)

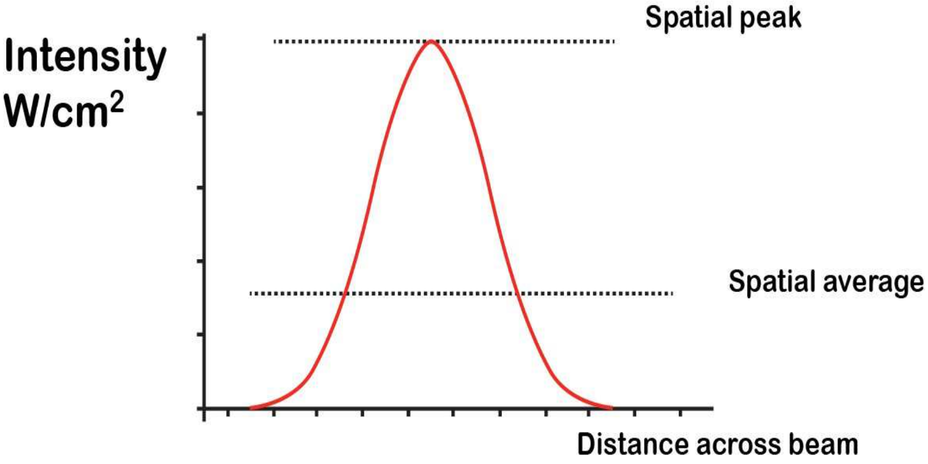

Figure 2.9: The profile of the intensity as a function of the distance

Intensity varies with time when using pulsed ultrasound (**Figure 2.10**) and the following definitions are commonly used:

- Temporal peak (TP) is the greatest intensity found in a pulse.
- Temporal average (TA) includes the "dead" time between pulses.
- Pulse averaged (PA) intensity pulse averaged intensity is the average intensity during the "on" time period of the pulse only.

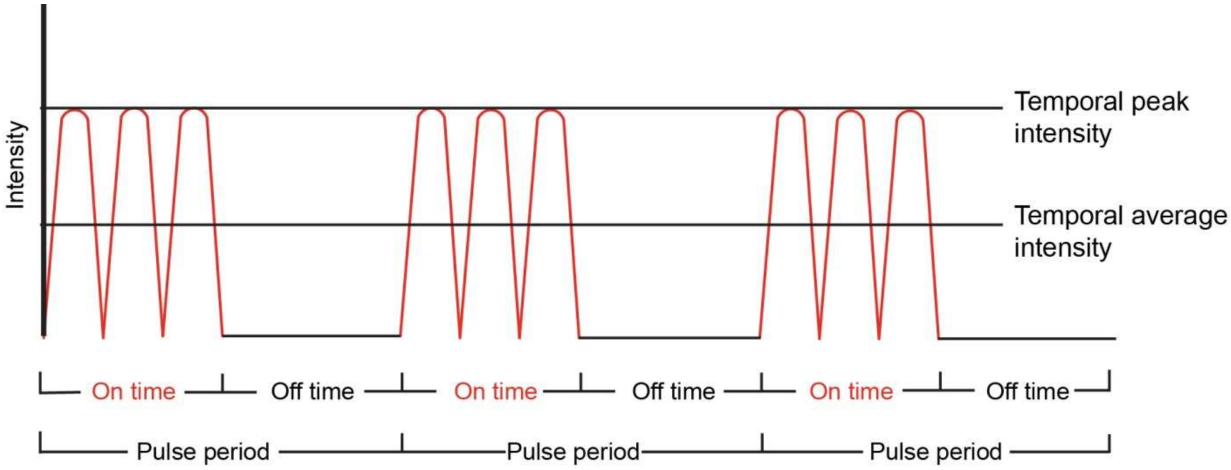

Figure 2.10: The profile of the intensity versus time

The acoustic intensity is important when discussing biological effects and safety. Ultrasound interacts with biological tissues via two main mechanisms: thermal and mechanical.

Thermal effects are related to the absorption of ultrasonic waves by the tissue. In tissues, thermal energy deposition per unit of time is proportional to the acoustic intensity and to the frequency.

Mechanical effects are of several types. The acoustic vibration itself causes movement of the tissue of a few tens of nanometers at the ultrasonic frequency. But other more complex effects exist, such as the generation of a radiation force proportional to the average acoustic intensity. This force induces tissue displacement of few tens of microns with a low frequency, through transfer of momentum. Finally, acoustic cavitation can occur, corresponding to the stable or inertial oscillation of microbubbles (either injected or generated spontaneously). The mechanical index (MI) has been introduced to evaluate the risk associated with cavitation effects and is defined by:

$$\mathrm{MI} = \frac{PNP}{\sqrt{F_c}}$$

Where PNP is the peak negative pressure of the ultrasonic wave (expressed in MPa) and Fc is the center frequency of the ultrasonic wave (expressed in MHz)

Like all interactions, beyond a certain threshold they can cause serious tissue damage, up to its partial or total destruction. Thermal absorption can cause tissue necrosis and inertial cavitation can literally tear cellular tissue, causing cell necrosis. These two effects are exploited respectively in HIFU (High Intensity Focused Ultrasound) and histotripsy. In the context of the use of ultrasound imaging, strict standards are imposed on manufacturers to ensure the safety of the ultrasound sequences used.

Nevertheless we also know that, at intermediate powers, thermal and mechanical effects also have physiological effects that do not necessarily put the tissue at risk and allow important medical applications. An example is the opening of the blood-brain barrier (BBB) using focused ultrasound and co-injection of contrast agents (microbubbles of gas, air, nitrogen or perflurocarbon): it allows molecules to enter the brain, that would normally be blocked because of their size (> 400 Da). The opening is noninvasive, transient and localized. It is believed to rely on stable cavitation (Tung et al., 2010)(McDannold, Vykhodtseva, and Hynynen 2008)(Tung et al. 2011) which do not cause visible damages on histological sections.

A similar effect is sonoporation, allowing transient change in cell membrane permeability by ultrasound. This technique is used in particular to allow the local penetration of molecules too large to pass through the membrane itself(Deng et al. 2004), such as DNA fragments used for in vivo gene therapy. The addition of microbubbles promotes sonoporation, similarly to BBB opening.

In addition, ultrasound has been shown to be able to produce nervous peripherical stimulation and reversible inhibition of electrical activity for decades. In the 30s, Harvey was the first to demonstrate the potential of ultrasound to stimulate nerves and muscle fibers (Harvey 1930). Other experiments of stimulation or inhibition of ultrasonic nerves or muscles followed: the saphenous nerve of the cat in vitro (Young and Henneman 1961), in vitro preparations of peripheral nerves of frogs (Lele 1962)(Mihran, Barnes, and Wachtel 1990)(Tsui, Wang, and Huang 2005), in vivo nerves of the hand in humans (Davies and Gavrilov 1996), in vivo spinal cat (Shealy and HENNEMAN 1962).

On brain tissue, Fry showed in the 50s that the response induced by a visual stimulus could be reversibly inhibited in the primary visual cortex of the cat by focusing ultrasound in the lateral geniculate body (W. Fry et al. 1958). The existence of auditory sensations in patients undergoing a transcranial Doppler of the basilar artery has also been reported (Magee and Davies 1993). Experiments on slices of rodent and seahorses directly measured the influence of ultrasound on the amplitude of action potentials and have shown an increase or decrease in the amplitude as a function of ultrasonic power (Rinaldi et al. 1991). It is not, strictly speaking, direct stimulation by ultrasound but a modulation of the excitability of neurons.

Recently, the U.S. team of William Tyler has demonstrated the possibility of inducing a direct neuromodulation with low acoustic pressure (Tyler et al. 2008). This has two novel aspects:

- the ability to directly stimulate neurons and not only modulate neuronal excitability

- the use of low acoustic pressure, that is to say, with minimum risk of damaging brain tissue.

Action potentials generated by low-frequency low intensity ultrasound were recorded by electrophysiology, first in slices of mouse hippocampi (Tyler et al. 2008) (whole-cell current patch clamp) and *in vivo* in mice (local field potentials or LFP) (T. Tufail et al. 2010)(Y. Tufail et al. 2011). The opening of calcium channels was observed in slices by confocal microscopy. In mice *in vivo*, without craniotomy, muscle twitching was observed and recorded by electromyography (EMG) when insonification was performed in the motor cortex.

Similar work has been published later by the Seung Schick Yoo's team on rabbits (with craniotomy) with similar results (Yoo et al. 2011). Yoo used an MR-compatible transducer and performed functional MRI during ultrasonic neuromodulation. Functional MRI provided direct visualization of the target area, i.e. the motor cortex. Yoo et al also used visual evoked potentials (light stimulation) to highlight the inhibition of neuronal activity in the visual cortex, first by analyzing the p30 component of the EEG signal (30ms positive peak) and second by the decrease of Bold signal on fMRI images. For inhibition, Yoo used shorter ultrasonic pulses while increasing the total insonification time (9s), keeping the pressure and ultrasonic frequency unchanged. Under these conditions, histology showed no damage of the targeted area and MRI was used to confirm the integrity of the blood-brain barrier (Gadolinium) and the absence of temperature elevation (< 0.8 ° C).

2.2 Transcranial HIFU

Transcranial HIFU therapy has the advantage of being non-invasive and thus allows the treatment of patients for whom operation are not safe. Accuracy is typically of the order of a millimeter. In addition, temperature elevation used in thermal ablation can be measured with dedicated MRI sequences to verify the proper course of the treatment.

The non-ionizing nature of this approach is an advantage in terms of simplicity of implementation and integration. The absence of radiation allows repeated treatments if necessary, unlike radiotherapy treatments.

Note the potential benefits of the procedure on the developing brain of children, more sensitive to ionizing radiation(Goske et al. 2008)(Duffner et al. 1993). The impact in terms of public health and comfort for the patient could be very beneficial, especially because such equipment helps overcome potential risks of both surgery (infection, bleeding, etc.) and ionizing radiation (radioprotection, etc.) and also because its cost is expected to be lower than stereotactic radiosurgery.

Recently, the first clinical trials with a frequency of 660 kHz have been performed with a system developed by Insightec to address different pathologies of the brain. They used a hemispherical HIFU probe, which distributes the energy over the largest skull surface possible but consequently limits the position of the probe in regard to the head and can cause large angles between the axis of the elements and the normal of the skull surface. Coupling is performed with water without any membrane between the probe and the head along the beam path, for better transmission. It is attached to a stereotactic frame and can be translated. Aberration correction is performed using a CT-derived model of the skull and based on ray tracings between the elements of the array and the target, taking into account the skull thickness.

In 2009, a first clinical trial on glioblastomas was performed on three patients using this system. However the maximum temperatures reached after 20 s emissions were too low (C 42 ° , 48 ° C and 51 ° C for each patient) to generate a significant treatment effect (McDannold et al. 2010).

The same year, eleven patients were treated for chronic neurogenic pain resistant to existing therapies (Martin et al. 2009)(Jeanmonod et al. 2012) . Patients were sedated but aware, regularly interviewed during surgery, as well as under conventional monitoring. Regions of 3 mm to 5 mm in diameter were generated in the posterior area of the central thalamic nucleus. Moderate heating with temperature varying between 39°C and 42°C was used to verify the location of the targeting. Treatment involved exposure to acoustic powers between 800W for 20s and 1200W for 10s. Temperatures of 51°C to 64°C were reached. Patients experienced a varying decrease of pain immediately after the procedure. The effect persisted for one year, as confirmed by improved electroencephalographic (EEG) measurements. However, for one patient, a case of cerebral hemorrhage coupled with ischemia was detected by MRI causing side effects still present one year after treatment (Jeanmonod et al. 2012). According to the authors, cavitation or excessive temperature (64°C measured) could be the cause.

Between 2011 and 2012, 15 drug-resistant patients participated in a phase I study on essential tremor with the same device (Elias et al. 2013). The treatment consisted of a thalomotomy of the ventralis intermediate nucleus (VIM). The maximum temperatures reached varied between 55 and 63 ° C and successive thermal rises were repeated until the tremor decreased. The results showed an average decrease of the tremor of 67% one year after treatment, resulting in a reduction of disability of 83%. However, a mild facial paralysis and numbness of the fingers were observed in some cases (transiently for 9 patients, and persistent after one year for 4 patients).

At the end of 2012, four patients with essential tremor of the hand were also treated in Toronto (Lipsman et al. 2013). The targets were in the VIM opposite to the most affected hand. The focus was verified by moderate heating and adapted so as not to affect the adjacent sensory areas. The lesions were gradually extended by increasing the power or duration of emissions (between 12 and 29 times in increments between 0 and 2 °C and 10 s and 25 s) until the disappearance of tremor or occurrence of adverse effects. Temperatures between 56 °C and 63 °C were reached. The tremors decreased significantly during treatment and after three months. However paresthesia at the tip of the thumb occurred in one patient during treatment, still persisting after three months. According to the authors, this side effect is associated with undesirable sensory area of an adjacent lesion. Another patient had a deep vein thrombosis which, according to the authors, was potentially linked to the duration of treatment.

All studies conducted between 2009 and 2013 at 660 kHz have been conducted with the ExAblate 4000 Insightec system displayed in Figure 2.11(left). A system operating at a higher frequency (1 MHz) is currently developed at Institut Langevin in collaboration with SuperSonic Imagine (Aix en Provence, France) (Figure 2.11, right). Increasing the frequency should decrease the risk of cavitation events and decrease the treated volume. Both are expected to lower side effects during essential tremor treatments. I used the 1MHz prototype for the experiments on MR ARFI optimization: MR ARFI will be used in the future to help guide the treatment.

Figure 2.11: Systems for transcranial treatments Insightec (Left, 660 kHz) and SuperSonic Imagine (right, 1 MHz).

At Institut Langevin, the first clinical trials are envisioned to be on essential tremor. The treatment planning and target accuracy has been tested recently on sixteen cadavers(Chauvet et al. 2013): the neurologist selected the targeted area (the ventral intermediate (VIM) nucleus), from a T1 weighted image of the brain and the planning software automatically computed the position of the array and phase corrections to apply to individual elements. MR temperature imaging was performed to image the temperature elevation during sonication. A millimetric accuracy was found between the location of the maximum temperature elevation and the location of the target.

The objectives of the work described in this thesis are first to investigate a new method for minimizing energy deposition when localizing the ultrasonic beam in the brain, using an accelerated MR acquisition technique. The second objective is to investigate ultrasonic neuromodulation, which has only been tested on anesthetized rodents in the literature, by doing experiments first in an anesthetized rat model to investigate the motor threshold and ultrasonic field and then, for the first time, in awake monkeys in order to advance toward potential future clinical applications such as better targeting of the essential tremor focus, or treatment of other brain disorders similarly to that currently achieved with transcranial magnetic stimulation (TMS).

Chapitre 3 Keyhole Acceleration for Magnetic Resonance Acoustic Radiation Force Imaging (MR ARFI)

3.1 Introduction

Magnetic Resonance Acoustic Radiation Force Imaging (MR ARFI) (McDannold and Maier 2008) has recently been introduced as a promising method to plan and monitor therapeutic applications of magnetic resonance guided focused ultrasound (MRgFUS). MR ARFI measures the displacement induced by the radiation force that accompanies the acoustic beam, and provides the location of the focal spot without significant heating effects. The displacement is MR encoded into the phase. Quantitative displacements maps obtained with MR ARFI are used as an optimization parameter in MR-guided adaptive focusing procedures (Larrat, Pernot, Montaldo, et al. 2010)(Hertzberg et al. 2010). The heterogeneous nature of biological tissues induces the distortion of acoustic waves which can result in severe degradations of the focusing pattern. In particular, transcranial (Tanter et al. 2007) (Pernot et al. 2007) or transcostal (Aubry et al. 2008) FUS is hampered by the large disparity between speed of sound in bone versus that in tissue, which leads in turn to a spreading of the focal spot and a lowering of the pressure at the focus. Adaptive focusing techniques can restore the focusing quality by estimating and applying a phase correction to each element of the ultrasonic array. To obtain the phase corrections, MR-guided adaptive focusing methods (Larrat, Pernot, Montaldo, et al. 2010) rely on the indirect estimation of the acoustic wave at the target by transmitting at least 3N Hadamard-coded ultrasound signals, with N the number of elements of the array that typically ranges from 256 to 1024. Hence, a large number of serial MR ARFI images (a minimum of 768 images) must be acquired for the full procedure. It is thus of primary importance to offer fast MR ARFI techniques in order to reduce the total scan time. In addition, a low number of acquisitions or scans is desired to ensure minimal heat deposition during the focus restoration, as ultrasonic sonication is required for each MR acquisition of the radiation force.

MR ARFI can also be used for beam localization with low energy before switching to ablative sonications. Again, minimizing the number of sonications to acquire an image is important to minimize energy deposition.

MR ARFI has already been performed using dedicated MR pulse sequences, such as line-scan(McDannold and Maier 2008), two-dimensional gradient-echo (Huang et al. 2009) or spin-echo(Larrat, Pernot, Montaldo, et al. 2010)(Larrat, Pernot, Aubry, et al. 2010). The technique has recently found its rapid expression in the development of single-shot echo-planar imaging (EPI) versions (Hertzberg et al. 2010)(Kaye, Chen, and Pauly 2011). The EPI method is an accelerated technique that could be suited for adaptive focusing. However it requires the use of long echo-times (TE) and high bandwidth values, which unavoidably decrease the signal to noise ratio (SNR) and thus require larger displacements and higher pressure levels. Adaptive focusing requires substantial SNR in MR ARFI images to estimate the phase corrections accurately (Marsac et al. 2012). Single-shot MR ARFI echo-planar images also suffer from inherent geometric distortions arising from magnetic field inhomogeneities and fail to provide very accurate localization of the focal spot.

To reach a compromise between SNR, high spatial resolution, limited geometric distortions, and reduced total scan time, a partial k-space updating technique, such as “keyhole” (Van Vaals et al. 1993)(Jones et al. 1993), may be a method of choice. The dynamic imaging keyhole technique was originally introduced as a technique to follow the uptake of contrast agent rapidly (Van Vaals et al. 1993)(Jones et al. 1993). Keyhole was rapidly extended to cardiac MRI (Doyle et al. 1995)(Suga et al. 1999) and has been used to improve the temporal resolution of functional MR imaging (Gao et al. 1996)(Xiong, Fox, and Gao 1999), diffusion tensor imaging in mouse brains (Sun et al. 2010), MR elastography(Murphy et al. 2010), MR thermometry(Han and Mun 2011), interventional MRI (Duerk, Lewin, and Wu) or chemical exchange saturation transfer imaging(Varma, Lenkinski, and Vinogradov 2012). The technique relies on the fact that the low spatial frequencies contain the coarse appearance of an image, while the contours and the fine contrast are provided by the higher frequencies. A keyhole acquisition updates only a central subset of k-space lines, which is then merged with complementary peripheral lines taken from a previously recorded reference image. Keyhole is particularly suitable for accelerating 2D gradient-echo or spin-echo acquisition, whose times of acquisition (TA) are determined by the number of phase-encoding steps. The temporal gain increases linearly with the number of outer lines shared between the reference and the dynamic images. However, the keyhole technique must be employed with caution since it provides only a low resolution image of the updated or changing data (Hu 1994). Truncation artifacts appear when the change contains high-spatial frequency components in the phase-encoding (PE) direction and significant intensity drops occur for small dynamic objects when the number of shared lines is too high (Spraggins 1994).

In this thesis, we demonstrate the efficiency and the advantages of keyhole acquisitions for a 2D spin-echo MR ARFI pulse sequence used in the context of MR-guided adaptive focusing preparation (Clement and Hynynen 2002)(Botros, Ebbini, and Volakis 1998) and target visualization, for essential tremor treatments with the 1MHz device. The uniqueness of our approach relies on the a priori knowledge of the dynamic object, since the profile of the displacement induced by ultrasound bursts can be described by a Gaussian shape (Sarvazyan et al. 1998). A Gaussian function is well-known to have straightforward Fourier Transform (FT) properties; typically a broad Gaussian in the image space generates a sharp Gaussian in the k-space and vice-versa. First, we hypothesize and demonstrate that the spread, i.e., the size, of the Gaussian profile in the PE dimension is the key parameter affecting the keyhole technique in a predictable way for a spin-echo MR ARFI sequence. We show via simulations and experiments the importance of adequate choice of the imaging plane and the PE direction with respect to the ellipsoidal shaped ultrasound focal spot to take full advantage of the keyhole technique. We show how well the displacement profile and maximum intensity at the target are preserved when increasing the number of shared lines and thus the acceleration factor. All experiments of this proof of concept have been performed in an ex-vivo calf brain.

3.2 MR ARFI

MR ARFI measures the quasi-static displacement induced by the ultrasonic radiation force at the focus(McDannold and Maier 2008). The diagram of the 2D spin-echo MR ARFI pulse sequence used here is presented in **Figure 3.1**. The displacement is MR encoded into the phase using gradients applied along the direction of the ultrasound beam (corresponding to the direction of the induced tissue displacement). Repeated bipolar displacement encoding gradients were used to cope with artifacts originating from bulk motions and eddy currents and to enhance the signal to noise ratio (SNR) (Chen, Watkins, and Pauly 2010). The ultrasound bursts were emitted during the second lobe of the displacement encoding gradients and were generated with an MR compatible 1 MHz 512 channel prototype of ultrasonic brain therapy (SuperSonic Imagine, Aix en Provence, France). The amplitude of the gradient was set to $|Ge|$ = 20 mT/m. The duration of each lobe was τ = 5 ms. each pair of displacement encoding gradients is shifted symmetrically away from the refocusing pulse by a 4 ms delay.

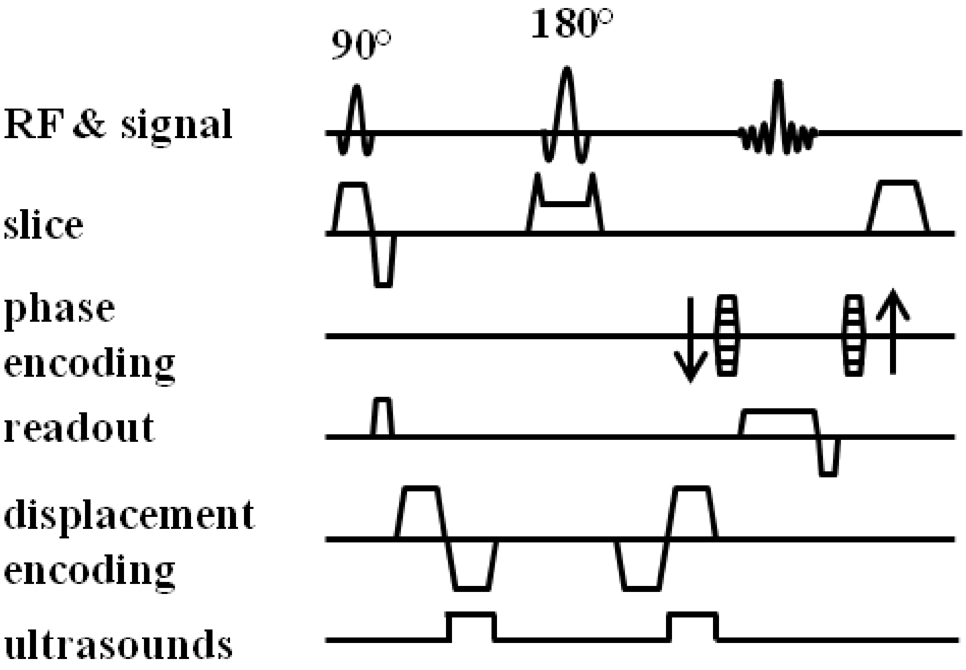

Figure 3.1: Diagram of the 2D spin-echo MR ARFI pulse sequence used for keyhole acquisition. The displacement-encoding gradients can be applied along the slice-selection axis, the readout axis or the phase-encoding axis. The ultrasound bursts are synchronized with the second half of displacement-encoding gradients.

This configuration minimizes the encoding of motion due to the first ultrasound burst during the first lobe of the second displacement encoding gradient and augments the SNR. To obtain absolute displacements maps, a pair of phase images is generally acquired with displacement encoding gradients applied with opposite polarity to double the sensitivity(McDannold and Maier 2008). Subtraction of the two acquisitions ensures removal of background phase variations originating from magnetic field inhomogeneities. In this work, a single reference phase image was acquired with identical imaging parameters but without ultrasound emission. The phase difference $\Delta\varphi$ between the acquisitions obtained with ultrasound emission and the reference acquisition can be translated to a displacement map as:

$$\Delta d = \frac{\Delta\varphi}{\gamma G_e \tau}$$

where Δd is the displacement and γ is the gyromagnetic ratio of protons. For the sake of simplicity, only phase difference maps are presented and discussed in this work. Figure 3.2a displays a typical phase map obtained in a 4% w/w ex-vivo calf brain immersed in an agar gel using a MR ARFI spin-echo sequence at 3T (FOV size: 128×128 mm2, resolution 2×2×7 mm3, matrix size 64×64, TE = 43 ms and TR = 900 ms). The focal spot is a three-dimensional anisotropic ellipsoidal object. The displacement can be described in any of the three MR main axes by a Gaussian profile (Sarvazyan et al. 1998). Depending on the chosen axis, the displacement profile is sharp (smallest axis of the ellipsoid) or broad (longest axis). Figure 3.2b shows one-dimensional maximum displacement profiles taken from Figure 3.2a and along the two imaging axes. The excellent agreement between the experimental profiles and a non-linear least square fit using a Gaussian function supports this hypothesis. Note that Figure 3.2a shows a transverse plane in which the focal spot is isotropic, giving phase profiles with similar spreads.

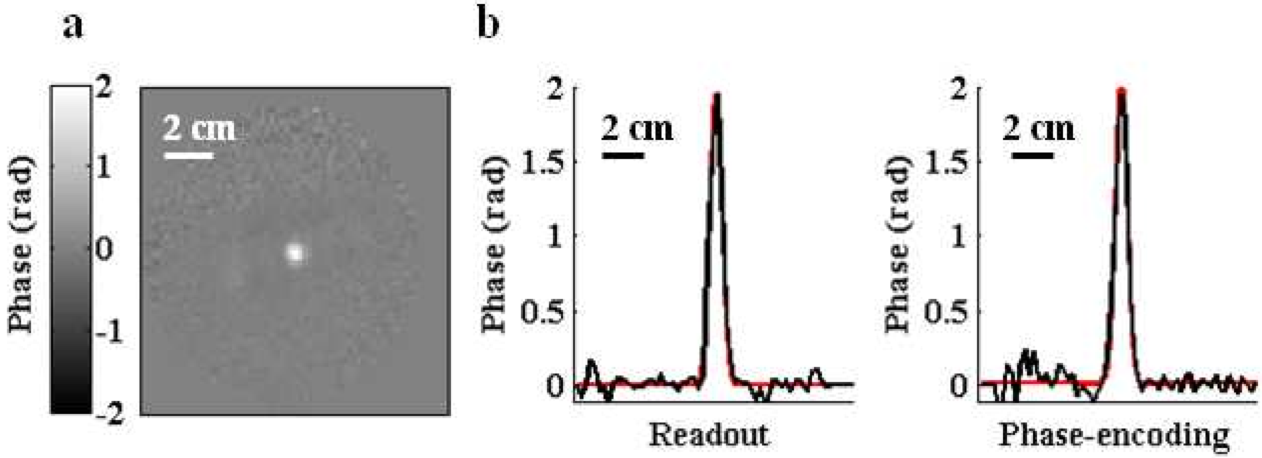

Figure 3.2 (a, b): a- Phase difference image obtained with a MR ARFI spin-echo sequence at 3T (transversal imaging plane). The imaging parameters were: FOV size: 128×128 mm^2, resolution 2×2×7 mm, matrix size 64×64, TE = 43 ms and TR = 900 ms. The background air noise has been removed by applying a mask created from the magnitude image (not shown). b- 1D phase profiles of the focal spot in readout and phase-encoding dimensions (black). Non-linear least square fit using a Gaussian function (red).

3.3 Influence of the human skull on displacement profiles

To investigate the influence of the human skull bone on the displacement profiles, hydrophone measurements were performed on twelve human skulls. The skulls were extracted from 12 fresh human cadavers at the “Institut d’Anatomie UFR Biomédicale des Saints-Pères Université René Descartes”, Paris and were lent to the authors for the duration of the study. All the specimens fulfilled the “Centre du Don des Corps” criteria and had given their informed consent before death. The 512 element therapeutic probe was used in a water tank and a hydrophone (HNC-0400, Onda Corporation) was placed at its geometrical focus with stepped motors. The skulls had been used in previous study on the evaluation of the precision of the treatment for targeting the thalamic nucleus ventro-intermedius (VIM) implicated in essential tremor(Chauvet et al. 2013). The geometrical focus was set to the same location it is intended to be in the first clinical target envisioned with the prototype used in this study: the VIM. Skulls were mounted on a stereotactic frame and placed between the probe and the hydrophone. The hydrophone was then scanned (FOV size: 6×6×12 mm3, resolution 0.375×0.375×2 mm3) to record the intensity field in the presence of the skull. Intensities were measured with and without skull aberration correction. Skull aberration correction was achieved by hydrophone-based time reversal:

i. a ten cycle 1MHz signal was first emitted by the hydrophone
ii. after propagation through the skull bone, the distorted wave front was recorded on the therapeutic array; the wave front was then time reversed in order to compensate for the diffraction and refraction effects induced by the skull bone: each transducer was driven by an independent electronic channel capable of generating the temporally inverted signal stored in memory
iii. time reversed signals where re-emitted in order to focus back through the skull towards the initial position

The corresponding intensity profiles were calculated and fitted with a Gaussian function.

3.4 Keyhole

Keyhole is a data-sharing method (Van Vaals et al. 1993)(Jones et al. 1993). A reference image with a complete PE range Δk_y is recorded once. Then, only a central subset of k-space data lines δk_y, i.e., the keyhole range, is collected from the image. The subset δk_y is then merged with the peripheral lines of the k-space of the reference image and then Fourier transformed to generate updated images Figure 3.3.

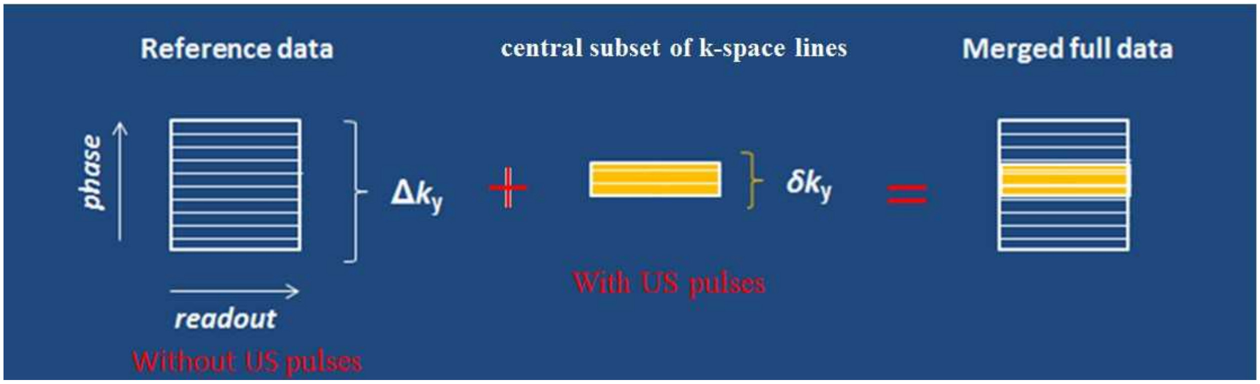

Figure 3.3: Principle of Keyhole technique

The gain in temporal resolution, the so-called keyhole factor, is defined as:

$$\mathrm{R} = \frac{\Delta k_y}{\delta k_y}$$

Consider a one-dimensional profile *f*(*y*) in the PE dimension which characterizes the change to update. We denote the Fourier Transform (FT) by F(k_y). Without contrast enhancement, the keyhole range is simply the product of F(k_y) by a window function WF(k_y), which is equal to 1 (0) inside (outside) the keyhole. As a result of the convolution theorem, the profile *f*(*y*) is convolved by a point-spread function (PSF) p(y), which is the FT of WF(k_y), i.e. a sinc function. The keyhole degrades the resolution of the change image in the PE dimension (Hu 1994) and the minimum number of lines to be acquired is ultimately determined by the size of the dynamic object (Spraggins 1994). Keyhole performed with a high keyhole factor R factor may result in an image intensity drop for small objects (Spraggins 1994).

3.5 Keyhole and MR ARFI: simulations

Numerical simulations were performed to determine the effect of the keyhole method on phase images containing a two-dimensional Gaussian profile f(x, y). In the following, the x and y axes denote the readout and PE (keyhole) axis respectively. The Gaussian profile was characterized by spreads $\{\sigma_x, \sigma_y\}$ and was centered at a given position $\{x_0, y_0\}$. Simulated data were generated in two ways.

First, the impact of the keyhole sampling on a dynamic Gaussian object of amplitude A_0 was studied. Magnitude images of the Gaussian profile were produced for $\{\sigma_x, \sigma_y\} = \{1, 1\}$ or $\{1, 4\}$ pixels, $A_0 = 1$ (a.u.), $\{x_0, y_0\} = \{49, 49\}$ and with $N_x \times N_y = 96 \times 96$ points. Simulated keyhole (magnitude) images were generated for every even keyhole range δk_y, i.e., by replacing pairs of lines, one on each edge of k-space with zeroes, and this repeatedly until $\delta k_y = 0$.

Secondly, the two-dimensional Gaussian profile was encoded into the background phase of an experimental image, as would occur in a realistic MR ARFI experiment. A spherical phantom filled with doped water (17 cm diameter, Siemens Healthcare, Erlangen, Germany) was used to generate a background image. A spin-echo sequence was implemented with a FOV of 192×192 mm using an isotropic resolution of 2 mm (matrix size = 96×96). The slice was approximately positioned at the center of the sphere, resulting in a ~17 cm in-plane disc image. In order to remove background phase variations, two acquisitions were performed and only the phase difference image, combined with one of the two magnitude images, was considered in the simulations. As in the previous case, the Gaussian profile was arbitrarily positioned and inserted with spreads $\{\sigma_x, \sigma_y\} = \{1, 1\}$ or $\{1, 4\}$ pixels. For the sake of clarity, we have denoted by φ_0 (in radians) the amplitude of the Gaussian profile encoded into the phase. This second category of simulations was achieved with $\varphi_0 = 1$ rad. The keyhole acquisitions were simulated by replacing the outer k-space lines of the synthetic phase images by the corresponding lines taken from the initial experimental set of raw data. Again, this was achieved for every even keyhole range δk_y.

3.6 Ex-vivo experiments

Images were acquired on a 3T Siemens Verio MR scanner (Siemens, Erlangen, Germany). The measurements were performed in an ex-vivo calf brain immersed in a 3% agar gel. Flexible phased array receiving coils were wrapped around the object. Inversion recovery experiments were previously conducted to extract longitudinal relaxation times T1. These ranged between 0.7 s and 1 s. A spin-echo sequence (Figure 3.1) was modified to sample a specific keyhole range δk_y, such as δk_y /Δk_y = 1/R = 8/8 (R = 1), 7/8, 6/8, 5/8, 4/8 (R = 2), 3/8, 2/8 (R = 4) and 1/8 (R = 8). Experimental parameters were: TE = 43 ms, TR = 900 ms (≈ T1), bandwidth = 390 Hz/pixel, the number of excitations N_{ex} was 1. Each acquisition was preceded by 3 dummy scans. Square fields of view (FOV) of 160×160 mm2 were acquired with a matrix size of 64×64, isotropic resolution of 2.5 mm (V_{voxel} = 15.6 mm3). With R = 1, TA ≈ 61 s. Two reference datasets without ultrasound pulses were recorded with a complete PE rangeΔk_y. In addition, one dataset for each permitted keyhole range range δk_y (i.e., Δk_y, 7× Δk_y/8, 6× Δk_y/8… Δk_y/8) was acquired with ultrasound pulses. Each keyhole data was merged with complementary peripheral lines taken from the first reference dataset. Background phase variations were removed by subtracting the updated image and the second reference image. Note that a use of the same reference dataset for data-sharing and the subtraction of background phase variations would result in a low resolution version of the background phase image in the PE dimension. The experiments were performed for three imaging configurations: one transverse (TRA) view and two sagittal (SAG) views with the PE axis being either perpendicular (per) or parallel (par) to the longest axis of the ultrasonic focal spot as illustrated in Figure 3.4. The displacement encoding gradients were applied along the slice, readout, and PE axis when using the TRA, SAG (per) and SAG (par) configurations respectively. Regional saturation bands were necessary to avoid folding along the PE direction due to the water flowing in the coupling system located between the ultrasound transducer array and the ex-vivo tissue. Image processing was performed off-line using Matlab (Mathworks, Natick, MA).

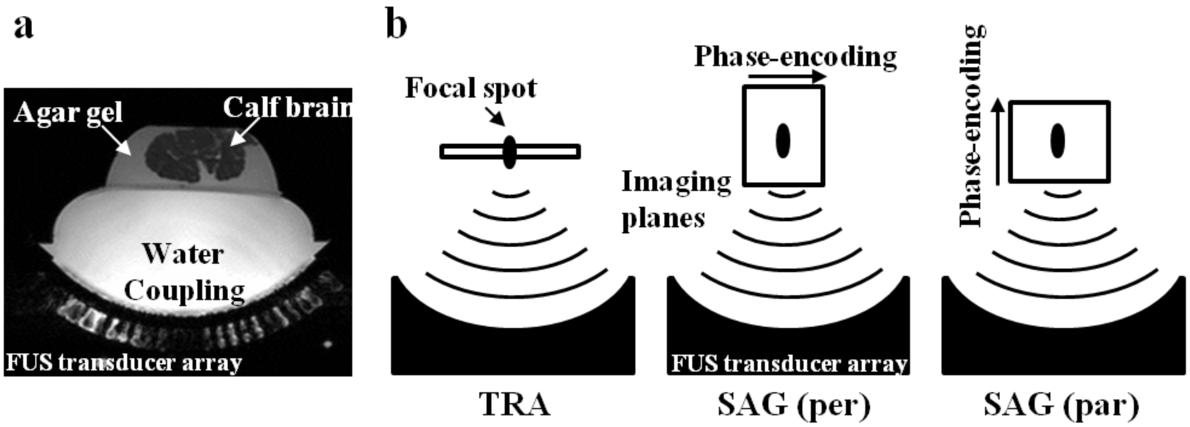

Figure 3.4 (a, b): a- Sagittal view of the MRgFUS experimental setup. b- Imaging configurations tested in this work for MR ARFI keyhole acquisitions.

3.7 Results

3.7.1 Simulated data

Figure 3.5a presents simulated keyhole magnitude images of a two-dimensional Gaussian object of various spreads and of amplitude $A_0 = 1$. Figure 3.5b displays the cross-sections taken along the y axis that pass through the position of the maximum for R = 1, 4 and 8. When R increases, the Gaussian shape is gradually convolved by a sinc function in the PE dimension. The convolution results in a loss of resolution. As shown in Figure 3.5c, the keyhole method also leads unavoidably to a decrease of the amplitude A_0; however the rate at which it occurs is lower when the spread σ_y increases. To explain these features, consider again a 1D Gaussian profile $f(y)$ in the y (PE or keyhole) dimension. It is known that a broad Gaussian profile $f(y)$ in the image space generates a sharper Gaussian $F(k_y)$ in the magnitude of the k-space and vice-versa. Indeed, the full width at half maximum (FWHM) of $f(y)$ is directly proportional to σ_y (FWHM ~ 2.35× σ_y), while the FWHM of $F(k_y)$ is inversely proportional to σ_y and depends on the number (denoted N) of complex data points involved in the discrete FT (FWHM ~ 0.37/N× σ_y). Truncation of high frequencies would thus be more severe for a sharp Gaussian object, resulting in earlier convolution process and decrease of amplitude when R is increased.

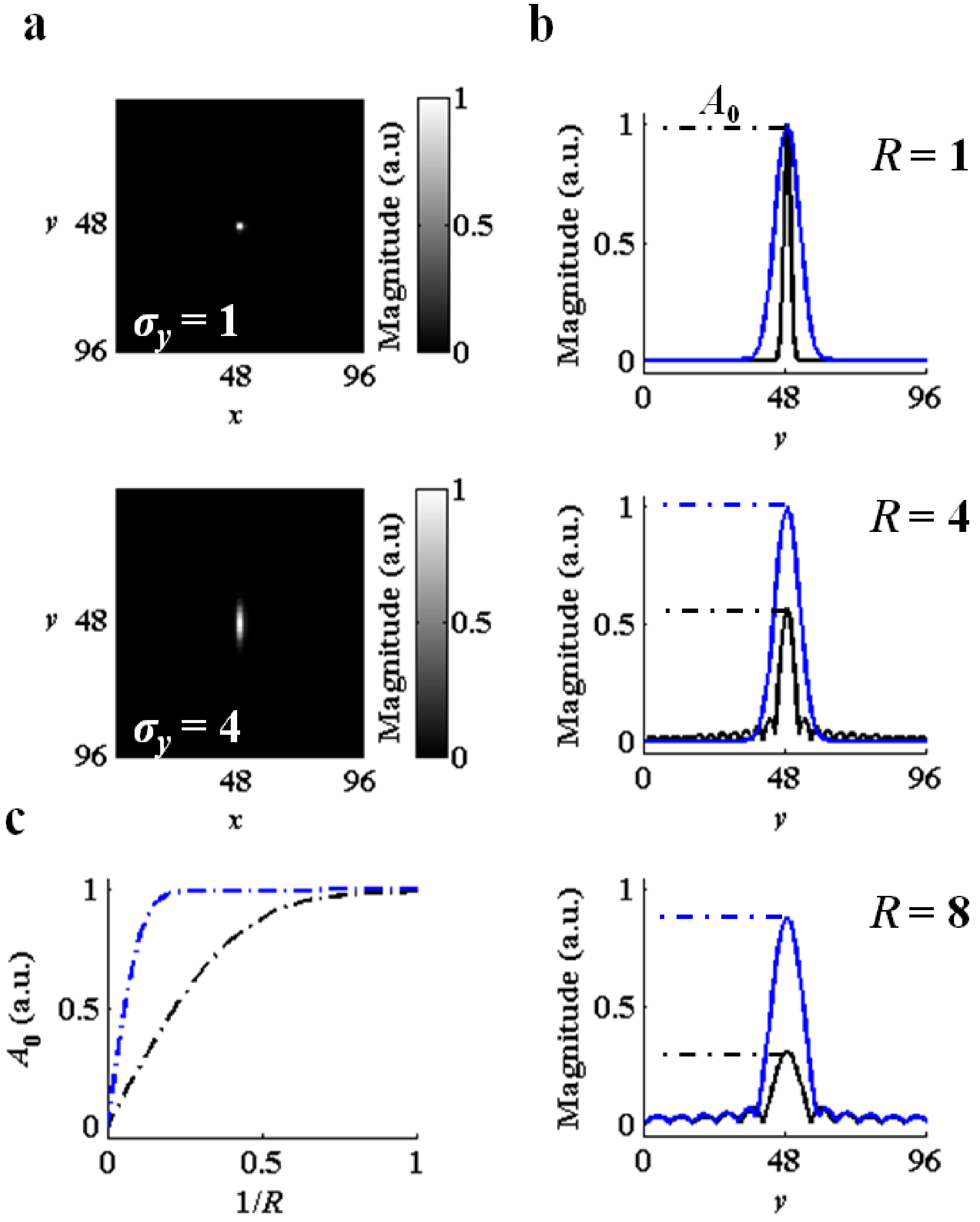

Figure 3.5 (a, b, c): a- Magnitude images of a Gaussian profile $f(x, y)$ centered on $\{x_0, y_0\} = \{49, 49\}$ with an amplitude $A_0 = 1$ and spreads $\{\sigma_x, \sigma_y\} = \{1, 1\}$ or $\{\sigma_x, \sigma_y\} = \{1, 4\}$ pixels. b- 1D profiles obtained with $\sigma_y = 1$ pixel (*black line*) or $\sigma_y = 4$ pixels (*blue line*) taken from the *y* axis for various keyhole factors. c- Plot of the amplitude A_0 versus the inverse of the keyhole factor *R*. The size of the dynamic object is a crucial parameter for the keyhole technique.

Figure 3.6a shows synthetic keyhole phase images made with a two-dimensional Gaussian profile encoded into the phase of an experimental image. **Figure 3.6**b and

Figure 3.6c displays the 1D Gaussian profiles passing through the maximum phase in the two imaging dimensions. Results are shown for spreads σ_x = 1 pixel, σ_y = 1 and 4 pixels. As R increases, the profile in the x dimension remains intact, while the resolution is gradually lost in the y dimension. The convolution process and the decrease of maximum phase are again attenuated when σ_y is increased. With φ_0 = 1 rad, the PSF that convolves the Gaussian profile seems to be similar to a sinc function. Experimentally, it is expected that the maximum phase will rarely exceed one or two radians.

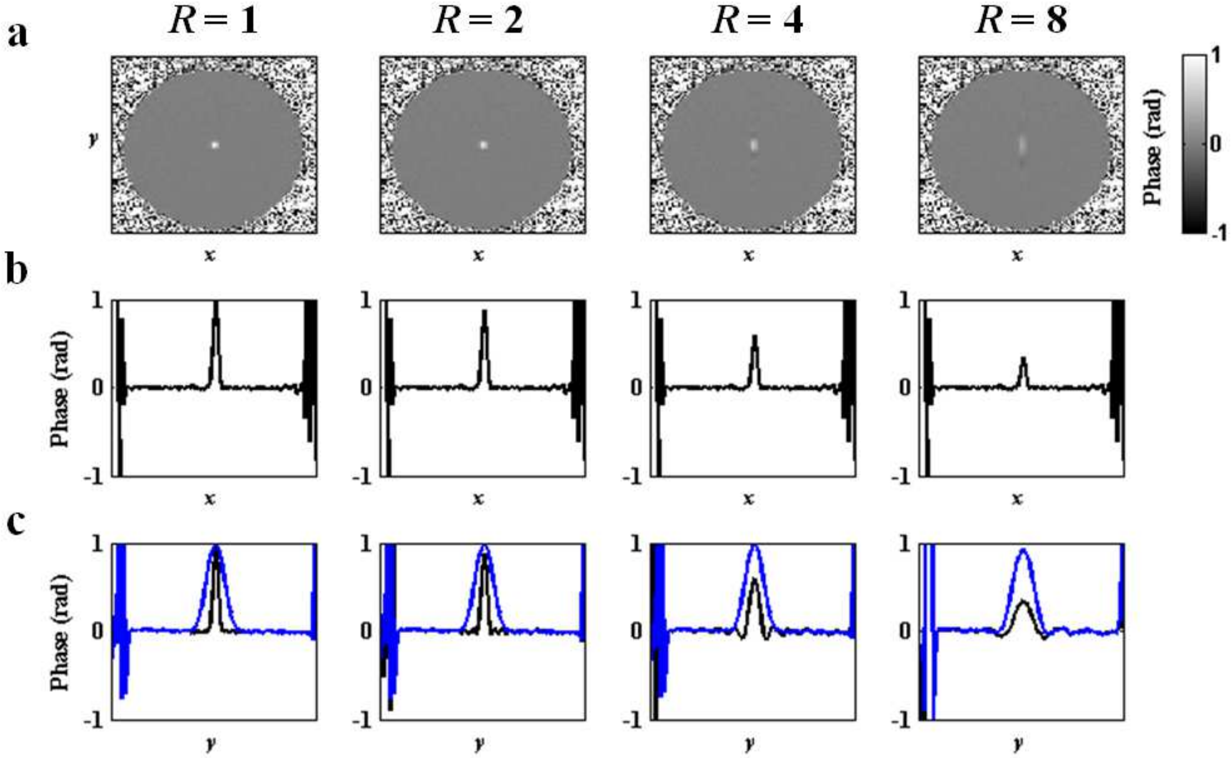

Figure 3.6 (a, b, c): a- Synthetic phase images containing a two-dimensional Gaussian profile *f*(*x*, *y*) obtained with *R* = 1, 2, 4 and 8. The profile was introduced with an isotropic spread $\sigma_x = \sigma_y$ = 1 pixel and a phase amplitude φ_0 = 1 rad and was centred arbitrarily at $\{x_0, y_0\}$ = {49, 49}. b- 1D maximum phase profiles taken from Fig. 4a. and along the *x* axis. c- Idem along the *y* (*keyhole*) axis with σ_y = 1 pixel (*black line*), σ_y = 4 pixels (*blue line*).

Figure 3.7 plots the evolution of φ_0 versus the inverse of the keyhole factor for spreads σ_y = 1 and 4 pixels. The evolution is almost coincident with the curves obtained for A_0 in our preceding simulations (Figure 3.5). Changes in the position of φ_0 as well as the size of the object in the background image had no influence on the keyhole features simulated here (data not shown). As a result, the evolution of the displacement profile using the keyhole method can be simulated from a simple 1D Gaussian object. The a priori knowledge of the spread of the displacement profile in the PE dimension is then sufficient to predict the decaying rate of the intensity at the target.

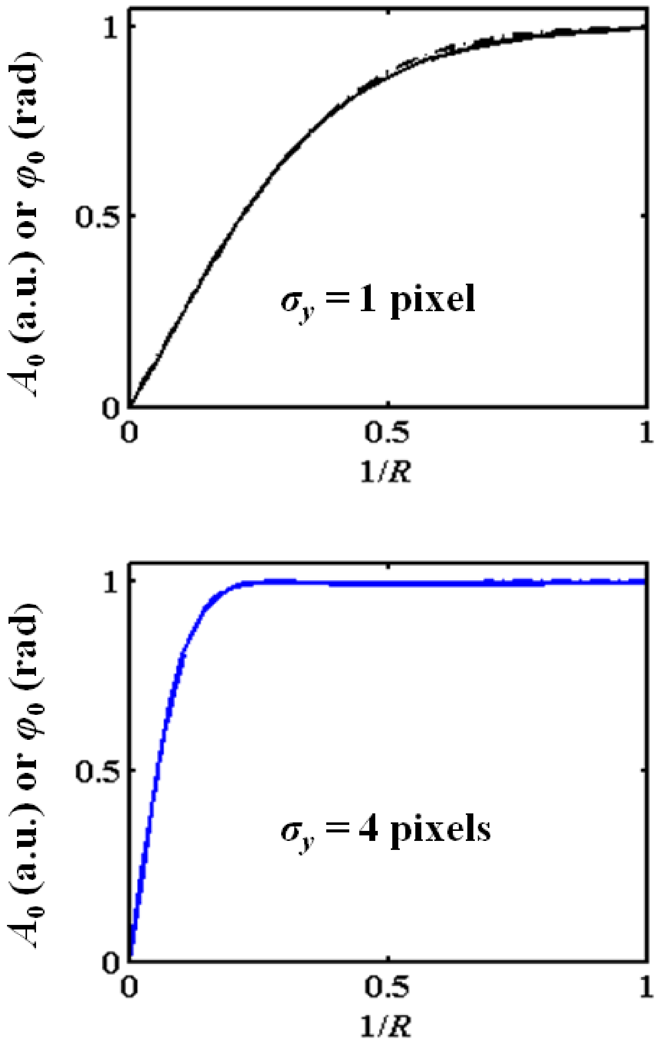

Figure 3.7: Plots of A_0 (*dashed line*) and φ_0 (*continuous line*) versus the inverse of the keyhole factor *R* using $A_0 = 1$ and $\varphi_0 = 1$ rad.

3.7.2 Experimental MR ARFI data

Experimental MR ARFI images obtained in an ex-vivo calf brain using four different keyhole factors are shown in Figure 3.8. The acquisitions were performed for a transverse (TRA) view and two sagittal (SAG) views with the displacement being oriented perpendicular (per) or parallel (par) to the PE direction. From keyhole factors R = 1 to 8, the phase amplitude at the focal spot decreases and the resolution is gradually lost.

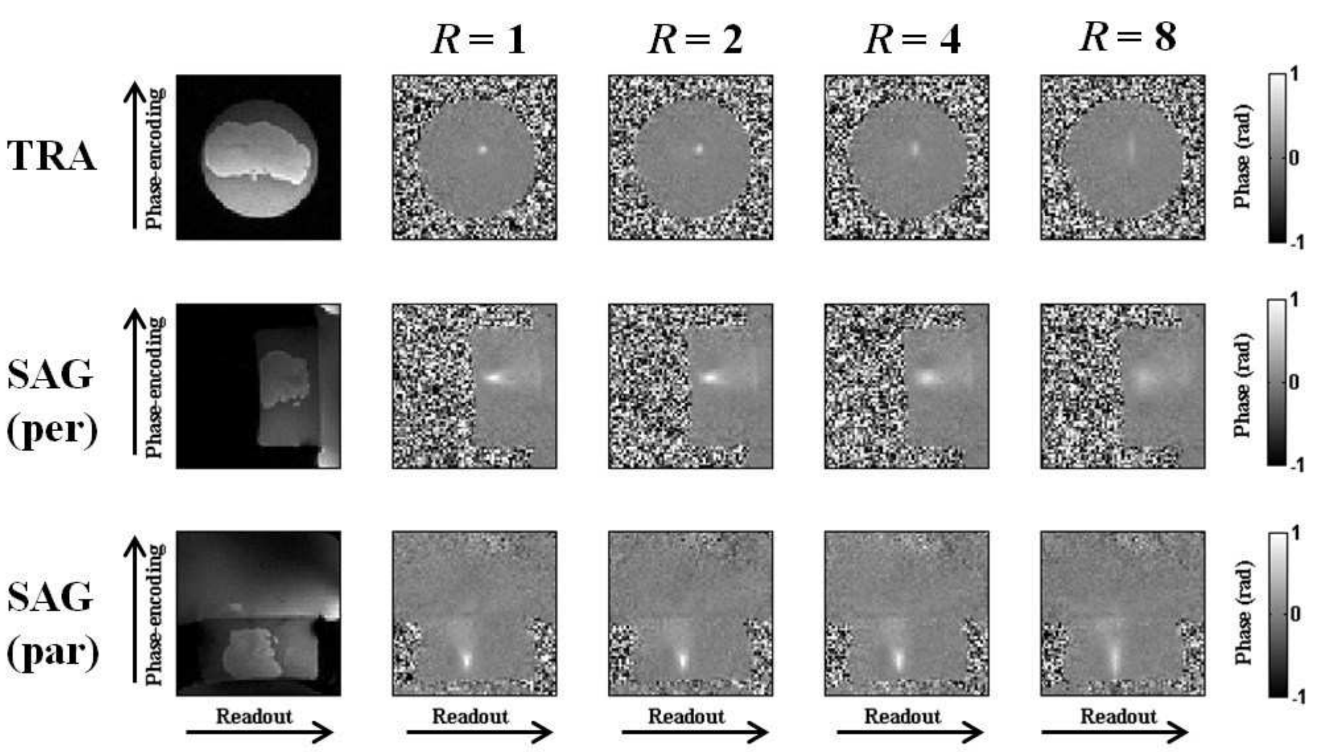

Figure 3.8: Ex-vivo calf brain phase images obtained with MR ARFI using keyhole factors *R* = 1, 2, 4 and 8 for a transversal view (TRA), and sagittal views (SAG) with the longest axis of the focal spot oriented perpendicular (per) or parallel (par) to the phase-encoding direction.

Figure 3.9a shows non-linear least square fits using a Gaussian function of the phase profile of the focal spot taken along the PE axis when R = 1. The spread and maximum phase values are σ_y ~ 1 pixel (FWHM ~2.35 pixels) and φ_0 = 0.83 rad for the

TRA view, σ_y ~ 1.2 pixels (FWHM ~3 pixels) and φ_0 = 0.87 rad for the SAG (per) view, and σ_y ~ 2.6 pixels (FWHM ~6.1 pixels) and φ_0 = 0.94 rad for the SAG (par) view. **Figure 3.9**b shows the plots of the phase φ_0 measured at the target for 1/R = 1/8 to 1, in steps of 1/8. For the TRA and SAG (per) view, φ_0 continuously decreases with R. For R = 2, φ_0 keeps more than 90 % of the original value and then falls to 60-70% at R = 4 or to 35-40 % at R = 8. For the SAG (par), φ_0 remains almost intact from R = 1 to 4 (~95 %), and then decreases to ~70 % at R = 8. The configuration SAG (per) gives roughly two times more signal than TRA when R = 8. According to our simulations, it is sufficient to apply the keyhole technique to a Gaussian object encoded into the magnitude to reproduce properly the evolution of the phase values as a function of the keyhole factor. With spreads extracted from the fits displayed in **Figure 3.9**a and φ_0 values measured in phase images displayed in **Figure 3.8**, the simulated curves are in good accordance with the experimental data (**Figure 3.9**b).

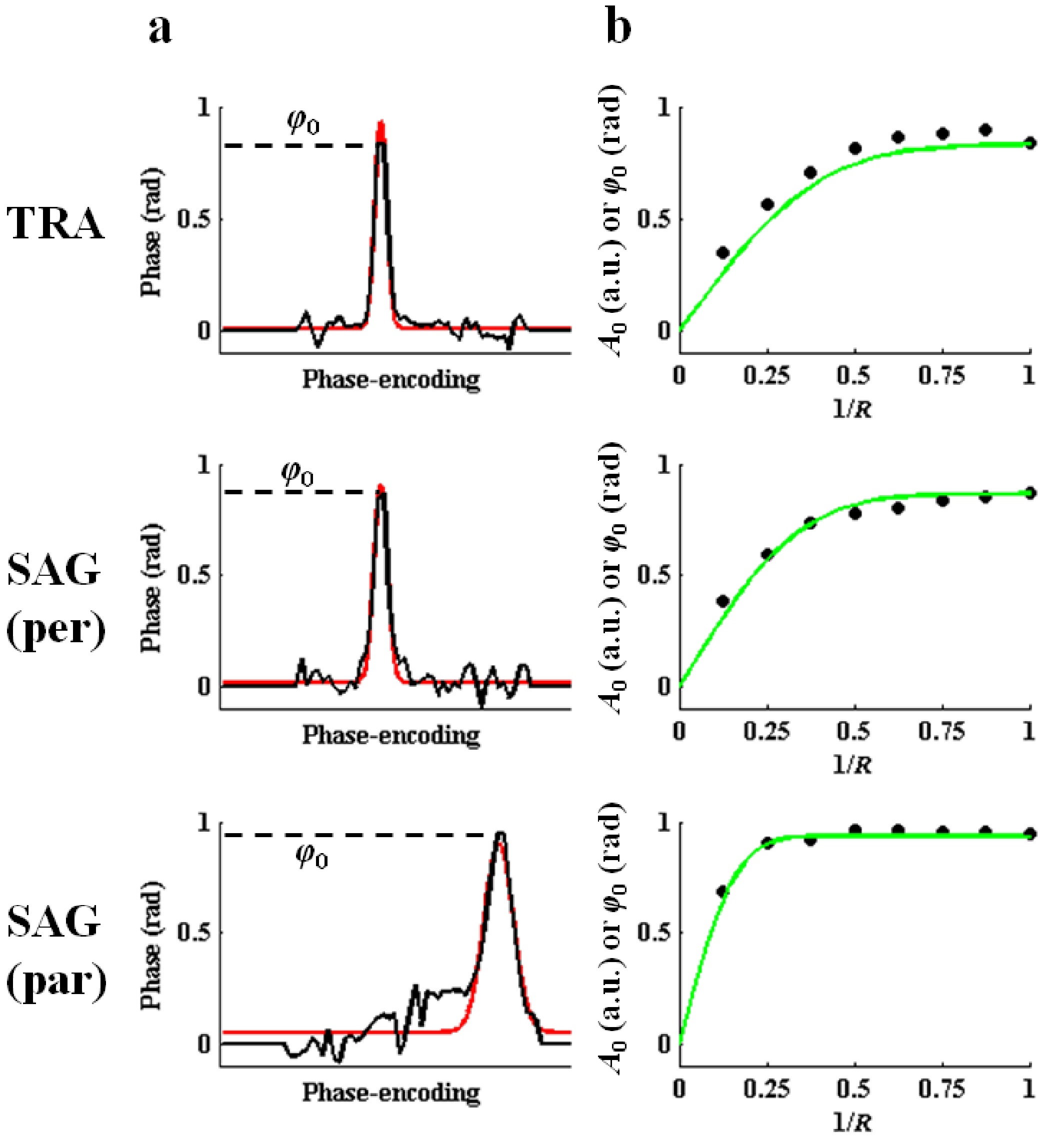

Figure 3.9(a, b): a- (black) 1D phase profiles of the focal spot in the phase-encoding dimension taken from Figure 3.8. (red) Non-linear least square fit using a Gaussian function. b- (black dots) Maximum phase φ_0 measured at the target versus the inverse of the keyhole factor. (green) Simulated evolution of the amplitude A_0 of a Gaussian object based only on the spread extracted from the fit. The φ_0 values were only used as scaling factors. For the SAG (par) configuration, note that the small discrepancy between the experimental phase profile and the Gaussian-fit is due to the phase differences in the background between the phantom and the water coupling system.

3.7.3 Experimental evaluation of the influence of the skull on the intensity profile

Table one list coefficient of determination R^2 of Gaussian fits along each axis for all transcranial sonications, with and without aberration correction. Time reversed focusing corresponds to higher values of R^2. Nevertheless, the lowest mean R^2 without correction is equal to 0.968.

	Without correction	**Time Reversal correction**
R^2 along x axis	**0.968 +/-0.0431**	**0.999 +/-0.000394**
R^2 along y axis	**0.986 +/-0.0225**	**0.997 +/-0.00315**
R^2 along z axis	**0.991 +/-0.0122**	**0.999 +/-0.000414**

Figure 3.10 shows examples of experimental intensity profiles (blue) and corresponding Gaussian fits (red). Skull #5 and skull #8 illustrate typical plots obtained with all skulls. For sake of conciseness only non-corrected profiles are displayed for these two skulls (Figure 3.10a and b). The worst case scenario has also been displayed (skull #12) with time-reversal-based aberration correction (Figure 3.10d) and without (Figure 3.10c).

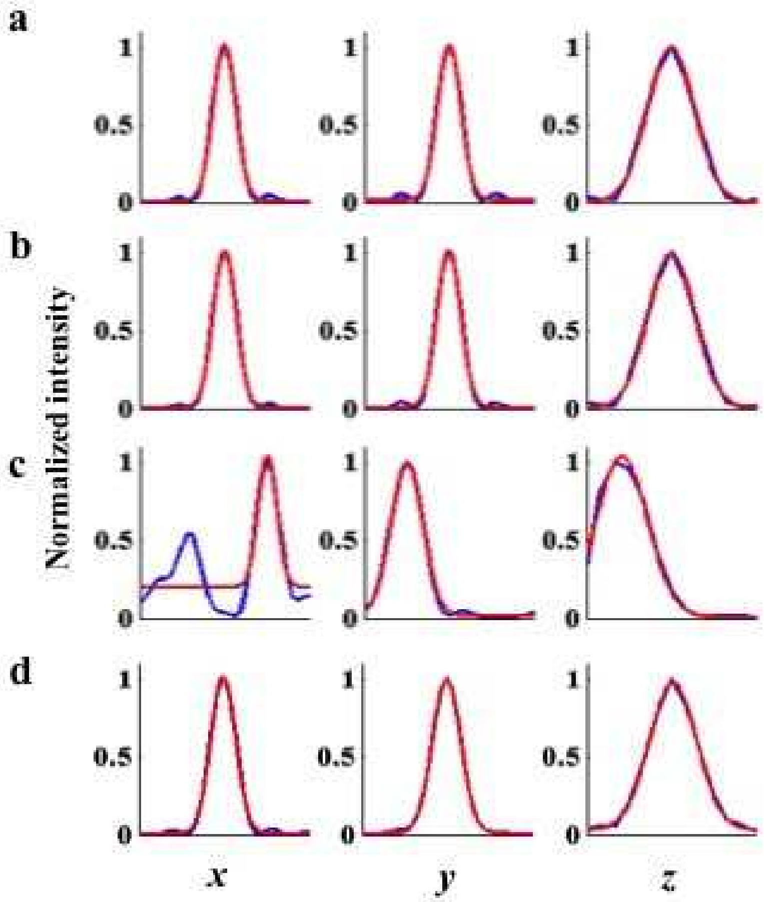

Figure 3.10(a, b, c, d): Normalized intensity profiles along each axis obtained at focus when sonicating through typical skulls (skull #5 and skull #8) and the worst case focusing (skull #12): a- skull #5 without any correction, b- skull #8 without any correction, c- skull #12 without any correction, d- skull #12 with time reversal correction. Experimental data (blue lines) are compared to Gaussian fits (red lines)

3.8 Discussion

Compared to the most popular applications of the keyhole technique, our approach benefits from the a-priori knowledge of the dynamic object since it is known that the displacement profile can be described by a Gaussian shape constrained by the geometrical characteristics of the ultrasonic transducer and the ultrasonic sonication parameters. Water tank measurements showed that even if the skull affects the propagation of ultrasound, the Gaussian functions can fit the beam profile along the three main axis with a high R^2 coefficient (more than 0.968), at least for targeting the centrally located VIM(Chauvet et al. 2013). A Gaussian function has straightforward Fourier transform properties that deserve to be exploited in the context of keyhole imaging. Typically, a broad Gaussian in the image space generates a sharp Gaussian in the reciprocal space and vice-versa. The PSF that characterizes the magnitude image of a Gaussian object obtained with keyhole is a sinc function. We have shown via numerical simulations that a keyhole acquisition results in a degradation of the resolution in the phase-encoding dimension and in a drop of the maximum amplitude when the keyhole factor R is increased. In addition, our simulated data indicate that the spread of the Gaussian determines in-fine the rate at which its amplitude decays. In particular, a broad Gaussian in the image space minimizes the deleterious impact of the keyhole technique.

MR ARFI encodes the Gaussian displacement profile into the phase of the image (McDannold and Maier 2008) not into its magnitude counterpart. To our knowledge, there exists no analytical expression for the corresponding PSF. The impact of the keyhole method on a Gaussian phase profile has thus been investigated here with numerical simulations based on experimental MR images. The simulations were made with φ_0 = 1 rad. It is indeed expected that the maximum phase, i.e. the displacement, that can be measured in a real (through skull or ribs) in-vivo experiment would never exceed this threshold. Under this condition, it has been observed that the PSF was very similar to a sinc function. Accordingly, the decrease of the phase at the target was almost coincident with the decay of the amplitude of a Gaussian magnitude profile. Though less realistic, future work could determine wether this similarity holds when the phase at the target is increased by several fold.

The experiments were performed in an ex-vivo calf brain. We have demonstrated that the keyhole technique can dramatically enhance the acquisition speed of a 2D spin-echo MR ARFI sequence. The unwanted effects of keyhole are mitigated when the phase-encoding axis of the imaging plane is parallel to the longest axis of the focal spot. This agrees with our simulations and our theoretical description. Using this particular imaging configuration, SAG (par), the 1D profile of the focal spot taken along the phase-encoding axis is the broadest. It is then possible to maintain seventy percent of the initial phase amplitude when a keyhole factor R = 8 is employed. In brief, this configuration makes best use of the keyhole technique for MR ARFI and would enable a reduction by a factor eight of the time required for adaptive focusing procedures. To guarantee no major changes of the phase information at the target, the keyhole method could be employed at least with R = 2 (TRA configuration) or R = 4 (SAG (par) configuration). If the time required the 3N MR ARFI images was one hour, the keyhole acceleration would decrease this duration respectively to 30 for R=2 or 15 minutes for R=4.

To a certain extent, the phase decay is thus predictable when the keyhole method is implemented. Only the knowledge of the spread of the Gaussian profile in the phase-encoding dimension would be required to achieve the calculations. It can either be determined experimentally in a calibration measurement without keyhole acceleration or be determined given the ultrasonic characteristics of the transducer (active surface, focal distance, acoustic power, central frequency and duration of the sonication). In the context of adaptive focusing, a knowledge of the spread would be absolutely necessary to correct for the decrease of maximum phase corresponding to the keyhole factor employed and thus to retrieve the true acoustic beam intensity at the target. The main objection to the keyhole method for MR ARFI would reside in artifacts originating from patient motion. However, this risk is minimum for FUS brain treatments and during MR-guided adaptive focusing procedures since the patient’s head is immobilized.

3.9 Conclusion

The keyhole method applied to a 2D spin-echo MR ARFI pulse sequence is able to generate rapidly undistorted displacement maps and offers an alternative to echo-planar imaging sequence. The principal requirements for MR-guided adaptive focusing procedures are fulfilled since keyhole ensures a reduction of the total time of acquisition and minimal heat deposition. It is demonstrated that the method is strongly dependent on the size of the ultrasound focal spot, and thus on imaging configurations. Indeed, the coincidence between the phase-encoding axis and the longest axis of the focal spot preserves a significant amount of the phase information at the target, even when high acceleration keyhole factors are used. A natural extension of this technique could be to apply it to MR temperature monitoring during FUS therapy. The geometry of both the radiation pressure and the temperature elevation distribution are indeed constrained by the focal spot profile, so that one would again benefit from a priori knowledge of the dynamic object.

Chapitre 4 **Neuromodulation on rats**

4.1 Introduction

If temperature elevation and radiation force are important tools for transcranial MRgFUS either as monitoring or correction tools, it may also be useful to rely on more subtle effects of ultrasound which are specific to the neural tissue: ultrasonic neuromodulation. It can be interesting to use ultrasound as a non invasive neuromodulation tool either to validate the targeting of a specific structure, based on its functional response to the stimulation (such as a transient stop of tremor) or to directly induce a therapeutic effect due to the repetitive stimulation of a specific structure, such as is currently achieved with transcranial magnetic stimulation, but with a better spatial resolution.

Although it is not yet fully understood, ultrasonic neuromodulation is not a new effect and has a long history. In 1958, Fry(F. Fry, Ades, and Fry 1958) was able to demonstrate that the transmission of ultrasound waves to the lateral *geniculate nucleus* could suppress the induced response in the primary visual cortex in cats, as evidenced by standard electroencephalogram recordings (EEG). In 1976, Gavrilov and colleagues(Gavrilov LR, Gersuni GV, Ilyinsky OB, Sirotyuk MG, Tsirulnikov EM 1976) studied the effect of ultrasound in humans and demonstrated that it was a powerful tool for stimulating nerve structures and produced different thermal, tactile, and pain responses. Later, Tyler and colleagues(Tyler et al. 2008; T. Tufail et al. 2010), proved the ability of low frequency, low intensity ultrasound waves to induce motor stimulation without producing damage to the brain tissue. Yoo and colleagues(Yoo et al. 2011) obtained similar results in rabbits in 2010 and used a magnetic resonance imaging (MRI)-compatible transducer to visualize the activation of the motor cortex using functional MRI.

Ultrasound can be focused through the intact human skull using multi-element transducers and phase correction (Thomas and Fink 1996; Tanter, Thomas, and Fink

1998; Hynynen and Sun 1999), thus making it possible to translate these animal studies to humans.

Compared to current non-ultrasonic neurostimulation techniques such as transcranial direct current stimulation (tDCS)(Nitsche et al. 2008), implanted electrodes(Ressler and Mayberg 2007), Transcranial Magnetic Stimulation (TMS)(Hallett 2000) or optogenetics(Szobota et al. 2007; Zhang et al. 2007), transcranial ultrasonic neuromodulation offers a unique combination of high spatial resolution (a few millimeters), good time resolution (few hundreds of milliseconds), good access to deep brain structures and non-invasiveness. Transcranial ultrasound neuromodulation could thus open the door to unique high resolution and non-invasive neuromodulation applications. Recent results confirm this potential, as focused ultrasound was shown to be able to modulate the level of cortical neurotransmitters(Yang et al. 2012) and thus, may have diagnostic as well as therapeutic implications for DA/5-HT-mediated neurological and psychiatric disorders.

Important questions on the mechanisms behind ultrasound neuromodulation remain. On the physiological scale, different hypotheses have been proposed from the ultrasound-induced release of neurotransmitters inside the synaptic cleft(Borrelli, Bailey, and Dunn 1981) to the ultrasound-induced opening of mechano-sensitive channels on the membrane(Krasovitski et al. 2011) that would then trigger action potentials(Tyler et al. 2008). On a more macroscopic scale, it has not yet been demonstrated wether the effect is linked to thermal or mechanical interactions of the ultrasound beam with neuronal tissue, which is nonetheless critical to optimize efficacy and safety. One way to investigate these interactions is to vary ultrasound parameters such as pressure, burst length and frequency and to study the resulting stimulation strength. However the existence of an acoustic threshold lower bound for the effect has been questioned as, interestingly, Tufail et al. reported higher electromyography (EMG) responses when lower acoustic intensities were used(T. Tufail et al. 2010). In contrast, King et al.(King et al. 2013) reported an acoustic threshold below which no stimulation was observed for ultrasonic neuromodulation in rats.

In order to investigate the potential mechanisms involved further, the exact value of the *in situ* acoustic threshold in the brain needs to be determined, as must the spatial distribution of the beam (for correlation with brain structures), due to the presence of standing waves. While investigating ultrasonic blood brain barrier opening, O'Reilly et al.(O'Reilly, Huang, and Hynynen 2010) reported pressure modulation due to standing waves, as measured in a rat skull inside a water tank. We propose here to take advantage of numerical simulations to investigate the spatiotemporal pressure field using a full rat head model surrounded by air, in the same experimental conditions used for neuromodulation.

In this thesis, we first studied the motor response of 8 rats using a low frequency transducer (320 KHz) transcranially for different ultrasonic pressure levels. We investigated the different kinds of motor responses elicited and the existence of an acoustic pressure threshold for the response. Since the exact pressure in the head cavity cannot be measured *in vivo*, the corresponding acoustic field was then simulated numerically using a full rat head 3D computed tomography (CT) scan and finite-difference time-domain (FDTD) software with identical acoustic parameters. The simulated pressure peak and spatial distribution inside the head cavity were then compared to that which was simulated in water. The correction of the motor thresholds for *in situ* pressure and the acoustic field spatial distribution are then discussed.

4.2 Experimental setup

A custom holder was used to lift the body of the animal while allowing free motion of its tail, forelegs and hind legs in order to easily visualize motor excitations. A stereotactic frame (502603, WPI, Sarasota, FL,USA) was used to immobilize the head. A single element focused ultrasound transducer (H115, Sonic Concepts, Bothell, MA, USA) (central frequency 250 KHz, diameter 64 mm, FD# 1) was used. A coupling cone (C103, Sonic Concepts, Bothell, WA, USA) filled with degassed water was used in between the transducer and the animal head (**Figure 4.1**). The transducer was fixed on two linear motors (Micos sMc Pollux, Freiburg, Germany) that allow a translation inside the horizontal plane to position the transducer over the desired target area. Echographic gel (Aquasonic 100, Parker Laboratories Inc., Fairfield, NJ, USA) was applied between the head to ensure acoustic coupling. All experiments were recorded on video to allow further determination of the motor threshold. The motor response was then manually classified in three categories: no response, moderate or strong motor response. A strong motor response was considered when a clear limb movement was elicited. Moderate motor response was considered when a muscular contraction was clearly visible but no limb movement occurred. Visual motor response classification was preferred to electromyography recordings (EMG) because EMG measurements were found to be affected by electrical cross-talk with the transducer driving signals. Several electrodes and shielding have been tested but too many false responses were recorded, as demonstrated by additional measurements without coupling gel and thus without actual ultrasound transmission.

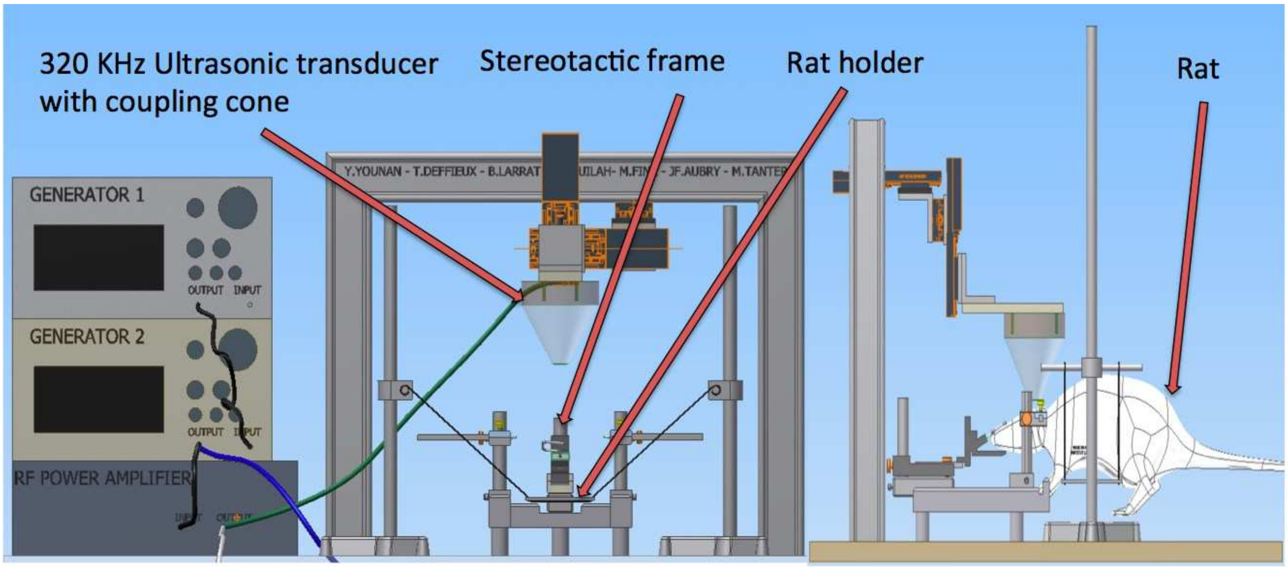

(a) (b)

Figure 4.1(a, b): a - Experimental setup showing the stereotactic frame, ultrasound transducer, linear motors and support frame with the electronics equipment, b - Schematic diagram with the animal positioned in the stereotactic frame and holder. The transducer with coupling cone is positioned on the head of the animal.

4.3 Ultrasound sequence and calibration

The ultrasound sequence used is based on the protocol of Tufail et al.(Y. Tufail et al. 2011), with a slightly higher center frequency of 320 kHz instead of 300 kHz; this corresponds to a peak in the transducer spectrum and a longer total sonication duration of 250 ms instead of 100ms, which was found to be more efficient.

The detailed parameters are as follows: ultrasound frequency was 320 KHz, number of cycles was 75 per pulse (pulse duration = 230 µs), pulse repetition frequency (PRF) was 2 KHz (duty-cycle=50%) and the total burst duration was 250 ms. Only the pressure was changed in this study to identify the threshold, and ranged from 0.4 MPa to 1 MPa peak pressure.

In order to build such sequence, two generators were used (AFG3101, Tektronix, Melrose, MA); a 75 Watt amplifier (75A250A, Amplifier Research, Souderton, PA) was then used to deliver the required power to the transducer and the input voltage of the transducer was monitored using an oscilloscope (TDS2022B, Tektronix, Melrose, MA) and voltage probe (P6139A, Tektronix, Melrose, MA).

The transducer was calibrated with a custom built heterodyne interferometer(Royer, Dubois, and Fink 1992) in degassed water. The heterodyne interferometer uses a laser beam to detect the small vibration of the ultrasound wave on a mylar membrane which is then converted to pressure.

The calibration was first performed in free water. It was also performed behind three excised rat skulls. The skulls were cut in half in the horizontal plane to allow the positioning of the mylar membrane just behind the top of the skulls. Transmission through the rat skulls was measured at three different locations for all skulls, as shown in **Figure 4.2**b: position A at +1, +1 mm from Lambda (N=3 skulls), position B at -1.5, -1.5 mm from Bregma (N=3 skulls) and position C at Bregma (N=1 skull).

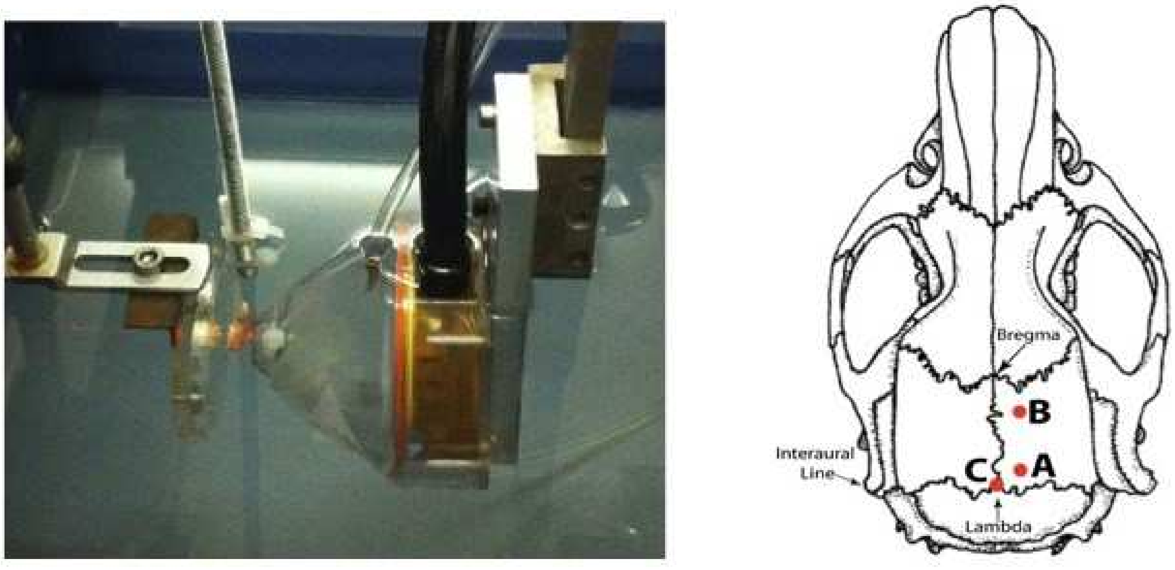

a

b

Figure 4.2(a, b): a- Image showing the position of the half-skull between the transducer and the heterodyne interferometer, b- the three different locations of attenuation measurement on the half-skull sample

4.4 Preliminary experiments

We spent a lot of time finding the appropriate dosage of sedatives (Ketamine/Xylazine). We varied dosage from 30 mg/Kg of Ketamine (respectively 8.45 mg/Kg of Xylazine) to 72 mg/Kg of Ketamine (respectively 20 mg/Kg of Xylazine) to sedate the rats. A total of 8 different dosages were tested three times : 24 experiments were thus conducted. The most stable and reproducible response after US stimulation was obtained with the following dosage: 66 mg/Kg of Ketamine and 13 mg/Kg of Xylazine.

We also investigated various PRF (ranging from 500Hz to 4kHz) and chose the value of 2 kHz as the most robust parameter.

This parametric exploration (n=14 animals) was used as a first step to find a good and reproducible response and design our final protocol but could in no way be interpreted as statistically relevant since the number of experiments conducted for each parameter was low (n=1-3 sessions max). However, it should be possible in future work to investigate those additional parameters with more animals in order to provide a more robust estimation of their influence.

4.5 Animal preparation and ultrasound neuromodulation protocol

All animals were Sprague Dawley rats (N=8; all male, body weight 150-250 g). Each rat was shaved prior to the experiment and was injected intraperitoneally with Ketamine and Xylazine for sedation (66 mg Ketamine for 1 kg body weight, 13 mg Xylazine for 1 kg body weight). Eight to ten minutes after anesthesia, and once the rat was deeply anesthetized, the animal was placed on the holder and his head was fixed in the stereotactic frame. A coupling gel was placed over the rat head and the ultrasonic transducer was positioned using the motors at the desired location (**Figure 4.3**).

25 to 30 minutes after injection, we started to apply ultrasound pulses every 10 seconds to the rat brain with a pressure of 0.75 MPa, as estimated from the calibration measured in free water, around the locations Lambda –1 mm, - 1 mm and -3 mm as can be seen in **Figure 4.2**. These chosen locations correspond to the best success rate in obtaining motor responses, even though they did not correspond to the motor cortex area. The position was adjusted during this phase to find the best motor responses, although it was generally stable when moved less than a few millimeters. When a stable response was obtained, the pressure was reduced until the response was barely noticeable.

For each series of measurements, 30 different pressure amplitudes centered around this value were defined randomly in order to investigate the motor responses versus pressure curves. New series were added until the rat started to wake up and to show motor activity uncorrelated with the ultrasound pulses. This temporal window of acceptable anesthesia level typically lasted around 10 to 15 minutes depending on the rat weight and anesthesia strength. Meanwhile, the anesthesia level was regularly estimated by assessing the pedal reflex of the rat, assuming that no reflex meant a deep anesthesia level and a reflex meant a lower anesthesia level. For each series, experimental points were fitted with a sigmoid curve using Matlab (MathWorks, Natick, MA, USA) in order to obtain a more accurate threshold value for the motor response.

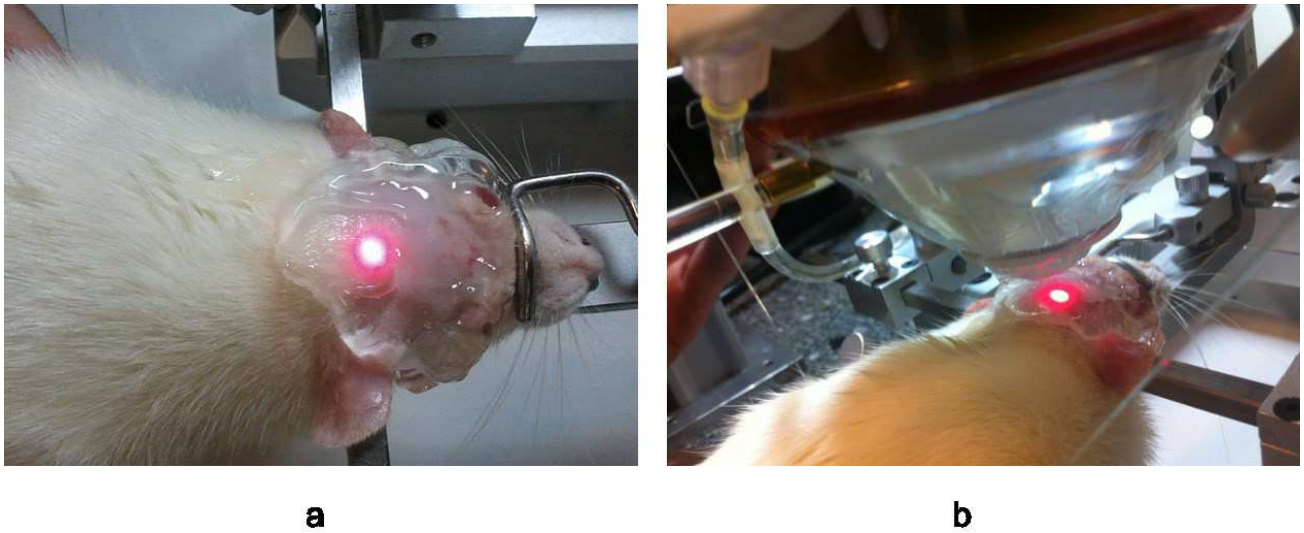

Figure 4.3(a,b): The ultrasound transducer is initially positioned close to the lambda anatomical point and has been marked by a laser beam here. The rat head is shaved and echographic gel was inserted between the coupling cone and the rat skin.

Possible damage was investigated by careful examination of the skin of the rats after the experiment and one day later. The behavior of the rats was also investigated over several days after each neuromodulation session and their weight controlled. No change in behavior or weight was observed, although no histology was performed in this study. In order to minimize the number of animals required for the study, each rat underwent several neuromodulation sessions with at least one week of recovery between each.

4.6 Numerical simulation of the experimental setup

In order to investigate the ultrasound field in the whole rat brain while taking into account complex effects of the full skull cavity and head geometry, three-dimensional (3D) numerical simulations of the ultrasound propagation were conducted. Acoustic density and velocity maps were reconstructed from a 80 µm micro-CT scan (Skyscan1178, Bruker micro-CT, source 65kV) of a rat head using an approach validated on different animal models(Aubry et al. 2003; Marquet et al. 2009; Deffieux and Konofagou 2010; Tanter et al. 2007). The skull was considered as a homogeneous layer since the only apparent variations were due to the smoothing from the CT reconstruction algorithm and not to the microstructure. The acoustic parameters are summarized in **Table 1**. The acoustic density and velocity 3D maps were then sub-sampled to a 240 µm isotropic resolution which gave a ratio of 20 pixels per wavelength.

An in-house 3D finite-difference time-domain acoustic simulation software (Acel, Institut Langevin, Paris, France), was used to perform the purely acoustic and linear ultrasound propagation simulation through skull structures(Aubry et al. 2003; Marquet et al. 2009; Tanter et al. 2007). The coupling cone and the tissue-air interfaces around the head were modeled as perfectly reflecting interfaces since the reflection coefficients between water and air and between tissue and air are close to 99.9% (Z_{air}=408 Pa.s/m, Z_{water}=Z_{tissue}=1.5 .10^6 Pa.s/m).

	Water	Brain	Skull	Other tissue (muscle, ears, skin ..)
Velocity(m/s)	1540	1560(International Commission on Radiation Units and Measurements 1998)	3000(Marquet et al. 2009)	1540(Marquet et al. 2009)
Density (kg/m^3)	1000	1040(International Commission on Radiation Units and Measurements 1998)	1850(Marquet et al. 2009)	1000(Marquet et al. 2009)
Attenuation (dB/cm)	0	0.6 @ 1 MHz(International Commission on Radiation Units and Measurements 1998) 0.19 @ 320 kHz	6.9 @ 1 MHz(Culjat et al. 2010) 2.2 @ 320 kHz	0.3 @ 1 MHz 0.1 @ 320 kHz

Table 1: Acoustic parameters used in the rat head model

Three simulations were performed: one in free water, one behind the half-skull immersed in water and one inside the full head cavity in air. The same acoustic parameters were used as in the experimental setup but the total simulation duration was limited to 500 µs of which 230 µs corresponded to a single ultrasonic pulse, as defined in the “ultrasound calibration and sequence” subsection (i.e. the full 75 periods of the 320 kHz ultrasound burst).

For each simulation, the pressure field was stored in three dimensions for all time steps in a 180 gigabyte file.

Time profiles of the acoustic pressure were extracted at the geometric focus for the three configurations and normalized to the spatial peak, time peak pressure simulated in free water. The spatial peak position in free water corresponds to the acoustic focus of the transducer which is slightly closer to the transducer than the geometric focus at low frequencies.

Maps of the *in situ* time peak pressure were also estimated by taking the time peak of the pressure field at each pixel for the sagittal, coronal and horizontal views, centered on the geometric focus. All maps were then normalized to the spatial peak, time peak pressure simulated in free water.

Spatial peak, time peak pressures (Psptp) were estimated for each configuration to discuss the effect of reverberations. These values were normalized to the Psptp simulated in water.

Spatial peak, time peak acoustic intensities (Isptp) were estimated for each configuration by squaring the Psptp with the same normalization.

Spatial peak, pulse averaged acoustic intensities (Isppa) were estimated for each configuration by first squaring the space-time pressure field then averaging over the 75 cycles (taking into account the propagation delay for each pixel) and finally taking the spatial maximum. Those values were normalized to the Isppa simulated in free water.

For the estimations of these normalized values, only the acoustic field inside the brain volume was taken into account, disregarding any other peaks outside of this volume.

In order to investigate the robustness of these results with respect to the transducer position, 10 different locations of the transducer were simulated. These locations were chosen randomly in a cube of length equal to the wavelength (i.e. 5 mm at 320 kHz) to generate different configurations of interference patterns between the transducer and the skull surface. This artificially increases the standard deviation of the estimated values but provides more insight on the influence of the transducer-skull interferences with respect to the intra head cavity reverberations.

4.7 Results

4.7.1 Ultrasound pressure calibration through the half skulls

Measurements of the ultrasound transmission through the rat half-skulls shows that, on average, for the three positions tested, 89% of the pressure amplitude can be recovered behind the half-skulls immersed in water (see **Table 2** and **Figure 4.2**). This is to be expected due to the low frequency used here (320 kHz) as skull thicknesses were estimated to be approximately 0.41 mm +/-0.16 mm using a digital caliper rule (Fischer Darex, Le Chambon Feugerolles, France).

In specific cases, transmission could be higher than 100%, which is due to constructive interference between the skull sample and the transducer surface and can also be observed in simulations with the half skull model.

Transmission	Position A	Position B	Position C	All measurements
320 KHz	91±8%	83±9%	75% (std N/A)	89±10%

Table 2: Transcranial transmission coefficient over the three different points on the skull surface. Positions tested are given in the Methods section.

4.7.2 Ultrasound neuromodulation experiments

Following the protocol described in the Material and Methods section, we obtained motor responses of the tail and hindlegs in more than 60% of the experimental sessions. In the case of failed experiments (40%), no stimulation at all could be observed for any of the trials performed on a given day for a given animal and for any acoustic pressure tested (up to 1 MPa). Successful experiments, however, were consistent and always repeatable during the same day. They were strong, and clearly visible to the naked eye.

In these cases, a reproducible response was observed above a pressure threshold. **Figure 4.4** illustrates such a motor response obtained in a rat with a strong tail movement triggered by the ultrasound pulse.

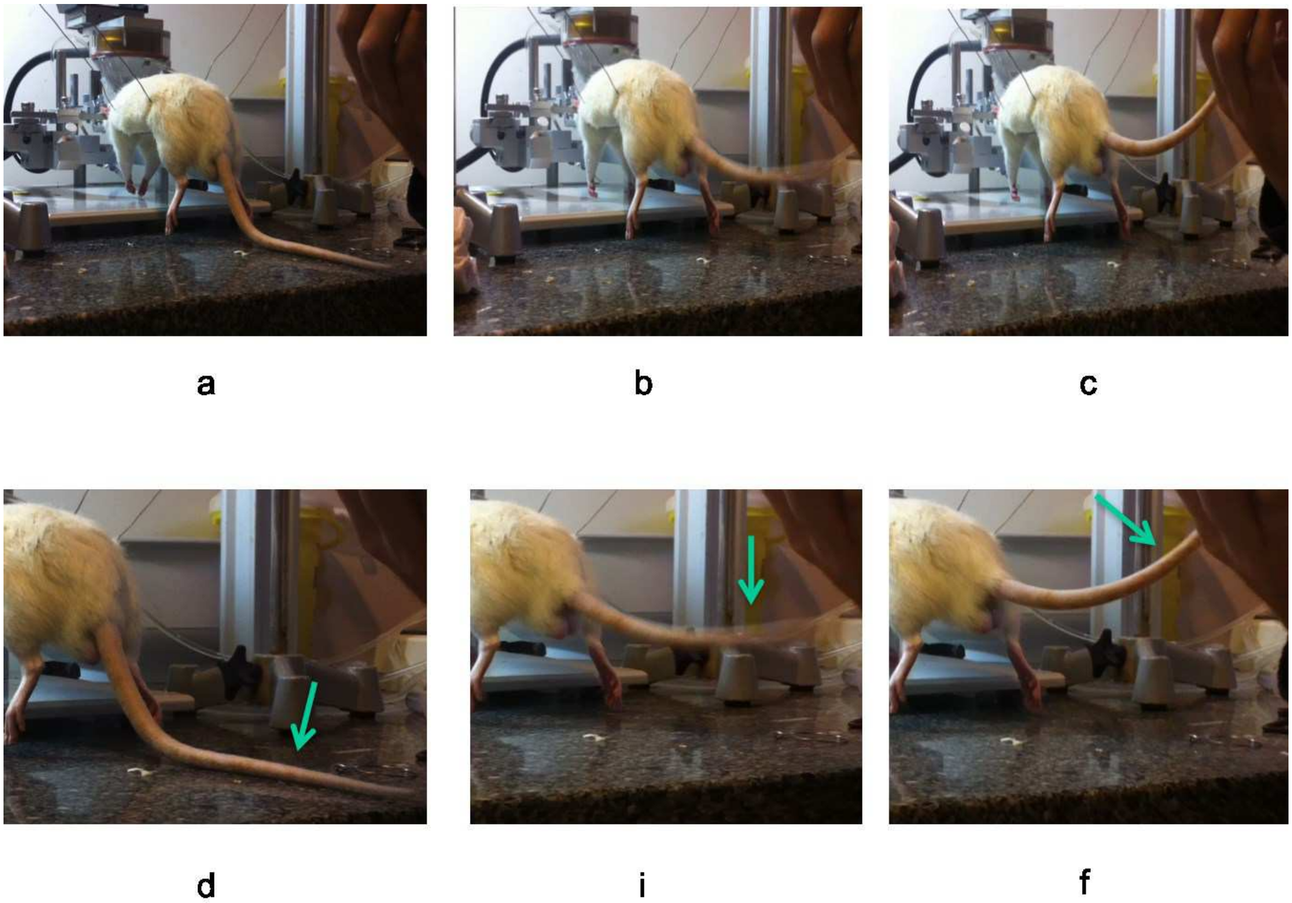

Figure 4.4 (a, b, c, d, i, f): Pictures of our successful experiments in our laboratory. We can see an immediate motor response in the tail. a- the moment before sending a sound wave. (d- close-up picture of the tail at the moment). b- during sending a sound wave. (e- close-up picture of the tail at the moment). c- through the end of the sound wave. (f- close-up picture of the tail at the moment.

While the observed motor responses largely involved the hindlegs and the tail, other motor responses have also been observed, such as contraction of the forelimbs or facial muscles, without tail or hindleg movement. These other motor responses did not seem to be linked to a particular position of the ultrasound transducer on the skull but were perfectly reproducible during the whole experimental session duration.

In some experimental sessions (N=3), we were also able to trigger a motor response of the occulomotor system alone (cf. Figure 4. 5) yielding a movement of the eyes. Both eyes were seen to move in the same direction. The focus zone was approximately 3 mm anterior, –2 mm right of the lambda point and the effects remained visible a few millimeters around this point.

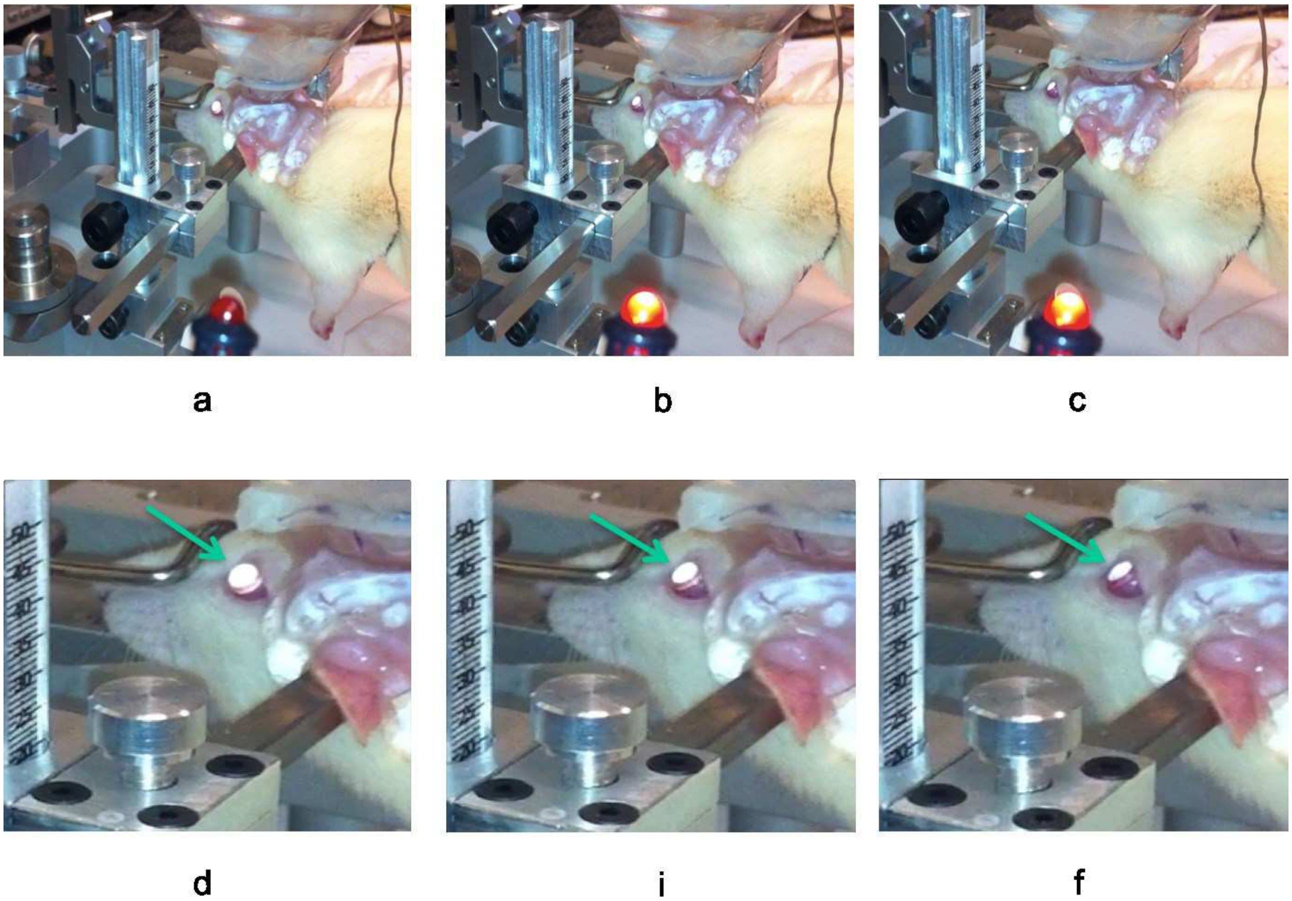

Figure 4. 5 (a, b, c, d, i, f): We can see an immediate motor response in the eyes. a- the moment before sending a sound wave. (d- close-up picture of the eyes at this moment). b- During sending a sound wave. (e- close-up picture of the eyes at this moment). c- through the end of the sound wave. (f- close-up picture of the eyes at this moment).

In another experimental session (N=1), we were able to trigger the motor response of a single whisker (cf. Figure 4. 6) during the whole duration of the experiment. Only the left whisker was seen to move. The focus point was contralateral to the whisker movement, 3 mm anterior, –1 mm right of the lambda point.

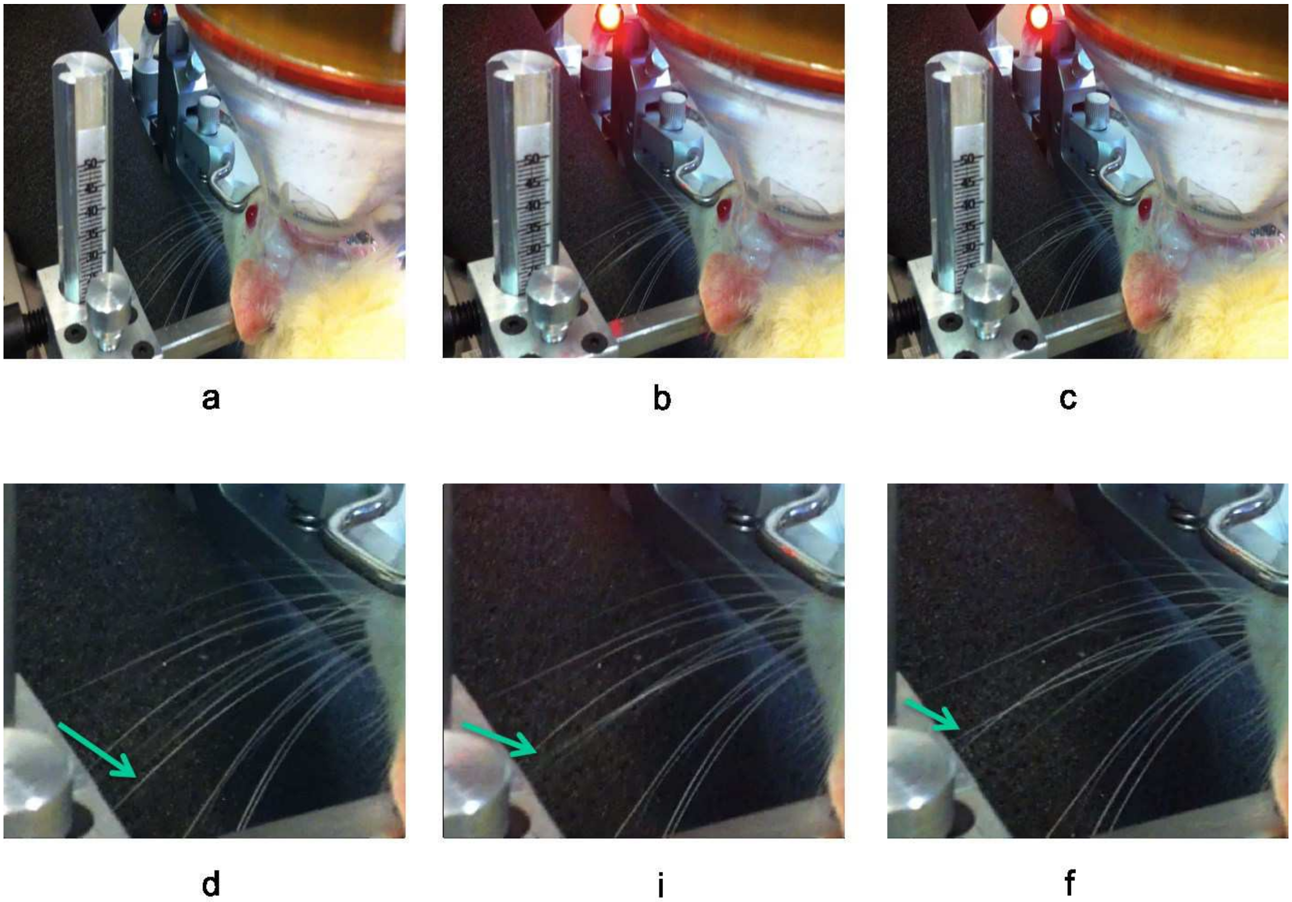

Figure 4. 6(a, b, c, d, i, f): We can see an immediate motor response in the mustache. a- the moment before sending a sound wave. (d- close-up picture of the mustache at this moment). b- During sending a sound wave. (e- close-up picture of the mustache at this moment). c- through the end of the sound wave. (f- close-up picture of the mustache at this moment).

The motor neuromodulation of very specific structures such as the occulomotor system or a single whisker are particularly interesting, since the size of the focal spot should theoretically not allow focusing only on such small brain regions (typically the occulomotor and lateral facial *nuclei* are submillimetric). One possibility is that their stimulation thresholds became lower in some of the experimental sessions due to specific brain activity state during the animal's sleep. Another possibility is that their activation involves the stimulations or inhibitions of several other structures that a given pressure pattern is able to trigger specifically. In order to get more insight into the spatial distribution of the ultrasound pressure field, results of numerical simulations of the ultrasound beam in a full rat head model are displayed in section 4.7.4 .

4.7.3 Pressure threshold

Figure 4.7 presents two response curves for the same animal, but at different times in the experiment, i.e. for different anesthesia stages: the motor response is plotted as a function of estimated pressure at focus, as evaluated in water, ranging from “no response”, “muscular contraction but no limb movement” to “muscular contraction with limb movement”. In those compiled results, rats of the same age and weight (200 g) were used with the same anesthesia protocol and we focused on the motor stimulation of the hindlegs and tail that were more consistently obtained.

Two experimental series are presented in **Figure 4.7** on the same animal for deep and light anesthesia stages. As described in the methods section, a sigmoid fit (red curve in **Figure 4.7**) was used to find the pressure thresholds, respectively 0.79 and 0.59 MPa in those cases. On average for all of the animals, we found a pressure threshold of 0.68 MPa (N=29 series), with a standard error of 0.02 MPa. Pressures are given as if in free water, without any correction applied. The standard deviation of the threshold corresponds to 0.1 MPa which is likely due to the anesthesia conditions and timing, as illustrated in **Figure 4.7**a and **Figure 4.7**b. Indeed, in the light anesthesia stage, the threshold was always found to be lower than in the early anesthesia stage (0.59 MPa in **Figure 4.7**b versus 0.79 MPa in **Figure 4.7**a), while the sigmoid also appears less sharp in **Figure 4.7**b, indicating more deviation in the responses for late anesthesia.

By using the results on which the pedal reflex was used as a classification tool between light and deep anesthesia (N=7 series), we found a threshold of 0.77 ± 0.04 MPa for early (deep) anesthesia (N=3 series, SE=0.02 MPa) and 0.61 ± 0.03 MPa for late (light) anesthesia (N=4 series, SE=0.015 MPa).

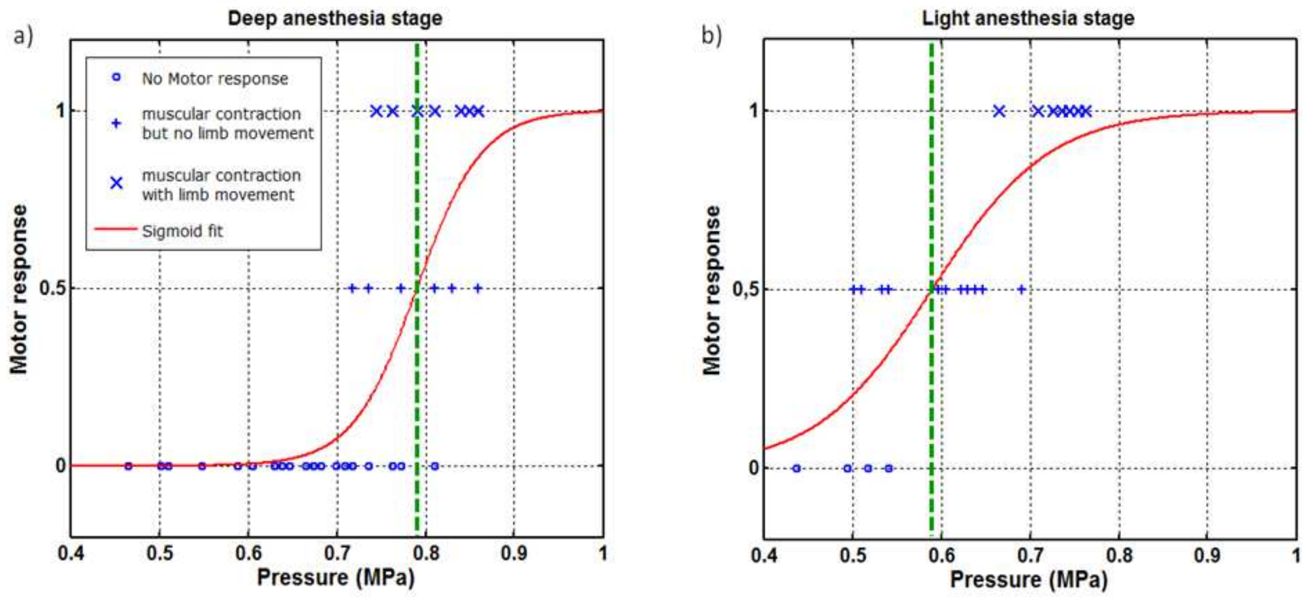

Figure 4.7 (a, b): Two response curves corresponding to different anesthesia stage on the same rat during the same experiment. a- In the beginning of the experiment, the sigmoid presents a sharp threshold at 0.79 MPa (uncorrected pressure). b- In the last minutes of the experiment, the sigmoid is not as sharp with a lower threshold around 0.59 MPa which corresponds to a diminishing threshold while the animal starts to wake up slowly.

All pressure thresholds are estimated in water for the equivalent input voltage, i.e. uncorrected for the skull transmission or any other effects. In order to provide values closer to the reality inside the brain, numerical simulations of the acoustic field in a full head model were performed and correction values for the pressure and intensity peaks are estimated in the next section.

4.7.4 Acoustic numerical simulation of the experiment

Numerical simulations of the acoustic field were performed using the geometry of the transducer and a CT scan of the rat head. All the ultrasonic parameters were similar to the real experiment.

Figure 4.8 presents the temporal pressure profile obtained at the geometric focus for the three configurations. In the case of the full head model, the pressure is not steady and oscillates over time due to acoustic interference in the head. It is also noticeable that the pressure is not zero, even at the end of the ultrasound pulse due to strong reverberations inside the head cavity, although the pressure amplitude is reduced by a factor two. This behavior is also present, albeit with a much lower pressure amplitude left, in the case of pressure curves through the half skull in water due to reverberations between the skull surface and the transducer and inside the coupling cone respectively. In the case of the half-skull, the time profile clearly shows the interferences between the direct and reflected waves which appear to be primarily destructive in the case presented below (t=120 µs…).

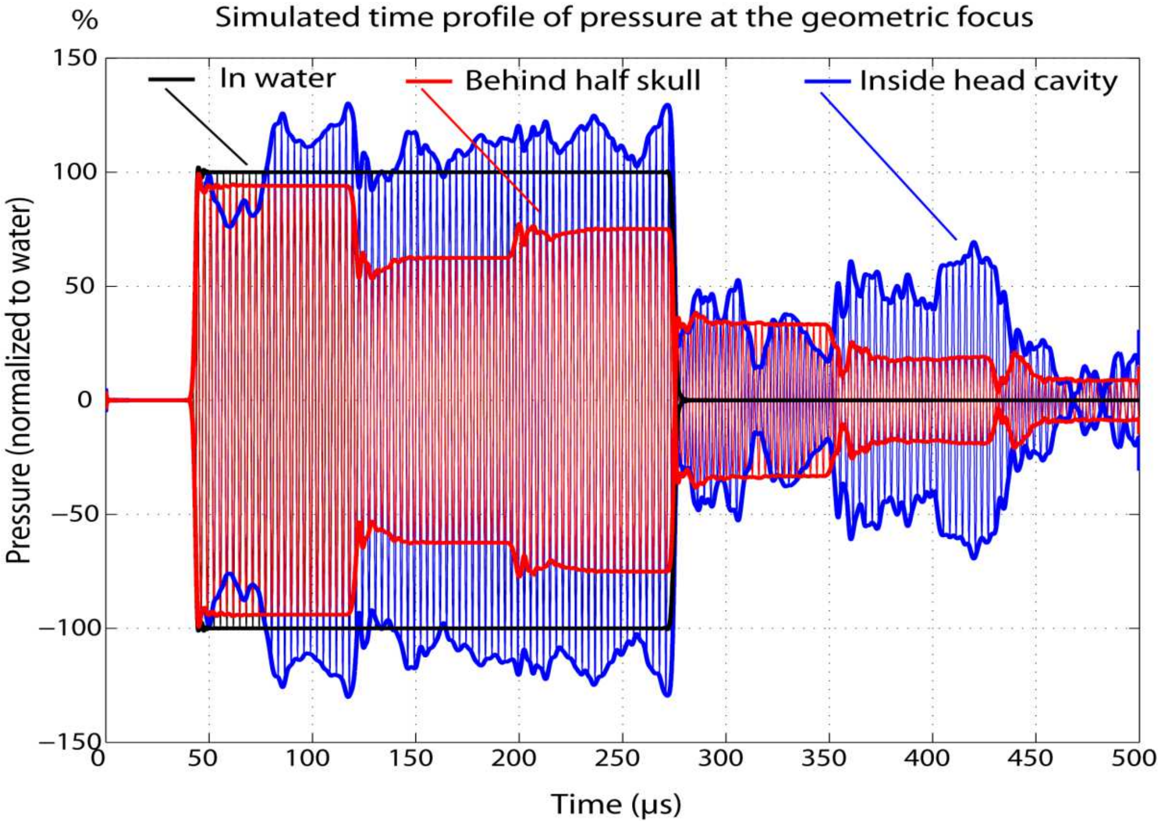

Figure 4.8: Simulated pressure amplitude at the geometric focus as a function of time; in free water (black), in the full head model (blue) and behind the half skull (red).

In order to quantify the overall increase in peak pressure, the spatial peak and time peak pressures were estimated for each configuration and normalized to that corresponding to the free water simulation. Peak pressure maps for the water and full head configuration in the sagittal, coronal and horizontal planes are presented in Figure

4.9. One can notice that the full head configuration shows considerable interference patterns with secondary and shifted peaks and an overall increased peak pressure inside the head due to standing waves. Those patterns arise in the full head and not only inside the animal brain, suggesting that the air-tissue interface is the primary cause of the reverberations in front of the tissue-skull interface, which could be expected given the small thickness of the skull with respect to wavelength.

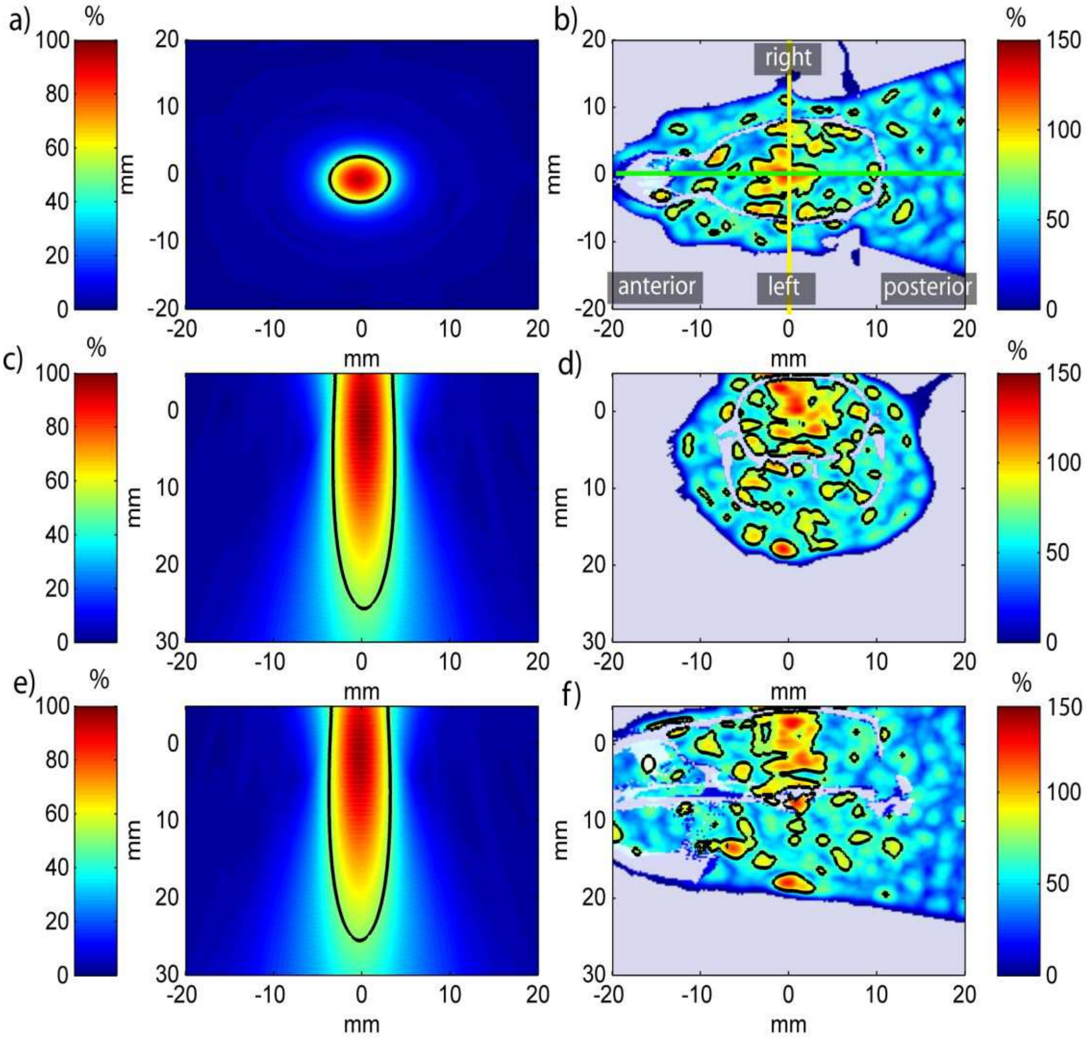

Figure 4.9 (a, b, c, d, e, f): Peak pressure spatial distribution relative to the peak pressure in water (%). Note the change in color-bar scale between the two columns. The isocontour represents half maximum of each configuration. a- Peak pressure map in water (horizontal view). b- Equivalent view for the full head model (skull is represented in white). c- Peak pressure map in water (coronal view). d- Equivalent view for the full head model. e- Peak pressure map in water (sagittal view). f- Equivalent view for the full head model. Views are centered on the geometric focus.

Spatial profiles of the time peak pressure are given in **Figure 4.10**, for the free water and full head configurations along the coronal and sagittal axes and centered at the geometric focus. It is clear from these spatial profiles, that there is both a uniform background pressure of approximately 40% of the spatial peak, time peak pressure in water (approximately 30% of the spatial peak, time peak pressure in the brain) and multiple secondary peaks that are smaller than the focal spot in water, which are typically half-a-wavelength wide and are expected in the case of standing wave interferences forming in a cavity.

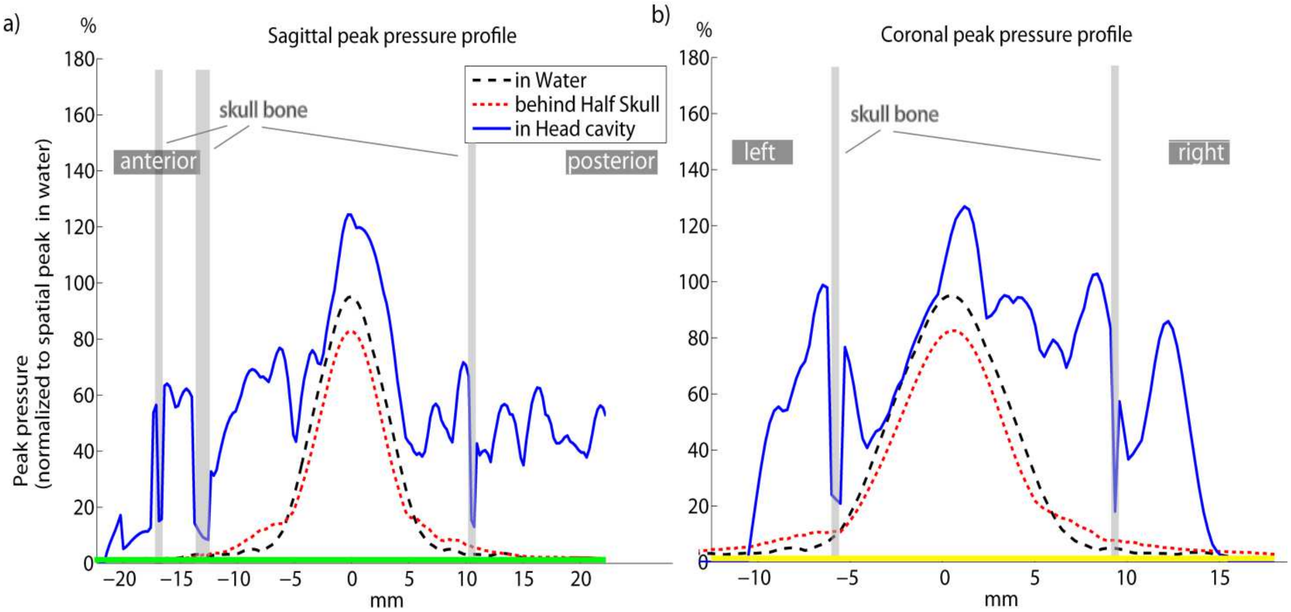

Figure 4.10: Spatial profiles at the geometric focus. a- Coronal axis. b- Sagittal axis. Skull bone is indicated in gray. The profiles show spatial oscillations of approximately half a wavelength typical of standing waves pattern. Although this gives rise to peaks smaller than the focus spot in water, the pressure is not well focused and is distributed over the whole head at approximately 30% of the peak value in the head cavity (40% of the peak value in free water).

As presented in **Table 3**, the spatial peak, time peak pressures were estimated for the half skull and full head configuration and normalized to the spatial peak, time peak pressure simulated in free water. Since part of the transmitted pressure is due to constructive or destructive interferences between the transducer and the half-skull as evidenced by the pressure profile behind the half skull in **Figure 4.8**, we averaged the results over 10 different positions of the transducer when estimating the pressures and intensities.

Simulations of the experiment	Mean ± Std
Spatial peak, time peak pressure behind the half skull normalized to water	1.1 ± 0.2
Spatial peak, time peak pressure inside the head normalized to water	1.8 ± 0.4
Spatial peak, time peak intensity behind the half skull normalized to water	1.1 ± 0.2
Spatial peak, time peak intensity inside the head normalized to water	3.6 ± 1.8
Spatial peak, pulse averaged intensity behind the half skull normalized to water	0.9 ± 0.4
Spatial peak, pulse averaged intensity inside the head normalized to water	2.3 ± 1

Table 3: Simulated pressures and intensities behind the half skull and inside the head normalized to those in free water.

We estimate that the spatial peak, time peak pressure inside the head of the animal has a 1.8-fold increase, on average, due to the reverberations of the ultrasound wave. The standard deviation of this ratio due to the 10 different positions simulated was found to be 0.4 and seems to be due to the destructive or constructive nature of interference between the transducer and animal skull. The spatial peak, pulse averaged intensity showed a 2.3-fold increase for a 3.6-fold increase for the spatial peak, time peak intensity. Intensity and pressure are thus very different from an estimation based on water measurements only and could potentially lead to local tissue heating even when the acoustic intensity was found to be low in water (**Table 3**).

Regarding the transmission through the half skull, we observe on the pressure time profile behind the half skull (red curve in **Figure 4.8**) an initial transmission of 90%, before the interferences start to play a role either destructively or constructively. This value is close to the experimental transmission found on three skulls (cf. **Table 2**).

4.8 Discussion

This work confirms the existence of a pressure threshold in the brain for motor stimulation using transcranial focused ultrasound. The ultrasonic sequence for neuromodulation was based on that described in detail in Nature Protocols (Y. Tufail et al. 2011). Only the pressure amplitude was modified, and all other ultrasonic parameters were kept constant. This enables the study of a single parameter in order to evaluate the existence of a neuromodulation threshold. However, it does not permit conclusions about whether the threshold is a mechanical threshold or a thermal threshold, which remains an open question. In further studies, several different transmit sequences (changing PRF, duty cycle and pressure amplitude) should be used in order to answer this question.

Failure to obtain any motor response was observed in 40% of the attempts, even though the same protocol was followed and was specific for a given animal and a given day. It can be hypothesized that any change in the anesthetic cocktail or in the physiological state of the animal that day can play a major role in these experiments. Even though we suspect anesthesia, no correlation could be made with any specific animal, or the date of the opening of the anesthetic cocktails. When successful (60%), the experiments were consistent for the whole experimental session on a particular day and always demonstrated an acoustic threshold, as shown in **Figure 3.6**a and **Figure 3.6**b. The mean pressure value was 0.68 ± 0.1 MPa (N series=29), measured in water. One should also notice that depending on the anesthesia stage the threshold varied from 0.61 ± 0.03 MPa (N series=3) to 0.77 ± 0.04 MPa (N series=4). The excitability thus appears to be highly dependent on the anesthesia. These pressures are again measured in water, uncorrected for skull transmission or reverberations, and correspond to an average Isppa of 7.5 W/cm^2.

For most experiments on acoustic neuromodulation published in the literature, the acoustic pressure values and Isppa reported correspond to calibration experiments performed in water or behind a half skull only. Our results are consistent with those observed by Yoo (Yoo et al. 2011) on the rabbits who found a Isppa of about 12.5 W/cm^2 using limb movements and considering we used a much lower frequency (320 kHz versus 690 kHz) which is known to reduce the threshold (T. Tufail et al. 2010)(King et al. 2013). Comparison with other published studies is difficult due to the different protocols involved in terms of motor threshold definition (EMG statistics versus limb movement), species, acoustic parameters or anesthesia levels (T. Tufail et al. 2010)(King et al. 2013).

Based on our numerical simulations, the acoustic pressure induced *in situ* was found to be strongly biased by the influence of ultrasound reverberations in the head cavity. The tissue-air interfaces were found to be predominant in generating such reverberations compared to the tissue-skull interfaces. In simulations, taking into account only the half skull transmission does not yield an accurate estimation of the acoustic pressure inside the animal head.

At 320 kHz, a mean 1.8-fold increase in spatial peak, time peak pressure inside the rat head compared to free space simulations was determined here. This indicates that the acoustic pressure threshold for motor threshold, which was found to be around 0.7 MPa based on free water measurement, should be corrected to approximately 1.2 ± 0.2 MPa. A 2.3-fold increase was found for the pulse-averaged intensity. This indicates that the maximum energy deposition in the brain is two times higher than expected and thermal effects could thus be higher than anticipated.

Applying these corrections on the estimation of the Mechanical index (MI) and Intensity Spatial Peak Pulse Average (Isppa) would yield a threshold of respectively MI=2.2 for the mechanical index and Isppa =17.5 W.cm^{-2}.

The correction of such biases should be taken into account when comparing results obtained with different frequencies, as well as the results from different species with significantly different head size, since, in both cases, the reverberations should be highly dependent on those parameters.

Moreover, the spatial distribution of pressure field using the 320 kHz ultrasound transducer was found to be strongly spread over the entire brain with much of the brain still receiving approximately 30% of the peak pressure *in situ*. Moreover, many secondary peaks were found, with a size of half a wavelength smaller than the focal spot in free water and typical for interferences pattern.

Even though the locations of the secondary peaks were not linked to any specific structure on a brain atlas, such random sub-wavelength peaks could provide new insight into the fine activations sometimes observed, such as for a single whisker or eye movement, which involve very small brain structures. It cannot be excluded, however, that these specific activations are simply the results of lower activation thresholds in the corresponding structures due the anesthesia level or to the brain activity state.

The results show that the neurostimulating acoustic field is much more complex than a single localized acoustic spot at the geometric focus. Combined with the intrinsic variability and complexity of the brain activity and its dependence on the anesthesia level and sleep state, it might be difficult to assess the mechanisms behind neuromodulation in such configurations. Simpler configurations that are less prone to reverberations, such as shorter pulse, higher frequencies, or chirps (Tang and Clement 2010; Deffieux and Konofagou 2010; O'Reilly, Huang, and Hynynen 2010), or simply larger animals could help in further simplifying the acoustic problem and looking at the neuromodulation effect itself. For a given frequency, such reverberation effects and pressure field distortion should be much lower in primate or human heads due to the larger size of the head. Additional numerical and experimental studies (Deffieux and Konofagou 2010) will be required to quantify this effect when investigating motor thresholds and safety in those species.

4.9 Conclusion

A transient motor response has been elicited in anesthetized rats by 320 kHz transcranial ultrasound in more than 60% of the experimental sessions, with a pressure threshold estimated at 0.68 MPa (Isppa = 7.5 W.cm^{-2}, Mechanical Index=1.2) as measured in free water. In some cases, the stimulation of very specific structures such as the occulomotor system or a single whisker was observed, even though the wavelength at 320 kHz is approximately 5 mm. Simulation using a finite-difference-time-domain software and CT scan shown ultrasound reverberations in the head cavity yielding a 1.8-fold increase of the spatial peak, time peak pressure compared to free water and a 2.3-fold increase of spatial peak, pulse averaged intensity. At this low frequency, several sub-wavelength peaks are also created. The acoustic field resulting from the reverberations needs to be carefully taken into account for small animal studies at low frequencies. Switching to larger animals (primates for example) would allow a better control of the ultrasonic field in the head.

Chapitre 5 **Neuromodulation on the awake monkey**

5.1 Introduction

Compared to Transcranial Magnetic Stimulation (TMS), low intensity ultrasonic neuromodulation shows great promise, because it is non-invasive and has a high spatial resolution. Nevertheless, we saw in the previous chapter that achieving neuromodulation in rodent models was not straightforward. Anesthetized animals with a Ketamine/Xylazine mixture respond to ultrasonic neuromodulation only within a 15min time window and with high variability. Moreover, at the low frequency suitable for ultrasonic neuromodulation, the rodent head forms a cavity where ultrasonic waves reverberate and create a complex pattern difficult to predict.

Another reason to consider another animal model is that, in the future, ultrasonic neuromodulation has the potential to become an alternative to TMS. Working on awake animals would help translating the technique to the clinic, and achieve neuromodulation on an animal much closer to humans: primates - ideally awake monkeys. In collaboration with Pierre Pouget’s team at Institut du Cerveau et de la Moelle (ICM), we performed neuromodulation experiments in the Frontal Eye Field (FEF) of two awake Maccacas using a protocol directly derived from transcranial magnetic stimulation experiments : the antisaccade paradigm.

5.1.1 Frontal Eye Field

In primates, the Frontal Eye Fields (FEF) is a sophisticated cortical brain area that plays an important role in the control of visual attention and eye movements **Figure 5.1**. Invasive intracortical microstimulation has been widely used in combination with oculometric measurements and mapping techniques, such as electrophysiological and fMRI recordings in non-human primates. These approaches have provided causal evidence about the role of the FEF, with direct bearing on oculomotor functions (Huerta, Krubitzer, and Kaas 1987)(Marrocco 1978). More recently, the causal contributions of the FEF in attentional orienting has been demonstrated (Moore and Fallah 2001) as well as its ability to influence different aspects of visual perception (Moore and Armstrong 2003)(Ekstrom et al. 2008).

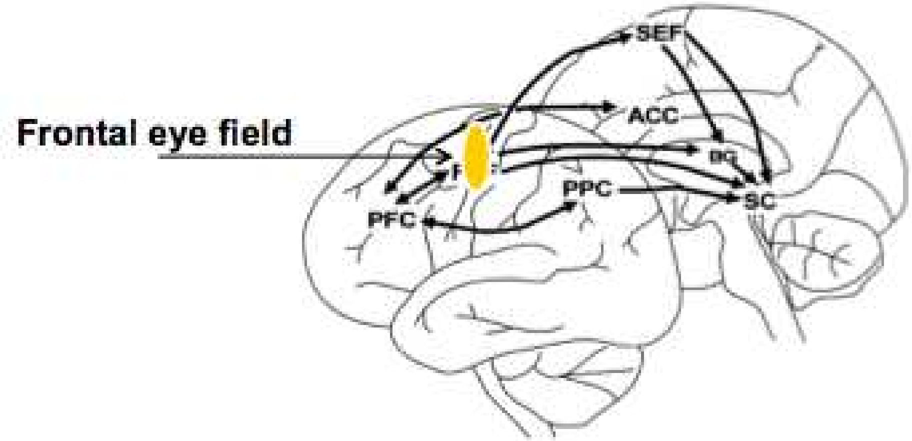

Figure 5.1: Schematic representation for the Frontal Eye Fields (FEF) in primate

5.1.2 Antisaccade

In addition to looking towards new visual targets, an important part of saccadic behaviour is to suppress eye movements that would be made to novel but behaviourally irrelevant stimuli. To investigate such control of voluntary versus reflexive saccades, a special test paradigm called the antisaccade task has been developed (Figure 5.2). In this task, the subject is required to suppress a saccade (the `prosaccade') towards a stimulus that appears in the periphery of vision and instead generate a voluntary saccade of equal size towards the opposite side (the `antisaccade'). After time for the antisaccade to be made, a target light is turned on at the correct location to check the accuracy of the movement (Fischer and Weber 1998). The simplest measure of the response to this test concerns the direction of the initial saccade, expressed as the ratio of antisaccades to prosaccades; this can be tested at the bedside (Currie 1991). Normal subjects initially make frequent errors in this task, but after a brief period of practice, error rates fall below 15 percent. Functional imaging studies have shown that FEFs are activated bilaterally during both prosaccades and antisaccades, but more so for the latter (Connolly et al. 2002)(DeSouza, Menon, and Everling 2003). The right hemisphere DLPC has also been shown to be activated during antisaccades (DeSouza, Menon, and Everling 2003). However, it has been reported that, at the cortical level, only patients with discrete lesions affecting the Dorsolateral prefrontal cortex (DLPC) have an increased percentage of errors in the antisaccade test (Pierrot-Deseilligny C, Müri, R M. Ploner, C J. Gaymard, B. Demeret, S. Rivaud-Pechoux 2003); in contrast, patients with FEF lesions had a normal percentage of errors on the antisaccade task, but their correct anti-saccades were made at increased latency. Thus, it has been suggested that, during the antisaccade task, inhibition of reflexive misdirected saccades is due to the DLPC, whereas triggering of the intentional, correct antisaccade depends upon the FEF (Rivaud et al. 1994)(Pierrot-Deseilligny C, Müri, R M. Ploner, C J. Gaymard, B. Demeret, S. Rivaud-Pechoux 2003). In a patient with a discrete brainstem lesion, increased distractibility was attributed to interruption of a pathway from the DLPC to the superior colliculus (Gaymard et al. 2003). Whether the FEF is also important for suppression of reflexive saccades is disputed (Pierrot-Deseilligny C, Müri, R M. Ploner, C J. Gaymard, B. Demeret, S. Rivaud-Pechoux 2003).

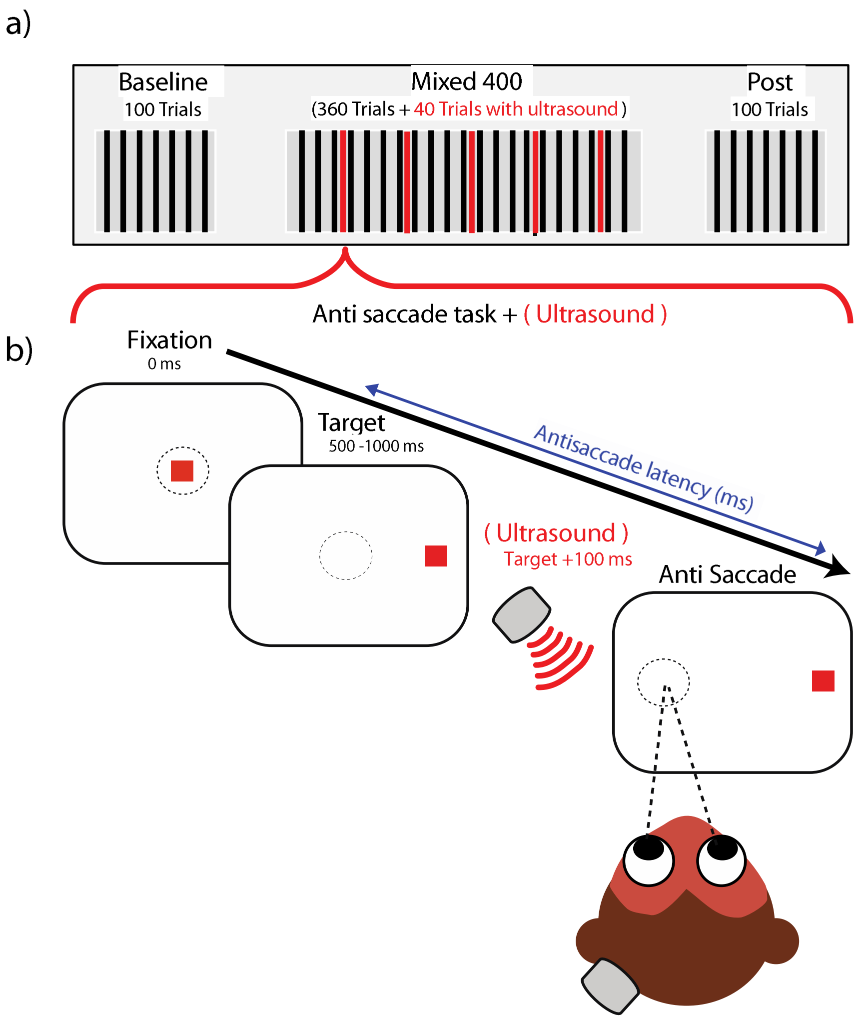

Figure 5.2 (a,b): a) Experimental session. One session consists of three blocks with left and right (50%) anti-saccade trials (100 trials for the baseline, 400 trials including 40 trials with ultrasound during the central block and 100 trials as a post block). b) The Antisaccade Paradigm. Monkeys were required to initially keep fixation on a central stimulus. After initial fixation onset, a red square (target) appeared right or left. Monkeys were trained to initiate as soon as possible a saccade towards the opposite direction. During ultrasound trials, 320 kHz ultrasound was applied for 100 ms, 100 ms after the target appearance.

5.1.3 Objectives

We used focused ultrasound on macaque frontal brain areas to interfere with the activity of antisaccade preparatory processes driven by spatial visual stimuli. More precisely, we decided to induce focused ultrasound driven interferences on the FEF, a complex area hosting highly overlapped networks likely to be involved in functions such as sensory integration, attentional orienting, oculomotor planning, saccade execution, spatial short term memory, visual detection, discrimination and visual awareness (Moore and Fallah 2001)(Connolly et al. 2002)(DeSouza, Menon, and Everling 2003)(Rivaud et al. 1994)(Kanai, Muggleton, and Walsh 2012)(Kirchner et al. 2009)(Kirchner et al. 2009)(Gerits et al. 2012). Our short-term goal was to demonstrate the feasibility of online focused ultrasound experiments in awake and freely performing non-human primate. Such an approach has the potential to clarify in the near future some of the mechanisms underlying the effects of focused ultrasound, and serve to the causal non-invasive exploration of cognition in non-human primate models.

5.2 Focused ultrasound

A single element focused ultrasound transducer (H115, Sonic Concepts, Bothell, WA, USA) (central frequency 250KHz, diameter 64mm, FD# 1) was used in these experiments. A coupling cone (C103, Sonic Concepts, Bothell, WA, USA) filled with degassed water was placed between the transducer and the animal head. The transducer was fixed on a mechanical arm with 4 rotation axes (Viewmaster LCD, Osmond Ergonomics, Wimborne, UK) to provide the flexibility for the positioning and orientation of the transducer over the tattooed target as can be seen in **Figure 5.3**. A thin layer of echographic gel (Aquasonic 100, Parker Laboratories Inc., Fairfield, NJ, USA) was applied on the skin and on the membrane of the coupling cone to ensure acoustic coupling.

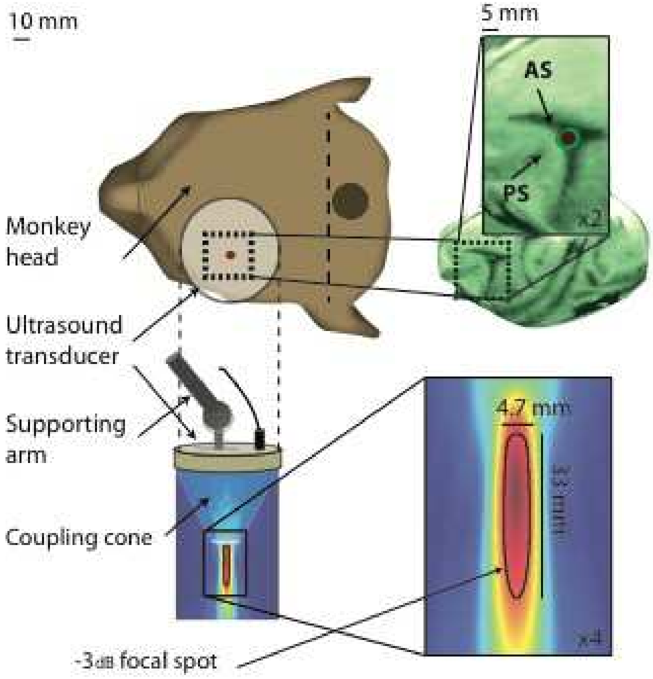

Figure 5.3: The ultrasonic transducer is manually positioned so that the cigar-shaped focal spot target the left Frontal Eye Field (FEF). A coupling cone filled with water ensures the ultrasonic coupling between the transducer and the animal's head.

The ultrasound frequency was set to 320 kHz (peak frequency of the transducer) with a pressure amplitude of 0.6 MPa (as measured in free water, see effects of skull below) using a first function generator (33250A, Agilent, Santa Clara, CA). The pulse duration was set to 100 ms (number of cycles 32000), with rise and fall times of 1 ms using a second function generator (AFG3101, Tektronix, Melrose, MA) which was connected to the amplitude modulation entry of the first generator. This setup is based on Tufail & al (Y. Tufail et al. 2011) and allows the testing of different waveform configurations. In this thesis all sonications are restricted to a single configuration with the simplest case of a single ultrasonic pulse.

A 75 Watts amplifier (75A250A, Amplifier Research, Souderton, PA) was then used to deliver the required power to the transducer and the input voltage of the transducer was monitored using voltage probe (P6139A, Tektronix, Melrose, MA) connected to an oscilloscope (TDS2022B, Tektronix, Melrose, MA).

The transducer was calibrated in degassed water behind a primate skull (Maccaca Mulatta skull) with a custom built heterodyne interferometer. An heterodyne interferometer uses a laser beam to detect the small vibration of the ultrasound wave on a mylar membrane which is then converted to pressure with very high sensibility and a flat frequency response.

The transmission of the pressure through the degassed primate skull was assessed at 7 different randomly chosen points on the skull (Figure 5.4). The transmission was found to be 58.2% ± 8.3%. The in situ pressure delivered to the monkey brain transcranially can thus be corrected to 0.35 ± 0.05 MPa.

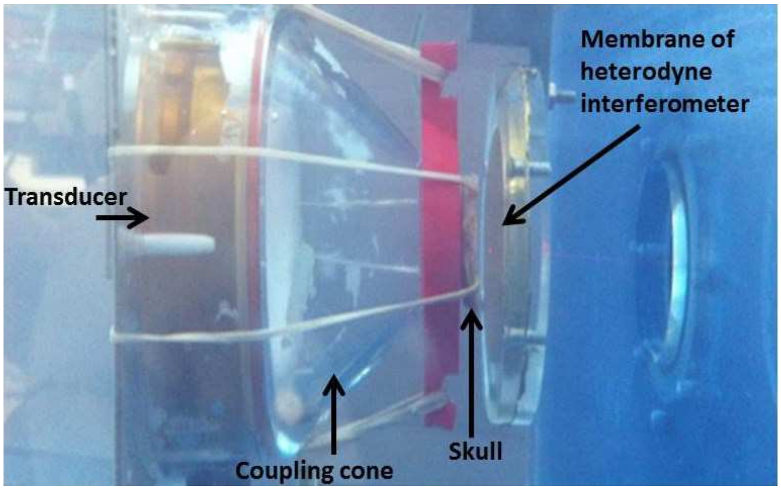

Figure 5.4: Image showing the position of the primate skull between the transducer and the heterodyne interferometer

The equivalent Mechanical index (MI) value is 1.07 with an Intensity Spatial Peak Pulse Average (Isppa) of 11.68 W/cm^2 in free water, those values need to be corrected to respectively MI = 0.62 ± 0.09 and Isppa = 4.04 ± 1.14 W/cm^2 behind the primate skull. By taking into account the pulse duration and repetition frequency (respectively 100 ms and 30 s) during the neuromodulation sequence, the Intensity Spatial Time Average (Ispta) can be estimated to 38.96 mW/cm^2 in free water and 13.46 ± 3.78 mW/cm^2 behind the primate skull. Even though the frequency is lower than for typical ultrasound imaging, they are all much below the Food and Drug Administration (FDA) limitations for ultrasound imaging safety guidelines (MI = 1.9, Isppa = 190 W/cm^2; Ispta = 720 mW/cm^2) ensuring that the parameters used here are completely safe as defined by the FDA.

5.3 Task

Prior to the first experimental session, animals were specifically trained in an antisaccade (AS) paradigm,

In the middle of the screen which is -16 to +16 degree in size, a green spot in a 10 degree window appears at the beginning. When the monkey looks at the green spot for a short period of time, we reward him with a drop of water. Then we decrease the window to 5 degrees. This requires a week of training.

Pro-saccades: the central spot (target) appears for 500-1000 millisecond, and then the target appears on one side, either the right or the left side. When the monkey looks at the target on the right or left, he is rewarded with a drop of water. This requires three weeks of training.

Anti-saccades: the most difficult test which requires four months of training. The first stage: the central target appears in brown, and simultaneously, two targets appear on both sides of the central target, one on the right and the other on the left, one in red and the other in green, but both have the same size of the central target, 1 degree. The monkey here should look at the green target not the red one (64 pixel2 = 8x8 pixel). This requires one week of training. We then start to decrease the size of the green target that appears on the side to 1 pixel. This requires eight weeks of training. Then the green target that appears on the side disappears completely and in that configuration it requires two months to teach the monkey to look at the opposite side of the red target Figure 5.2(b). When the monkey has learnt and got good at this, we can start our experiment. We accepted a relative error of 15% in pointing at the exact target.

Failure to trigger a saccade within 2000 msec after target onset cancelled the trial. The AS task was chosen since prior human and monkey TMS experiments have revealed prosaccade paradigms to be much less sensitive to single pulse TMS interference than antisaccades (Olk et al. 2006).

Eye movements were recorded with an infra-red eye tracker (Eyelink 1k, SR-Research, Ontario, Canada), and eye position was digitized and sampled at 1000 Hz and stored for off-line analyses. Visual paradigms and data acquisition were under the control of a computer running a real-time data acquisition system (Rexeno software; for further details see (Pouget et al. 2010)(Valero-Cabre et al. 2012). Saccades were detected using homemade matlab scripts that searched first for significantly elevated velocity (> 30°/s). Saccade initiation and termination were then defined as the beginning and end of the monotonic change in eye position lasting 12 ms before and after the high-velocity gaze shift. On the basis of the 1000-Hz sampling rate, this method is accurate to within 1 ms.

5.4 Experimental protocols

Two captive-born macaques (Maccaca Mulatta, “Y”, and “L”) participated in this study. The monkeys were paired-housed and handled in strict accordance with the recommendations of the Weatherall Report on good animal practice. Monkey housing conditions, surgical procedures and experimental protocols were all carried out in strict accordance with the National Institutes of Health guidelines (1996) and the recommendations of the EEC (86/609) and the French National Committee (87/848). The authorization for conducting our experiments in the institute was delivered by the Animal Health and Veterinary Medication Division of the Department of Public Veterinary Health, Nutrition and Food Safety of the French Ministry of Health (last renewals. no. Arrêté prefectoral N° DTPP 2010-424). Our routine laboratory procedures included an environmental enrichment program where monkeys had access to toys, mirrors and swings. Monkeys also had visual, auditory and olfactory contact with other animals and, when appropriate, could touch/groom each other. Any possible pain associated with surgery was pharmacologically ameliorated by means of a daily injection of Ketofen (0.03ml/kg) or Buprecare (0.067ml/kg). An institutional veterinary doctor constantly monitored the well-being and health conditions of the monkeys. Prior to participating in the study, both animals were periodically chaired, head-posted and trained to perform a series of tasks for a period of 6-12 months, until they became regular and proficient performers.

5.5 Surgical procedure

After buying the two monkeys, they were isolated in a cage for ten days in order to make sure they are not bearing any diseases. A plastic collar was placed around the neck of each one. They were trained to take the fruit from our hands to build trust between us. This usually happens in ten days. They were trained after that to approach the special chair that is related to the experiment by themselves. Then, fruit and water was given to them while they were on the chair only, not in the cage. This process took two weeks. The next step was the most difficult one: to train the monkey to extend his head out of the chair. This took two more weeks. When the monkey learned to approach the chair alone and extend his head through the chair every day, he became ready to have the head-post placed into his head. The surgical procedures for titanium headpost implant were the same as previously published (Pouget et al. 2010)(Valero-Cabre et al. 2012).

After preparing the room and sterilizing and disinfecting the instruments, we first injected the monkey with ketamine hydrochloride (5 mg/kg i.m.) to induce the anesthesia. Then we took him to the operating room. Then we continued the anesthesia with 3-4% isoflurane gas via a dedicated mask that facilitates the intubation process. After the intubation anesthesia was reduced to 2% Isoflurane with oxygen (0.5 L/h). We placed the head of the monkey in a stereotactic device. Then we injected the monkey with antibiotics and analgesics intravenously.

Heart rate, O2 saturation and temperature were monitored. With a sterile scalpel we opened the scalp and then removed the muscles and periosteum. The area was cleaned with Betadine and sterile saline. Holes were drilled in the skull to install the head post. Head posts (9/32” or 7.1 mm internal diameter) were commercially available as Part \#6-FHP-X2F produced by Crist Instrument, Hagerstown, MD, USA. They had an "X"-shaped footplate designed for attachment to the skull with a total of 12 titanium bone screws Figure 5.5.

Figure 5.5: Head post (12 holes)

The vertical post had a tapered cross section, designed to mate with a headpost holder (see Part \#6-FHB-S2B, Crist Instrument, Hagerstown, MD, USA, Figure 5.6).

Figure 5.6: Head post holder

The skin was finally sutured with absorbable sutures. We put cement in the head post (Figure 5.7). Isoflurane was stopped and O2 was left only, until the monkey woke up and extubated himself alone. The whole procedure time was 3 hours. We then took the monkey back to the cage.

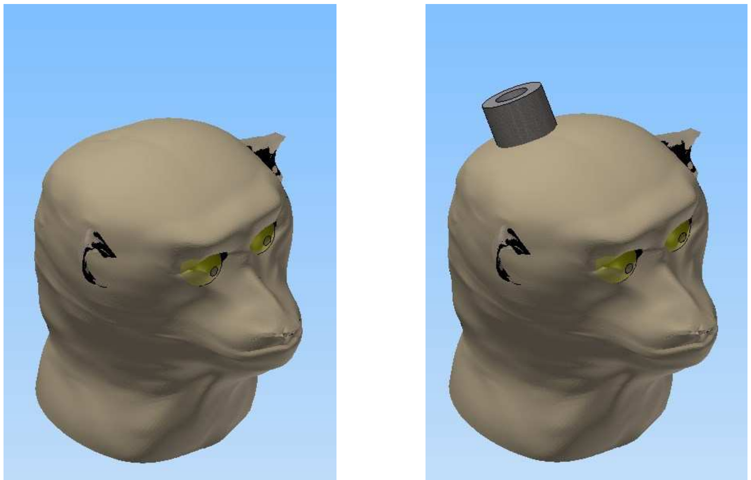

Figure 5.7: Monkey before performing surgery (Left), Monkey after surgery (right).

In monkey ‘Y’ the center of the head post was located adjacently caudal to the stereotaxic zero bar, aligned with the interauricular scalp line. In monkey ‘L’ the headpost was placed slightly more rostral than in monkey ‘Y’ (Figure 5.8).

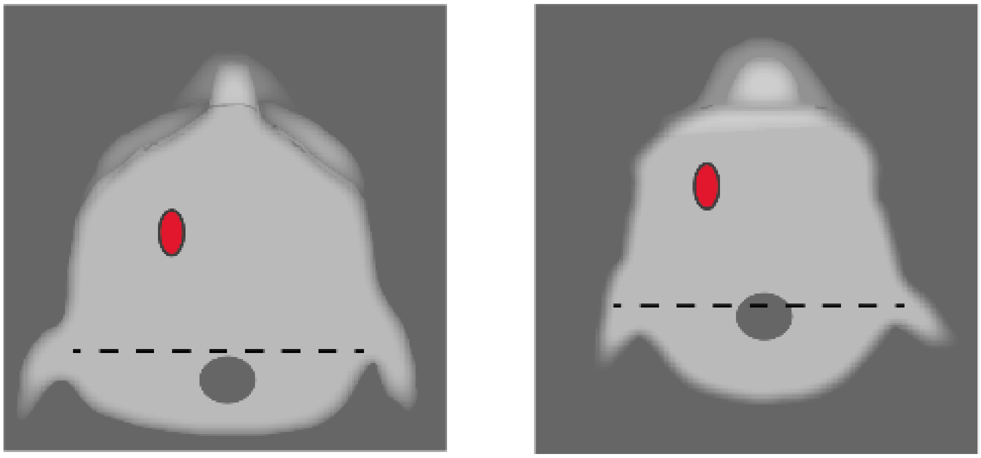

Monkey Y

Monkey L

Figure 5.8: FUS stereotaxic placement

Six months are needed after surgery for complete recovery of the monkey. The first fixation of the head to the chair has to be short (30 minutes), with more positive reinforcement (fruit and water) than usual, for the monkey to be as calm as possible in the chair.

The FEF field was identified using stereotaxic coordinates. Its site was labeled with a color tattoo on the monkey skin, which lasted for several weeks and was renewed when fading. FUS pulses were delivered at a 100 ms stimulus onset asynchrony interval (SOA), post visual target appearance, which was selected based on preliminary monkey's saccade latency measurements. In order to keep conditions as similar as possible during sham FUS sessions, the transducer was first placed above the expected location for FEF region and then moved up 4 cm above the skin, keeping an identical orientation.

For each experiment session, animals performed a total of 3 blocks of AS training. First, monkeys performed a 100 trials block of AS (50 for each side) as baseline. Then, a second block of 400 trials was done: 360 trials without FUS (180 for each side) and 40 trials with FUS (20 for each side) were presented. Trials with FUS were pseudo-randomly interleaved with trials without FUS. A last block of 100 trials was performed as post-test. Monkey Y performed 10 sessions and monkey L 12 sessions.

5.6 Data analysis and presentation

Trials in which blinking responses interfered with eye recordings, or incomplete AS, were eliminated from the data set. The AS latency for each individual trial was calculated as the time between stimulus presentation and the onset derivative of the eye saccade velocity reaching a speed of 30°/s. Individual AS latency values were averaged for trials with FUS (focused ultrasound trials) and compared to those without stimulation (no-focused ultrasound trials), for each session and each experimental condition explored in the study on each monkey.

5.7 Results

5.7.1 Focused ultrasound-modulated antisaccade latencies

As shown in **Figure 5.9**, FUS stimulation did affect antisaccade latencies. More specifically, across the experimental sessions, ipsilateral mean AS latencies with ultrasound stimulation were significantly slowed (monkey Y: *p*= 0.04; monkey L: *p*< 0.001) compared to the non-stimulation condition (monkey Y: noUS= 219 ms US= 233 ms ; monkey L: noUS= 236 ms US= 251 ms).

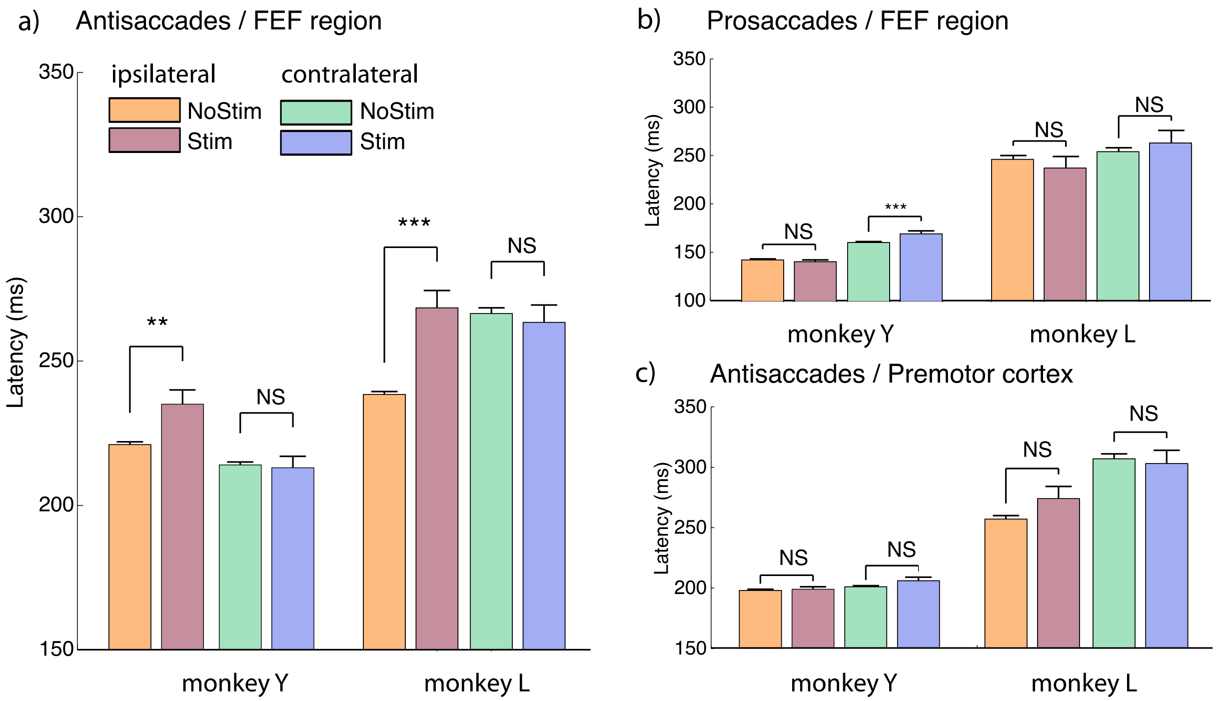

Figure 5.9 (a,b,c): a) Ipsilateral and contralateral antisaccades mean latencies with and without ultrasound on both monkeys. Ispsilateral antisaccade latencies are significantly slowed (p<0.05) with ultrasound. b) Same with prosaccade tasks. c) Antisaccades latencies when the transducer is positioned over the premotor cortex. No significant changes in latencies are observed. Error bars represent standard errors over all trials.

For the two animals, contralateral mean AS latencies were not significantly slowed (t-test: monkey Y: *p*= 0.6; monkey L: *p*= 0.09) compared to the non-stimulation condition.

A sham stimulation has also been performed while the transducer was placed on the side of the animal head, so that the ultrasound beam was reflected by air and no ultrasonic signal could be transmitted to the head of the animal. In both monkeys, sham focused ultrasound did not interfere with ipsi or contralateral saccade latency ($p > 0.5$).

5.7.2 Focused ultrasound Effect on Antisaccade Error Rate and Amplitude

The impact of focused ultrasound stimulation over FEF on AS error rate was statistically tested separately for each condition. Ipsilateral error rate AS with ultrasound stimulation were not different to the non-stimulation condition ($p > 0.5$, across conditions and animals). Contralateral error rate AS increased marginally with ultrasound stimulation (US= 9 % ±5.7 error US= 5.1 % ±3.1 error, $p=0.05$) only for monkey Y. The US pulses did not affect eye movement metrics. As compared to sham non-stimulated trials, amplitude of eye movement during trials with US did not significantly vary in any of the experimental conditions ($p>0.5$, for all conditions in both animals).

5.8 Discussion

The study demonstrates the feasibility of using focused ultrasound to modulate behaviour in awake non-human primate brain causally.

In this study, continuous pulses of ultrasound of duration 100 milliseconds were used with a low frequency 320 kHz and a low pressure amplitude, estimated at 0.35 MPa *in situ* (*corresponding* MI : 0.62). A pause time of at least 30 seconds was implemented between each pulse (corresponding Ispta: 13.5 mW/cm^2). Such conservative values were used to ensure that they was no possible damage to the neural tissue. This sequence is well below the Food and Drug Administration (FDA) limitations for transcranial ultrasound imaging safety guidelines (MI = 0.62 < 1.9, Isppa = 4 W/cm^2 < 190 W/cm^2; Ispta = 13.5 mW/cm^2 < 94 mW/cm^2) ensuring that the parameters used here are safe and could be used for imaging in human brain. Even though the center frequency and pulse duration are very different than those used for brain ultrasound imaging, it is particularly interesting that the neuromodulation effect is significant with these conservative parameters. Our group and others have recently reported on the ultrasonic motor threshold of anesthetized rodents which was found to be around 1.2 MPa *in situ* (Younan et al. 2013)(King et al. 2013). By using higher-pressure amplitude and by targeting the motor cortex of the monkeys, the next step would be to try to elicit a motor response in the awake monkey as it has been demonstrated with transcranial magnetic stimulation (Valero-Cabre et al. 2012).

Compared with the effect obtained with optogenetic manipulation (Szobota et al. 2007)(Zhang et al. 2007) our results with focused ultrasound appear to be as effective (lengthening ipsilateral movement) and as strong (5-20 ms). Compared with the moderate modulation of response times observed with TMS (shortening ipsi and contra lateral movement (Hallett 2000)) our results appear to be less affected by baseline variability of response times (no normalization was required) and no discomfort has been noticed for the animals. Even though the exact mechanisms are still unknown, ultrasonic neuromodulation is believed to be mechanical rather than thermal in origin, as illustrated by experimental evidence on rodents where lower frequencies yield lower motor thresholds (King et al. 2013): this is a typical behavior for mechanical effects whereas thermal effects would be more intense for higher frequencies due to increased tissue absorption.

Low frequencies have been favored in most recent neuromodulation studies. Indeed, the phase aberrations induced by the skull are less for low frequencies, so that the lower the frequency, the better the transcranial focusing will be. The lower the frequency the lower the transmission loss through the skull (here approximately 50% at 320 kHz), making it easier to target the brain non-invasively.

Nevertheless, using higher frequencies would yield smaller focal spots and thus a higher targeting resolution. At 320 kHz, the focal spot is approximately 35 mm long and 5 mm wide (approximately 400 mm^3). This is already better than can be achieved with transcranial magnetic stimulation and could be achieved at any depth in the brain. It is our goal, in future studies, to estimate experimentally the targeting resolution of our setup by targeting smaller and deeper structures in the brain and to investigate higher frequencies up to 1 MHz. Using phase correction techniques and a programmable 1 MHz multi-elements array (Pernot et al. 2007), it should be possible to obtain a targeting resolution of approximately 14 mm3 anywhere in the brain for such low in situ intensities. The possibility that focused ultrasound can modulate small and deep brain structures has crucial implications for treatment of numerous disorders *e.g.* Parkinson's disease, essential tremor, or disorders of consciousness. Ultrasound neuromodulation is thus a promising and competitive neuromodulation technique, especially compared to transcranial magnetic stimulation, with a higher resolution, a larger targeting envelope and the absence of noise or mechanical vibrations during the stimulation. Although the mechanism behind the focused ultrasound neuromodulation is still unknown, the modulatory potential of this non-invasive and spatially specific tool warrants further investigation in awake non-human primates.

5.9 Conclusion

Focused ultrasound (US) stimulation of awake primates in the left frontal eye field (FEF) influences the anti-saccade latencies. Ipsilateral mean AS latencies with ultrasound stimulation were significantly slowed compared to the non-stimulated condition (monkey Y: noUS= 221 ms US= 235 ms; monkey L: noUS= 239 ms US= 269 ms). For the two animals, contralateral mean AS latencies were not significantly slowed (t-test: monkey Y: p> 0.8; monkey L: p> 0.6) compared to the non-stimulated condition.

The study demonstrates the feasibility of using focused ultrasound brain neuromodulation to causally modulate high-level cognitive behaviour and opens the door for further parametric studies. In particular, it would be of interest to investigate whether ultrasounic neuromodulation is able to transiently stop tremor when focusing ultrasound in the thalamus as this would help to refine the location of the target for the treatment of essential tremor.

General Conclusion

In this thesis, we have investigated two techniques to achieve a safer planning for essential tremor treatments with transcranial MR guided focused ultrasound. We have shown that the Keyhole technique can be used to minimize ultrasonic energy deposition at the target while imaging the location of the focal spot with pulsed ultrasound. The MR ARFI keyhole technique is known to improve the temporal resolution and to produce undistorted two-dimensional images compared to EPI sequences. Nevertheless, we showed that this acceleration technique is dependent on the US focal spot size. The coincidence between the phase-encoding orientation and the longest axis of the focal spot allowed preserving up to 75 % of the original intensity at the focal spot with a keyhole acceleration factor of eight. Simulation and experiment were in good agreement. The method offers a good compromise between spatial resolution, SNR and scan time and could be valuable for adaptive focusing procedures and acoustic beam visualization.

Furthermore, we investigated the feasibility for directly modulating brain activity locally with ultrasound. Such a modulation would be of interest for checking if the defined target in the VIM is indeed responsible for the tremor. We thus investigated transcranial ultrasonic neuromodulation at low frequency (320 kHz) on anesthetized rats and we estimated the motor threshold to be 0.68 MPa (Isppa = 7.5 W.cm^{-2}, Mechanical Index=1.2) as measured in free water. The corresponding acoustic pressure distribution inside the brain, which cannot be measured in vivo, was investigated with numerical simulations of the ultrasound propagation inside the head cavity. Numerical simulations have shown that the pressure distribution in the head is complex and showed ultrasound reverberations in the head cavity yielding a 1.8-fold increase of the spatial peak, time peak pressure compared to free water and a 2.3-fold increase of spatial peak, pulse averaged intensity. Although the rat model is useful for performing initial low intensity neuromodulation experiments, it is not suitable for providing an understanding of the neuromodulation effect in awake conditions or within a larger skull cavity.

Finally, for the first time, we used low intensity FUS stimulation to causally modulate behavior in an awake nonhuman primate brain. We showed that the latency of an anti-saccade task was significantly delayed ($p < 0.05$) in the presence of ultrasonic beam focused in the Frontal Eye Field. Sham experiments did not show any significant change in the latencies.

These promising results will hopefully help guide the treatment of essential tremor during upcoming clinical trials at Institut du Cerveau et de la Moelle with the 1MHz multielements array developed at the Langevin Institute in collaboration with SuperSonic Imagine. The Keyhole technique has been validated with this device. Some work remains to be done before neuromodulation can be achieved with the 1MHz device: all neuromodulation experiments have been conducted with a 320kHz single element transducer and neuromodulation at higher frequencies needs to be investigated. For that purpose, a 1MHz single element transducer, with the same geometry, is being investigated as a next step will be tested on the monkeys toward the clinical goal of achieving neuromodulation with the 1MHz multielements array.

Acknowledgements

This thesis was partially funded by a scholarship from the University of Damas. This work was supported by LABEX WIFI (Laboratory of Excellence within the French Program ‘‘Investments for the Future’’) under references ANR-10-LABX-24 and ANR-10-IDEX-0001-02 PSL and by the Agence Nationale de la Recherche under the program ‘‘Future Investments’’ with the reference ANR-10-EQPX-15.

Bibliographie

Aubry, J-F, M Pernot, F Marquet, M Tanter, and M Fink. 2008. “Transcostal High-intensity-focused Ultrasound: Ex Vivo Adaptive Focusing Feasibility Study.” *Physics in Medicine and Biology* 53 (11) (June 7): 2937–51. doi:10.1088/0031-9155/53/11/012.

Aubry, J-F, M Tanter, M Pernot, J-L Thomas, and M Fink. 2003. “Experimental Demonstration of Noninvasive Transskull Adaptive Focusing Based on Prior Computed Tomography Scans.” *The Journal of the Acoustical Society of America* 113 (1) (January): 84–93. doi:10.1121/1.1529663.

Borrelli, M J, K I Bailey, and F Dunn. 1981. “Early Ultrasonic Effects Upon Mammalian CNS Structures (chemical Synapses).” *The Journal of the Acoustical Society of America* 69 (5) (May): 1514–6.

Botros, Y Y, E S Ebbini, and J L Volakis. 1998. “Two-step Hybrid Virtual Array Ray (VAR) Technique for Focusing Through the Rib Cage.” *IEEE Transactions on Ultrasonics, Ferroelectrics, and Frequency Control* 45 (4) (January): 989–1000. doi:10.1109/58.710577.

Chauvet, D, L Marsac, M Pernot, A-L Boch, R Guillevin, N Salameh, L Souris, et al. 2013. “Targeting Accuracy of Transcranial Magnetic Resonance-guided High-intensity Focused Ultrasound Brain Therapy: a Fresh Cadaver Model.” *Journal of Neurosurgery* 118 (5) (March 1): 1046–52. doi:10.3171/2013.1.JNS12559.

Chen, J, R Watkins, and KB Pauly. 2010. “Optimization of Encoding Gradients for MR-ARFI.” *Magnetic Resonance in Medicine : Official Journal of the Society of Magnetic Resonance in Medicine / Society of Magnetic Resonance in Medicine* 63 (4) (April): 1050–8. doi:10.1002/mrm.22299.

Clement, G T, and K Hynynen. 2002. “A Non-invasive Method for Focusing Ultrasound Through the Human Skull.” *Physics in Medicine and Biology* 47 (8) (April 21): 1219–36.

Connolly, JD, MA Goodale, RS Menon, and DP Munoz. 2002. “Human fMRI Evidence for the Neural Correlates of Preparatory Set.” *Nature Neuroscience* 5 (12) (December): 1345–52. doi:10.1038/nn969.

Culjat, MO, D Goldenberg, P Tewari, and RS Singh. 2010. “A Review of Tissue Substitutes for Ultrasound Imaging.” *Ultrasound in Medicine & Biology* 36 (6) (June): 861–73. doi:10.1016/j.ultrasmedbio.2010.02.012.

Currie, D J. 1991. “Energy and Large-scale Patterns of Animal-and Plant-species Richness.” *The American Naturalist* 137 (1): 27–49.

Davies, II, and LR Gavrilov. 1996. "Application of Focused Ultrasound for Research on Pain." *Pain* 67 (1): 17–27.

Deffieux, T, and EE Konofagou. 2010. "Numerical Study of a Simple Transcranial Focused Ultrasound System Applied to Blood-brain Barrier Opening." *IEEE Transactions on Ultrasonics, Ferroelectrics and Frequency Control* 57 (12): 2637–53.

Deng, C X, F Sieling, H Pan, and J Cui. 2004. "Ultrasound-induced Cell Membrane Porosity." *Ultrasound in Medicine & Biology* 30 (4) (April): 519–26. doi:10.1016/j.ultrasmedbio.2004.01.005.

DeSouza, JF X, RS Menon, and S Everling. 2003. "Preparatory Set Associated with Pro-saccades and Anti-saccades in Humans Investigated with Event-related FMRI." *Journal of Neurophysiology* 89 (2) (February): 1016–23. doi:10.1152/jn.00562.2002.

Doyle, M, E G Walsh, G G Blackwell, and G M Pohost. 1995. "Block Regional Interpolation Scheme for K-space (BRISK): a Rapid Cardiac Imaging Technique." *Magnetic Resonance in Medicine : Official Journal of the Society of Magnetic Resonance in Medicine / Society of Magnetic Resonance in Medicine* 33 (2) (February): 163–70.

Duerk, J L, J S Lewin, and D H Wu. "Application of Keyhole Imaging to Interventional MRI: a Simulation Study to Predict Sequence Requirements." *Journal of Magnetic Resonance Imaging : JMRI* 6 (6): 918–24.

Duffner, P K, M E Horowitz, J P Krischer, H S Friedman, P C Burger, M E Cohen, R A Sanford, R K Mulhern, H E James, and C R Freeman. 1993. "Postoperative Chemotherapy and Delayed Radiation in Children Less Than Three Years of Age with Malignant Brain Tumors." *The New England Journal of Medicine* 328 (24) (June 17): 1725–31. doi:10.1056/NEJM199306173282401.

Ekstrom, LB, PR Roelfsema, JT Arsenault, G Bonmassar, and W Vanduffel. 2008. "Bottom-up Dependent Gating of Frontal Signals in Early Visual Cortex." *Science (New York, N.Y.)* 321 (5887) (July 18): 414–7. doi:10.1126/science.1153276.

Elias, WJ, D Huss, T Voss, J Loomba, M Khaled, E Zadicario, RC Frysinger, et al. 2013. "A Pilot Study of Focused Ultrasound Thalamotomy for Essential Tremor." *The New England Journal of Medicine* 369 (7) (August 15): 640–8. doi:10.1056/NEJMoa1300962.

Fischer, B, and H Weber. 1998. "Effects of Pre-cues on Voluntary and Reflexive Saccade Generation." *Experimental Brain Research* 120 (4) (May 25): 403–416. doi:10.1007/s002210050414.

Fry, FJ, H W Ades, and W J Fry. 1958. "Production of Reversible Changes in the Central Nervous System by Ultrasound." *Science (New York, N.Y.)* 127 (3289) (January 10): 83–4.

Fry, WJ, R Meyers, FJ Fry, DF Schultz, LL Dreyer, and RF Noyes. 1958. "Topical Differentia of Pathogenetic Mechanisms Underlying Parkinsonian Tremor and Rigidity as Indicated by Ultrasonic Irradiation of the Human Brain." *Transactions of the American Neurological Association*: 16.

Gao, J H, J Xiong, S Lai, E M Haacke, M G Woldorff, J Li, and P T Fox. 1996. “Improving the Temporal Resolution of Functional MR Imaging Using Keyhole Techniques.” *Magnetic Resonance in Medicine : Official Journal of the Society of Magnetic Resonance in Medicine / Society of Magnetic Resonance in Medicine* 35 (6) (June): 854–60.

Gavrilov LR, Gersuni GV, Ilyinsky OB, Sirotyuk MG, Tsirulnikov EM, Shchekanov EE. 1976. “The Effect of Focused Ultrasound on the Skin and Deep Nerve Structures of Man and Animal.” *Prog Brain Res* 43: 279–92.

Gaymard, B, J Lynch, C J Ploner, C Condy, and S Rivaud-Péchoux. 2003. “The Parieto-collicular Pathway: Anatomical Location and Contribution to Saccade Generation.” *The European Journal of Neuroscience* 17 (7) (April): 1518–26.

Gerits, A, R Farivar, BR Rosen, LL Wald, ES Boyden, and W Vanduffel. 2012. “Optogenetically Induced Behavioral and Functional Network Changes in Primates.” *Current Biology : CB* 22 (18) (September 25): 1722–6. doi:10.1016/j.cub.2012.07.023.

Goske, MJ, KE Applegate, J Boylan, PF Butler, MJ Callahan, BD Coley, S Farley, et al. 2008. “The ‘Image Gently’ Campaign: Increasing CT Radiation Dose Awareness Through a National Education and Awareness Program.” *Pediatric Radiology* 38 (3) (March): 265–9. doi:10.1007/s00247-007-0743-3.

Hallett, M. 2000. “Transcranial Magnetic Stimulation and the Human Brain.” *Nature* 406 (6792) (July 13): 147–50. doi:10.1038/35018000.

Han, YH, and CW Mun. 2011. “Evaluation of the Keyhole Technique Applied to the Proton Resonance Frequency Method for Magnetic Resonance Temperature Imaging.” *Journal of Magnetic Resonance Imaging : JMRI* 34 (5) (November): 1231–9. doi:10.1002/jmri.22708.

Harvey, E N. 1930. “The Effect of High Frequency Sound Waves on Heart Muscle and Other Irritable Tissues.” *American Heart Journal* 5 (3) (February): 388. doi:10.1016/S0002-8703(30)90343-2.

Hertzberg, Y., A. Volovick, Y. Zur, Y. Medan, S. Vitek, and G. Navon. 2010. “Ultrasound Focusing Using Magnetic Resonance Acoustic Radiation Force Imaging: Application to Ultrasound Transcranial Therapy.” *Medical Physics* 37 (6) (May 26): 2934. doi:10.1118/1.3395553.

Hu, X. 1994. “On the ‘Keyhole’ Technique.” *Journal of Magnetic Resonance Imaging : JMRI* 4 (2): 231.

Huang, Y, L Curiel, A Kukic, DB Plewes, R Chopra, and K Hynynen. 2009. “MR Acoustic Radiation Force Imaging: In Vivo Comparison to Ultrasound Motion Tracking.” *Medical Physics* 36 (6) (June): 2016–20.

Huerta, M F, L A Krubitzer, and J H Kaas. 1987. “Frontal Eye Field as Defined by Intracortical Microstimulation in Squirrel Monkeys, Owl Monkeys, and Macaque Monkeys. II. Cortical Connections.” *The Journal of Comparative Neurology* 265 (3) (November 15): 332–61. doi:10.1002/cne.902650304.

Hynynen, K, and J Sun. 1999. “Trans-skull Ultrasound Therapy: The Feasibility of Using Image-derived Skull Thickness Information to Correct the Phase Distortion.” *IEEE Transactions on Ultrasonics, Ferroelectrics, and Frequency Control* 46 (3) (January): 752–5. doi:10.1109/58.764862.

International Commission on Radiation Units and Measurements. 1998. *ICRU Report 61: Tissue Substitutes, Phantoms and Computational Modelling in Medical Ultrasound*. *… on Radiation Units and Measurements, ICRU Report*. Bethesda, MarylandICRU Publications.

Jeanmonod, D, B Werner, A Morel, L Michels, E Zadicario, G Schiff, and E Martin. 2012. “Transcranial Magnetic Resonance Imaging-guided Focused Ultrasound: Noninvasive Central Lateral Thalamotomy for Chronic Neuropathic Pain.” *Neurosurgical Focus* 32 (1) (January): E1. doi:10.3171/2011.10.FOCUS11248.

Jones, R A, O Haraldseth, T B Müller, P A Rinck, and A N Oksendal. 1993. “K-space Substitution: a Novel Dynamic Imaging Technique.” *Magnetic Resonance in Medicine : Official Journal of the Society of Magnetic Resonance in Medicine / Society of Magnetic Resonance in Medicine* 29 (6) (June): 830–4.

Kanai, R, N Muggleton, and V Walsh. 2012. “Transcranial Direct Current Stimulation of the Frontal Eye Fields During Pro- and Antisaccade Tasks.” *Frontiers in Psychiatry / Frontiers Research Foundation* 3 (January): 45. doi:10.3389/fpsyt.2012.00045.

Kaye, EA, J Chen, and KB Pauly. 2011. “Rapid MR-ARFI Method for Focal Spot Localization During Focused Ultrasound Therapy.” *Magnetic Resonance in Medicine : Official Journal of the Society of Magnetic Resonance in Medicine / Society of Magnetic Resonance in Medicine* 65 (3) (March): 738–43. doi:10.1002/mrm.22662.

King, RL, JR Brown, WT Newsome, and KB Pauly. 2013. “Effective Parameters for Ultrasound-induced in Vivo Neurostimulation.” *Ultrasound in Medicine & Biology* 39 (2) (February): 312–31. doi:10.1016/j.ultrasmedbio.2012.09.009.

Kirchner, H, EJ Barbeau, SJ Thorpe, J Régis, and C Liégeois-Chauvel. 2009. “Ultra-rapid Sensory Responses in the Human Frontal Eye Field Region.” *The Journal of Neuroscience : the Official Journal of the Society for Neuroscience* 29 (23) (June 10): 7599–606. doi:10.1523/JNEUROSCI.1233-09.2009.

Krasovitski, B, V Frenkel, S Shoham, and E Kimmel. 2011. “Intramembrane Cavitation as a Unifying Mechanism for Ultrasound-induced Bioeffects.” *Proceedings of the National Academy of Sciences of the United States of America* 108 (8) (February 22): 3258–63. doi:10.1073/pnas.1015771108.

Larrat, B, M Pernot, J-F Aubry, E Dervishi, R Sinkus, D Seilhean, Y Marie, A-L Boch, M Fink, and M Tanter. 2010. “MR-guided Transcranial Brain HIFU in Small Animal Models.” *Physics in Medicine and Biology* 55 (2) (January 21): 365–88. doi:10.1088/0031-9155/55/2/003.

Larrat, B, M Pernot, G Montaldo, M Fink, and M Tanter. 2010. “MR-guided Adaptive Focusing of Ultrasound.” *IEEE Transactions on Ultrasonics, Ferroelectrics and Frequency Control* 57 (8) (August 1): 1734–1747. doi:10.1109/TUFFC.2010.1612.

Lele, P P. 1962. “A Simple Method for Production of Trackless Focal Lesions with Focused Ultrasound: Physical Factors.” *The Journal of Physiology* 160 (3): 494.

Lipsman, N, ML Schwartz, Y Huang, L Lee, T Sankar, M Chapman, K Hynynen, and AM Lozano. 2013. “MR-guided Focused Ultrasound Thalamotomy for Essential Tremor: a Proof-of-concept Study.” *Lancet Neurology* 12 (5) (May): 462–8. doi:10.1016/S1474-4422(13)70048-6.

Magee, T R, and A H Davies. 1993. “Auditory Phenomena During Transcranial Doppler Insonation of the Basilar Artery.” *Journal of Ultrasound in Medicine : Official Journal of the American Institute of Ultrasound in Medicine* 12 (12) (December): 747–50.

Marquet, F, M Pernot, J-F Aubry, G Montaldo, L Marsac, M Tanter, and M Fink. 2009. “Non-invasive Transcranial Ultrasound Therapy Based on a 3D CT Scan: Protocol Validation and in Vitro Results.” *Physics in Medicine and Biology* 54 (9) (May 7): 2597–613. doi:10.1088/0031-9155/54/9/001.

Marrocco, R T. 1978. “Saccades Induced by Stimulation of the Frontal Eye Fields: Interaction with Voluntary and Reflexive Eye Movements.” *Brain Research* 146 (1) (May 5): 23–34.

Marsac, L, D Chauvet, B Larrat, M Pernot, B Robert, M Fink, A L Boch, J F Aubry, and M Tanter. 2012. “MR-guided Adaptive Focusing of Therapeutic Ultrasound Beams in the Human Head.” *Medical Physics* 39 (2) (February): 1141–9. doi:10.1118/1.3678988.

Martin, E, D Jeanmonod, A Morel, E Zadicario, and B Werner. 2009. “High-intensity Focused Ultrasound for Noninvasive Functional Neurosurgery.” *Annals of Neurology* 66 (6) (December): 858–61. doi:10.1002/ana.21801.

McDannold, N, GT Clement, P Black, F Jolesz, and K Hynynen. 2010. “Transcranial Magnetic Resonance Imaging- Guided Focused Ultrasound Surgery of Brain Tumors: Initial Findings in 3 Patients.” *Neurosurgery* 66 (2) (February): 323–32; discussion 332. doi:10.1227/01.NEU.0000360379.95800.2F.

McDannold, N, and SE Maier. 2008. “Magnetic Resonance Acoustic Radiation Force Imaging.” *Medical Physics* 35 (8) (August 23): 3748–58. doi:10.1118/1.2956712.

McDannold, N, N Vykhodtseva, and K Hynynen. 2008. “Blood-brain Barrier Disruption Induced by Focused Ultrasound and Circulating Preformed Microbubbles Appears to Be Characterized by the Mechanical Index.” *Ultrasound in Medicine & Biology* 34 (5) (May): 834–40. doi:10.1016/j.ultrasmedbio.2007.10.016.

Mihran, RT, FS Barnes, and H Wachtel. 1990. “Temporally Specific Modification of Myelinated Axon Excitability in Vitro Following a Single Ultrasound Pulse.” *Ultrasound in Medicine and Biology* 16 (3): 297–309.

Moore, T, and KM Armstrong. 2003. “Selective Gating of Visual Signals by Microstimulation of Frontal Cortex.” *Nature* 421 (6921) (January 23): 370–3. doi:10.1038/nature01341.

Moore, T, and M Fallah. 2001. "Control of Eye Movements and Spatial Attention." *Proceedings of the National Academy of Sciences of the United States of America* 98 (3) (January 30): 1273–6. doi:10.1073/pnas.021549498.

Murphy, MC, KJ Glaser, A Manduca, JP Felmlee, J Huston, and RL Ehman. 2010. "Analysis of Time Reduction Methods for Magnetic Resonance Elastography of the Brain." *Magnetic Resonance Imaging* 28 (10) (December): 1514–24. doi:10.1016/j.mri.2010.06.016.

Nitsche, MA, LG Cohen, EM Wassermann, A Priori, N Lang, A Antal, W Paulus, et al. 2008. "Transcranial Direct Current Stimulation: State of the Art 2008." *Brain Stimulation* 1 (3) (July): 206–23. doi:10.1016/j.brs.2008.06.004.

Olk, B, E Chang, A Kingstone, and T Ro. 2006. "Modulation of Antisaccades by Transcranial Magnetic Stimulation of the Human Frontal Eye Field." *Cerebral Cortex (New York, N.Y. : 1991)* 16 (1) (January 1): 76–82. doi:10.1093/cercor/bhi085.

O'Reilly, MA, Y Huang, and K Hynynen. 2010. "The Impact of Standing Wave Effects on Transcranial Focused Ultrasound Disruption of the Blood-brain Barrier in a Rat Model." *Physics in Medicine and Biology* 55 (18) (September): 5251–67. doi:10.1088/0031-9155/55/18/001.

Pernot, M, J-F Aubry, M Tanter, A-L Boch, F Marquet, M Kujas, D Seilhean, and M Fink. 2007. "In Vivo Transcranial Brain Surgery with an Ultrasonic Time Reversal Mirror." *Journal of Neurosurgery* 106 (6) (June): 1061–6. doi:10.3171/jns.2007.106.6.1061.

Pierrot-Deseilligny C, Müri, R M. Ploner, C J. Gaymard, B. Demeret, S. Rivaud-Pechoux, S. 2003. "Decisional Role of the Dorsolateral Prefrontal Cortex in Ocular Motor Behaviour." *Brain : a Journal of Neurology* 126 (Pt 6) (June): 1460–73.

Pouget, P, N Wattiez, S Rivaud-Péchoux, and Be Gaymard. 2010. "Rapid Development of Tolerance to Sub-anaesthetic Dose of Ketamine: An Oculomotor Study in Macaque Monkeys." *Psychopharmacology* 209 (4) (May): 313–8. doi:10.1007/s00213-010-1797-8.

Ressler, KJ, and HS Mayberg. 2007. "Targeting Abnormal Neural Circuits in Mood and Anxiety Disorders: From the Laboratory to the Clinic." *Nature Neuroscience* 10 (9) (September): 1116–24. doi:10.1038/nn1944.

Rinaldi, PC C, JP P Jones, F Reines, and L R Price. 1991. "Modification by Focused Ultrasound Pulses of Electrically Evoked Responses from an in Vitro Hippocampal Preparation." *Brain Research* 558 (1) (August 30): 36–42.

Rivaud, S., R.M. Müri, B. Gaymard, A.I. Vermersch, and C. Pierrot-Deseilligny. 1994. "Eye Movement Disorders After Frontal Eye Field Lesions in Humans." *Experimental Brain Research* 102 (1) (January): 110–20. doi:10.1007/BF00232443.

Royer, D., N. Dubois, and M. Fink. 1992. "Optical Probing of Pulsed, Focused Ultrasonic Fields Using a Heterodyne Interferometer." *Applied Physics Letters* 61 (2): 153. doi:10.1063/1.108202.

Sarvazyan, A P, O V Rudenko, S D Swanson, J B Fowlkes, and S Y Emelianov. 1998. "Shear Wave Elasticity Imaging: a New Ultrasonic Technology of Medical Diagnostics." *Ultrasound in Medicine & Biology* 24 (9) (November): 1419–35.

Shealy, CN, and E HENNEMAN. 1962. "Reversible Effects of Ultrasound on Spinal Reflexes." *Archives of Neurology* 6 (5) (May 1): 374–386. doi:10.1001/archneur.1962.00450230036005.

Spraggins, T A. 1994. "Simulation of Spatial and Contrast Distortions in Keyhole Imaging." *Magnetic Resonance in Medicine : Official Journal of the Society of Magnetic Resonance in Medicine / Society of Magnetic Resonance in Medicine* 31 (3) (March): 320–2.

Suga, M, T Matsuda, M Komori, K Minato, and T Takahashi. 1999. "Keyhole Method for High-speed Human Cardiac Cine MR Imaging." *Journal of Magnetic Resonance Imaging : JMRI* 10 (5) (November): 778–83.

Sun, S-W, Y-J Chen, K-H Chou, and W-C Chu. 2010. "Keyhole and Zero-padding Approaches for Reduced-encoding Diffusion Tensor Imaging of the Mouse Brains." *Magnetic Resonance Imaging* 28 (10) (December): 1413–9. doi:10.1016/j.mri.2010.07.016.

Szobota, S, P Gorostiza, F Del Bene, C Wyart, DL Fortin, KD Kolstad, O Tulyathan, et al. 2007. "Remote Control of Neuronal Activity with a Light-gated Glutamate Receptor." *Neuron* 54 (4) (May 24): 535–45. doi:10.1016/j.neuron.2007.05.010.

Tang, SC, and GT Clement. 2010. "Standing-wave Suppression for Transcranial Ultrasound by Random Modulation." *IEEE Transactions on Bio-medical Engineering* 57 (1) (January): 203–5. doi:10.1109/TBME.2009.2028653.

Tanter, M, M Pernot, J F Aubry, G Montaldo, F Marquet, and M Fink. 2007. "Compensating for Bone Interfaces and Respiratory Motion in High-intensity Focused Ultrasound." *International Journal of Hyperthermia* 23 (2) (March): 141–51.

Tanter, M, JL Thomas, and M Fink. 1998. "Focusing and Steering Through Absorbing and Aberrating Layers: Application to Ultrasonic Propagation Through the Skull." *The Journal of the Acoustical Society of America* 103 (5) (May 1): 2403. doi:10.1121/1.422759.

Thomas, J-L, and M Fink. 1996. "Ultrasonic Beam Focusing Through Tissue Inhomogeneities with a Time Reversal Mirror: Application to Transskull Therapy." *IEEE Transactions on Ultrasonics, Ferroelectrics and Frequency Control* 43 (6) (November 1): 1122–1129. doi:10.1109/58.542055.

Tsui, P-H, S-H Wang, and C-C Huang. 2005. "In Vitro Effects of Ultrasound with Different Energies on the Conduction Properties of Neural Tissue." *Ultrasonics* 43 (7): 560–565.

Tufail, T, A Matyushov, N Baldwin, ML Tauchmann, J Georges, A Yoshihiro, SIH Tillery, and WJ Tyler. 2010. "Transcranial Pulsed Ultrasound Stimulates Intact Brain Circuits." *Neuron* 66 (5) (June 10): 681–94. doi:10.1016/j.neuron.2010.05.008.

Tufail, Y, A Yoshihiro, S Pati, MM Li, and WJ Tyler. 2011. "Ultrasonic Neuromodulation by Brain Stimulation with Transcranial Ultrasound." *Nature Protocols* 6 (9) (September 1): 1453–70. doi:10.1038/nprot.2011.371.

Tung, Y-S, F Vlachos, JJ Choi, T Deffieux, K Selert, and EE Konofagou. 2010. "In Vivo Transcranial Cavitation Threshold Detection During Ultrasound-induced Blood-brain Barrier Opening in Mice." *Physics in Medicine and Biology* 55 (20) (October 21): 6141–55. doi:10.1088/0031-9155/55/20/007.

Tung, Y-S, F Vlachos, JA Feshitan, MA Borden, and EE Konofagou. 2011. "The Mechanism of Interaction Between Focused Ultrasound and Microbubbles in Blood-brain Barrier Opening in Mice." *The Journal of the Acoustical Society of America* 130 (5) (November): 3059–67. doi:10.1121/1.3646905.

Tyler, WJ, Y Tufail, M Finsterwald, ML Tauchmann, EJ Olson, and C Majestic. 2008. "Remote Excitation of Neuronal Circuits Using Low-intensity, Low-frequency Ultrasound." *PloS One* 3 (10) (January): e3511. doi:10.1371/journal.pone.0003511.

Van Vaals, J J, M E Brummer, W T Dixon, H H Tuithof, H Engels, R C Nelson, B M Gerety, J L Chezmar, and J A den Boer. 1993. "'Keyhole' Method for Accelerating Imaging of Contrast Agent Uptake." *Journal of Magnetic Resonance Imaging : JMRI* 3 (4): 671–5.

Valero-Cabre, A, N Wattiez, M Monfort, C François, S Rivaud-Péchoux, B Gaymard, and P Pouget. 2012. "Frontal Non-invasive Neurostimulation Modulates Antisaccade Preparation in Non-human Primates." Ed. Suliann Ben Hamed. *PloS One* 7 (6) (January): e38674. doi:10.1371/journal.pone.0038674.

Varma, G, R E Lenkinski, and E Vinogradov. 2012. "Keyhole Chemical Exchange Saturation Transfer." *Magnetic Resonance in Medicine : Official Journal of the Society of Magnetic Resonance in Medicine / Society of Magnetic Resonance in Medicine* 68 (4) (October): 1228–33. doi:10.1002/mrm.23310.

Xiong, J, PT Fox, and J-H Gao. 1999. "The Effects of K-space Data Undersampling and Discontinuities in Keyhole Functional MRI." *Magnetic Resonance Imaging* 17 (1): 109–119.

Yang, PS, H Kim, W Lee, M Bohlke, S Park, TJ Maher, and S-S Yoo. 2012. "Transcranial Focused Ultrasound to the Thalamus Is Associated with Reduced Extracellular GABA Levels in Rats." *Neuropsychobiology* 65 (3) (January): 153–60. doi:10.1159/000336001.

Yoo, S-S, A Bystritsky, J-H Lee, Y Zhang, K Fischer, B-K Min, NJ McDannold, A Pascual-Leone, and FA Jolesz. 2011. "Focused Ultrasound Modulates Region-specific Brain Activity." *NeuroImage* 56 (3) (June 1): 1267–75. doi:10.1016/j.neuroimage.2011.02.058.

Younan, Y, T Deffieux, B Larrat, M Fink, M Tanter, and J-F Aubry. 2013. "Influence of the Pressure Field Distribution in Transcranial Ultrasonic Neurostimulation." *Medical Physics* 40 (8) (August): 082902. doi:10.1118/1.4812423.

Young, R R, and E Henneman. 1961. "Functional Effects of Focused Ultrasound on Mammalian Nerves." *Science (New York, N.Y.)* 134 (3489) (November 10): 1521–2.

Zhang, F, AM Aravanis, A Adamantidis, L de Lecea, and K Deisseroth. 2007. “Circuit-breakers: Optical Technologies for Probing Neural Signals and Systems.” *Nature Reviews. Neuroscience* 8 (8) (August): 577–81. doi:10.1038/nrn2192.

Communications scientifiques

Articles publiés dans des revues à comité de lecture

R Paquin, A Vignaud, L Marsac, Y Younan, S Lehéricy, M Tanter and J-F Aubry, **Keyhole** Acceleration for Magnetic Resonance Acoustic Radiation Force Imaging (MR ARFI) *Magn Reson Imaging. 2013 Dec;31(10):1695-703. doi: 10.1016/j.mri.2013.07.011.*

Y Younan, T Deffieux, B Larrat, M Fink, M Tanter, and J-F Aubry (2013). **Influence of the pressure field distribution in Transcranial ultrasonic neuromodulation.** *Medical physics, 40(8), 082902. doi:10.1118/1.4812423*

T Deffieux and Y Younan, N Wattiez, M Tanter, P Pouget and J-F Aubry, **Low intensity focused ultrasound modulates monkey visuomotor behavior.** *Current Biology*, *Volume 23, Issue 23*, *2 December 2013*, *Pages 2430-2433*

Conférences avec participation

- **Ultrasonic neuromodulation in a rat model: in vivo determination of the acoustic pressure threshold and spatial distribution in the brain**, Y. Younan, T. Deffieux, B. Larrat, M. Fink, J-F. Aubry and M. Tanter, Acoustics conference, Nantes (France) 23 April 2012.

- **Ultrasonic Neuromodulation in a rat model: in vivo investigation of an acoustic threshold for motor response** Y. Younan, T. Deffieux, B. Larrat, A. Souilah, M. Fink, J-F. Aubry, M. Tanter, 12th International Symposium on Therapeutic Ultrasound conference, Heidelberg (Germany) 10 June 2012.

- **Ultrasonic Neuromodulation in a rat model: investigation of the in situ threshold for motor response** T Deffieux, Y Younan, B Larrat, A Souilah, M Fink, J-F Aubry, M

Tanter, 2012 IEEE International Ultrasonics Symposium, Dresden (Germany) 7 October 2012

- **Ultrasonic neuromodulation in awake monkey: modulation of saccade control** Y. Younan, T. Deffieux, M. Tanter, J. Aubry, N. Wattiez, P. Pouget.

13th International Symposium on Therapeutic Ultrasound conference, Shanghai (China) 12 May 2013.

- **Transcranial ultrasound neuromodulation of the contralateral visual field in awake monkey** Y Younan, T Deffieux, N Wattiez, M Tanter, P Pouget, J-F Aubry

2013 IEEE International Ultrasonics Symposium, Prague (Czech Republic) 22 Jul 2013